

An observational perspective of convective momentum transport

Koning, A.M.

DOI

[10.4233/uuid:f881c04f-e8d1-4d54-86d6-99c173b650ec](https://doi.org/10.4233/uuid:f881c04f-e8d1-4d54-86d6-99c173b650ec)

Publication date

2023

Document Version

Final published version

Citation (APA)

Koning, A. M. (2023). *An observational perspective of convective momentum transport*. [Dissertation (TU Delft), Delft University of Technology]. <https://doi.org/10.4233/uuid:f881c04f-e8d1-4d54-86d6-99c173b650ec>

Important note

To cite this publication, please use the final published version (if applicable). Please check the document version above.

Copyright

Other than for strictly personal use, it is not permitted to download, forward or distribute the text or part of it, without the consent of the author(s) and/or copyright holder(s), unless the work is under an open content license such as Creative Commons.

Takedown policy

Please contact us and provide details if you believe this document breaches copyrights. We will remove access to the work immediately and investigate your claim.

An observational perspective of convective momentum transport

Ada Mariska Koning

An observational perspective of convective momentum transport

PROEFSCHRIFT

ter verkrijging van de graad van doctor
aan de Technische Universiteit Delft,
op gezag van de Rector Magnificus
prof. dr. ir. T.H.J.J. van der Hagen
voorzitter van het College voor Promoties,
in het openbaar te verdedigen op
maandag, 18 september 2023 om 10:00 uur

door

Ada Mariska KONING

Master of Applied Earth Sciences,
Technische Universiteit Delft, Nederland
geboren te Capelle aan den IJssel, Nederland

Dit proefschrift is goedgekeurd door de promotoren.

Samenstelling promotiecommissie:

Rector Magnificus	voorzitter
prof. dr. A. P. Siebesma	Technische Universiteit Delft, promotor
dr. A. A. Nuijens	Technische Universiteit Delft, copromotor

onafhankelijke leden:

prof. dr. ir. B. J. H. van de Wiel	Technische Universiteit Delft
prof. dr. ir. H. W. J. Russchenberg	Technische Universiteit Delft
prof. dr. J. Mann	Danish Technical University
dr. A. P. Lock	Met Office
dr. F. Couvreur	Météo-France

Dit onderzoek is financieel mogelijk gemaakt door de *European Research Council* (ERC) onder het *European Union's Horizon 2020* programma voor onderzoek en innovatie (*Starting grant agreement*, nummer 714918).

Trefwoorden / *keywords*: shallow convection, cumulus, wind mixing, convective momentum transport, Cabauw, EUREC4A, observations, large eddy simulation

Gedrukt door / *Printed by*: Gildeprint

Omslag: bewerking van een foto van Anneke Janissen

ISBN 978-94-6384-478-9

Dit werk is auteursrechtelijk beschermd / © 2023 A. Mariska Koning

Alle rechten voorbehouden / *All rights reserved*.

Typeset by the author with the \LaTeX Documentation System.

Een elektronische versie van dit proefschrift is beschikbaar via /

An electronic version of this dissertation is available at:

<https://repository.tudelft.nl>

Contents

Summary	v
Samenvatting	ix
1 Introduction	1
1.1 The interaction between shallow cumulus, convection, and wind	2
1.1.1 Convective momentum transport	4
1.1.2 Insights from large eddy simulations	9
1.1.3 Observational approaches	10
1.2 Research goals	12
1.3 Outline	12
2 Surface-layer wind shear and momentum transport from clear-sky to cloudy weather regimes over land	15
2.1 Introduction	15
2.2 Data	18
2.2.1 Cabauw (Ruisdael) observational data	18
2.2.2 Large Eddy Simulations	19
2.3 Cloud regime classification	20
2.3.1 Validating the LES against observations	23
2.4 Climatology of cloud regimes	24
2.5 Wind gradients in the surface layer	27
2.5.1 Non-dimensional wind gradients following Monin-Obukhov Similarity Theory	29
2.5.2 Wind and momentum flux profiles	33
2.6 Conclusion & discussion	35
3 Momentum fluxes from airborne wind measurements in three cumulus cases over land	39
3.1 Introduction	39
3.2 Flight measurements and data processing	41
3.2.1 Flight strategy and measurements	41
3.2.2 Updraft detection algorithm	47
3.3 Flight conditions: wind and thermodynamic profiles	48
3.4 Momentum flux profiles	52

3.4.1	Sub-cloud and cloud layer profiles	52
3.4.2	Scale contributions to flux	55
3.4.3	Conclusions	57
4	The wind structure below marine trade-wind cumulus	61
4.1	Introduction	61
4.2	Data description	64
4.2.1	Long-range wind lidar	64
4.2.2	Doppler cloud radar	66
4.3	Data Processing	66
4.3.1	Cloud entity selection	66
4.4	Results	68
4.5	Summary and outlook	74
5	Conclusions and perspectives	77
5.1	Observations and pseudo-observations	78
5.2	Observation-based insights into (C)MT	80
5.3	Recommendations	83
	Bibliography	85
	Acknowledgements	95
	Curriculum Vitae	97
	List of Publications	99

Summary

Shallow cumulus clouds interact with their environment and redistribute heat, moisture, and momentum (wind speed and direction) in the atmosphere. The same convective plume that forms the cloud is for a large extent responsible for this transport. Modeling the effect of shallow cumulus clouds is challenging because these clouds are smaller than can be directly simulated by models. Weather and climate models therefore rely on empirical functions to represent the effect of sub-grid processes such as the turbulent and convective transport. The transport of moisture and heat through cumulus convection has received a lot of attention from the atmospheric science community. Momentum transport has been studied far less, even though a few studies indicate that momentum transport may have a large influence on local weather as well as the large-scale circulation.

One reason that momentum transport by shallow cumulus convection has received less attention stems from a lack of simultaneous measurements of clouds and wind. This thesis analyses the relationship between cumulus clouds, wind, and momentum transport using three sets of observational data, two of which were collected during this research. The data helps us understand:

1. Differences in the wind field and profiles of wind and momentum flux in regimes of cumulus clouds, clear skies, and non-convective cloudiness conditions.
2. The different length scales that contribute to the momentum transport.

These findings are put in light of existing theories that are at the basis of current parametrizations, for example the mass flux and eddy diffusivity theory.

The first data set consists of 10 years of observations and pseudo-observations from large eddy simulations over Cabauw, The Netherlands. We categorised each day as either a clear-sky day, cumulus day (subdivided into two groups of different cloud cover), or as a day with non-convective clouds (stratus, for instance). On average, clear sky and cumulus days showed a similar development of the wind speed throughout the day. But on cumulus days, the near-surface wind speed increases more than on clear-sky days. Under cumulus conditions there is also less wind shear between 80 and 200 m of the atmosphere, which implies better vertical mixing of the wind in the upper surface layer.

To make a fairer comparison of the effect of cumulus on the wind, we must account for a few factors. First, we need to consider that the surface buoyancy flux, which drives turbulence and convection in the boundary layer, is typically stronger

on cumulus days than under clear sky days. Second, the different cloud regimes have different large-scale wind conditions. Under stronger wind, the surface layer wind shear is also larger. The Obukhov length is a measure that takes into account both the wind shear and the (driving force behind) convection. Comparing clear sky and cumulus days *at a similar Obukhov length*, we find that wind shear near the top of the surface layer is still smaller in cumulus conditions.

On cumulus days, there is also more surface friction than we would expect based on (Monin-Obukhov similarity) theory. Likely, this is related to the faster surface winds that are maintained under cumulus conditions. However, this may also suggest that momentum transport in the surface is not solely determined by local properties of the atmosphere – one of the assumptions in this theory. Apart from the small-scale turbulence, coherent convective structures that span the boundary layer may penetrate into the surface layer and impact its momentum transport.

The pseudo-observations in the form of large-eddy simulations (LES) reveal differences in wind and momentum flux profiles throughout the entire boundary layer. Above 200 m the wind shear is generally very small up to cloud base for all convective regimes. Aligned with the mean wind direction, the momentum fluxes from the pseudo-observations were analysed parallel to the mean wind direction (along wind) and perpendicular to the prevailing wind direction (crosswind) of the surface layer (at 65 m height). The fluxes have a similar shape among the four categories and on average act to reduce shear. The more cumulus cloud fraction near cloud base height, the larger the magnitude of the momentum flux remains at that height, maintaining up to 30% of the value at the surface. This seems also true for clouds on non-convective days, but the mechanisms causing the transport there may differ from the convective cloud regimes. Differences between the categories are more evident in the magnitude of the crosswind flux. Clear-sky days and cumulus days up to 30% cloud cover have significantly larger cross-wind momentum flux than cumulus days with more cloud cover (up to 70%) and days with non-convective cloudy conditions.

The second data set involved three measurement flights over agricultural areas in Germany in spring 2019. The first flight started out with clear skies and weak winds, where local shallow cumulus started forming over a hilly area, reaching a thickness of only 500 m. The second flight was characterized by a cold front passage, where stratocumulus was present next to cumulus. Cumulus clouds were about 1 km thick, and many other clouds were present at higher altitudes. The last flight targeted a large cumulus field having clouds with diverse tops, which were at most 800 m thick. During the flights, a down-looking wind lidar was deployed from an airplane cruising at 11 km altitude and a second aeroplane took high-frequency in-situ measurements (allowing to measure turbulence) at different heights along the same track. Despite the coarser footprint of the lidar, due to the faster aircraft and its viewing angle, it measured similar horizontal wind variance along the track as the in-situ measurements.

From the in-situ measurements we calculated the momentum transport and selected regions of upward moving air. The first day showed that compared to clear sky patches the momentum flux was more than twice as large below cumulus clouds.

The third flight enabled us to compare clouds of different thickness: one track encountered thicker clouds than a second track. Updrafts contributed one-third up to two-thirds to the momentum transport in thinner clouds, which is still much less than what they typically contribute to the buoyancy flux. The thicker clouds, typically having stronger updrafts, had much larger fluxes in the cloud layer and updrafts contributed more to the overall flux.

The in-situ measurements were filtered to assess the contributions of different scales to the momentum transport. For instance, scales smaller than 100 m represent smaller turbulent processes, whereas larger scales of turbulence, such as convection, act on scales of 100 m up to a few kilometers. On the track with thicker clouds, scales >1.4 km contributed more to the momentum flux, especially near cloud base. The sign of the flux carried on these scales of more organised coherent flows was found to be a so-called counter-gradient flux, which acts to enhance shear, rather than reducing shear, as in down-gradient transport which was typical for all flows with scales < 1.4 km. The contributions of different scales to the total momentum flux, where positive and negative fluxes can cancel out, highlights a challenge for parametrizing momentum transport.

The third data set was part of a larger field campaign, EUREC4A, which took place in the marine trade-wind region in early 2020. Using a cloud radar and wind lidar aboard the research vessel Meteor, the study visualized the effect that clouds have on the wind field around them. The anomalous wind by subtracting the mean wind during 10 minute window of each measurement, visualises the convective flows, while removing meso-scale and large-scale effects, including synoptic changes and the diurnal cycle. We selected 843 clouds from the data set and grouped them according to their thickness. Compared to the campaign average, wind speed was generally faster when there were clouds, in line with earlier studies that found that clouds are better correlated with faster wind.

A composite average of (anomalous) wind field showed that winds in the cloud are typically slower than their surroundings. This is a well-known property, where air with lower momentum (slower wind) is transported upward into the cloud by convection. This upward plume is visible in the clouds less than 1 km thick. Furthermore, signatures of stronger winds at the upwind side of the cloud were found, as predicted by sailing theory, as well as slower winds at the downwind side. For clouds between 500 - 1000 m thick, a clearer circulation is evident, with horizontal convergence in the main wind direction that extends throughout the sub-cloud layer, whereas sailing theory only depicts convergence close to the surface. For even deeper clouds, the winds and circulations become more complex, and indicate the presence of downward motion below clouds caused by precipitation, as well as the presence of other nearby convective plumes, as deeper clouds tend to be part of larger cloud structures composed of multiple individual plumes.

This thesis has shown that cumulus clouds leave a signature on the atmospheric flow in which they are embedded. Even though the momentum transport associated with cumulus clouds can often be understood in terms of common theories as mass flux and eddy diffusivity, the presence of counter-gradient momentum transport,

cross-wind circulations, and significant flux not accounted for by coherent updrafts, challenges these theories. The interaction between clouds and the atmospheric flow is mutual, dynamic, and remains a fascinating challenge.

Samenvatting

Ondiepe stapelwolken hebben een wisselwerking met hun omgeving. Ze zijn gekoppeld aan convectieve bewegingen die warmte, vocht en impuls (windsnelheid en richting) herverdelen in de atmosfeer. De convectieve pluimen waarop de wolk ontstaat, zijn grotendeels verantwoordelijk voor deze herverdeling. Het modelleren van het effect van ondiepe stapelwolken (cumulus) is een uitdaging, omdat de wolken kleiner zijn dan wat direct kan worden gesimuleerd door computermodellen. Grootschalige modellen, zoals weer- en klimaatmodellen zijn daarom afhankelijk van empirische functies die het effect sub-gridschaal processen meenemen, zoals het geval voor turbulent en convectief transport. Hoewel vocht- en warmtetransport veel aandacht van de onderzoeksgemeenschap hebben gekregen, is er naar convectief impulstransport nog niet veel onderzoek gedaan. Echter, een paar studies wijzen uit dat impulstransport een groot effect zou kunnen hebben op het lokale weer zowel lokaal als ook op de grootschalige circulatie en het klimaat.

Een van de redenen dat impulstransport door ondiepe cumulus niet veel is bestudeerd, komt doordat er weinig wind(profiel)metingen worden gedaan en nog minder tegelijkertijd met wolkenmetingen. In dit proefschrift worden drie datasets gebruikt, om de relatie tussen cumuluswolken, wind en momentumtransport te bestuderen. Twee daarvan zijn tijdens dit onderzoek tot stand gekomen. De data helpt ons te begrijpen

1. Hoe het windveld en de gemiddelde profielen van wind en impulstransport tussen wolkenloze dagen, dagen met cumulusbewolking en dagen met niet-convectieve bewolking verschillen;
2. Welke lengteschalen (het meest) bijdragen aan het totale impulstransport.

Onze bevindingen worden in het licht gezet van bestaande theorieën, zoals de massa flux en de flux-profiel relaties die vaak worden gebruikt als parameterisaties in weer- en klimaatmodellen.

De eerste dataset bestaat uit 10 jaar aan metingen en pseudo-metingen van simulaties (zogenoeten *Large-Eddy Simulations*, LES) van het weer op Cabauw. Elke dag werd gecategoriseerd naar zijn bewolking, waarin we een aantal gevallen hebben onderscheiden: wolkenloze dagen, dagen met stapelwolken (twee groepen met verschillende bedekkingsgraad), of dagen met niet-convectieve bewolking (denk bijvoorbeeld aan stratuswolken). Op een gemiddelde dag zonder bewolking of met stapelwolken verloopt de ontwikkeling van de wind doorgaans hetzelfde, hoewel de

windsnelheid nabij de grond op het midden van de dag over het algemeen sneller is op dagen met stapelwolken. Ook is er op die dagen tussen 80 en 200 m van de atmosfeer minder windschering, wat kan duiden op effectievere menging van wind in de oppervlaktelaag als convectieve bewolking aanwezig is.

Om een eerlijkere vergelijking te maken tussen dagen met en zonder (convectieve) bewolking, moeten we met twee factoren rekening houden. Ten eerste is convectie vaak sterker is op dagen met stapelwolken en verantwoordelijk voor zowel een betere menging in de atmosfeer als ook voor het ontstaan van de wolken. Minder windschering (betere menging) en snellere wind kunnen dus niet alleen aan de wolken worden gewijd. Ten tweede is er een verschil in windsterkte op de dagen waarop de verschillende soorten wolken voorkomen. Een sterkere wind is moeilijker te behouden nabij de oppervlakte, waardoor de windschering daar lokaal groter zal blijven. De Obukhovlengte is een maat die met zowel de windschering als de sterkte van (het aandrijven van) convectie rekening houdt. Ook wanneer we *bij dezelfde Obukhovlengte* de windschering tussen 80 - 200 m vergelijken, is de windschering op dagen met stapelwolken kleiner.

De schuifspanningssnelheid, een maat voor impulstransport aan het oppervlak, is op cumulusdagen groter dan men verwacht op basis van theorie (Monin-Obukhov gelijkvormigheid). De relatief snellere oppervlaktewind die aanwezig is op deze dagen, ligt daar waarschijnlijk ten grondslag aan. De bevinding suggereert dat convectie met een lengteschaal nabij de grenslaaghoogte zou kunnen binnendringen in de oppervlaktelaag waarmee het invloed heeft op het impulstransport aldaar. Dit is in tegenspraak met de gelijkvormigheidstheorie van Monin-Obukhov waarin wordt aangenomen dat alleen kleinschalige turbulente wervelingen het impulstransport bepalen.

Met behulp van LES (de pseudo-observaties) is ook de wind in de rest van de grenslaag onderzocht, waarmee we onder andere vonden dat de windschering tussen 200 m hoogte en de wolkenbasis zeer klein is voor alle convectieve dagen. De impulstransportprofielen in de richting van de wind zijn in elke wolken categorie grotendeels hetzelfde en reduceren de windschering. Dagen met meer of dikkere wolken hebben doorgaans een grotere impulsflux in de buurt van de wolkenbasis, die kan oplopen tot 30 % van de oppervlaktewaarde. Grotere verschillen tussen de categorieën uiten zich in de impulsflux loodrecht op de gemiddelde windrichting in de oppervlaktelaag (op 65 m hoogte). Wolkenloze dagen en dagen met stapelwolken met een bedekkingsgraad 5-30%, hebben een stuk meer impulstransport dan stapelwolkdagen met hoge bedekkingsgraad (30-70%) of bewolkte dagen zonder convectieve wolken.

De tweede dataset behelst data verkregen van drie meetvluchten over landelijk Duits gebied in het voorjaar van 2019. Op de eerste vluchtdag begon de dag zonder bewolking met zachte wind. Lokaal onstonden een aantal ondiepe cumuluswolkjes over de heuvels, die hooguit een dikte van 500 m haalden. De tweede vlucht vond plaats terwijl een koufront overtrok. Naast stapelwolken die een dikte bereikten van ongeveer 1 km, waren er ook stratocumuluswolken. Vele andersoortige bewolking was hoger op aanwezig. De derde vlucht vond plaats in een groot wolkenveld met

stapelwolken van verschillende grootte en dikte. De grootste waren ongeveer 800 m dik. Elke meetvlucht bleef één vliegtuig op 7.5 km hoogte en bracht met behulp van een Doppler wind lidar de wind profielen van onder het vliegtuig in kaart. Tegelijkertijd vloog een tweede kleiner vliegtuig over hetzelfde pad om op hoog-frequente turbulentie in-situ te kunnen meten. Hoewel de wind lidar een veel grotere voetafdruk heeft vanwege de hogere snelheid en de wijdere beelthoek van het instrument, kwam de windvariatie goed overeen met die van de in-situ metingen.

Met de hoog-frequente in-situ metingen zijn de impulstransporten worden en selecteerde we tijden met opwaardse luchtstromen. Daar waar ondiepe wolken ontstaan, is het impulstransport meer dan twee keer zo groot als in regio's zonder wolken. Ook konden we uit de derde vlucht de fluxen van dikkere wolken op een eerste traject vergelijken met die van minder dikke wolken op een ander traject. Convectieve bewegingen droegen een tot twee derde bij aan het impulstransport in dunnere wolken, veel minder dan de typische bijdrage aan warmtetransport. Dikkere wolken, die vaak ontstaan op sterkere convectie, gingen gepaard met een sterkere flux en de opwaardse luchtstromen droegen meer bij aan het impulstransport.

Door het filteren van de in-situ metingen kan inzicht worden verkregen in hoe verschillende schalen bijdragen aan het impulstransport. Bijvoorbeeld, zeer kleine schalen vertegenwoordigen kleinschalige turbulentie, terwijl grotere turbulente schalen, waar convectie bij hoort, van honderden meters tot enkele kilometers reiken. Op het traject met dikkere wolken (derde vlucht), droegen schalen van groter dan 1.4 km meer bij aan de impulsflux, vooral nabij wolkenbasis. De flux zorgde daar voor een toename in de windschering, hoewel de flux normaalgesproken voor minder windschering zorgt. Verschillende schalen kunnen een verschillend effect op impuls hebben, verschillende schalen kunnen zelfs elkaars bijdrage tenniet doen, waardoor het een uitdaging is om momentum transport te parameteriseren.

De laatste dataset is een onderdeel van een grotere meetcampagne, EUREC4A, die begin 2020 plaatsvond op de oceaan in een typische passaatwindregio. De wolkenradar en windlidar aan boord van het onderzoeksschip de *Meteor*, gaven ons inzicht in het effect van wolken op het windveld. Door te kijken de afwijking van de wind ten opzichte van een lopend gemiddelde van 10 minuten, krijgen we inzicht in de invloed van convectieve luchtstromen op de wind, terwijl mesoscaal en grootschalige wind, zoals synoptische ontwikkelingen en veranderingen in de wind gerelateerd de dagelijkse gang, worden weggehaald. Elke individuele wolk is uit de data geselecteerd en ingedeeld in een groep op basis van wolkendikte. De gemiddelde windprofielen van de wolkengroepen laten zien dat de wind sneller is dan het gemiddelde van de hele campagne, wat overeenkomt met eerdere studies die een correlatie hebben gevonden tussen bedekkingsgraad en snellere wind.

In de wolken zelf is de wind vaak minder sterk dan in de omgeving. Dit wordt veroorzaakt door het transport van langzamere wind van nabij de grond richting de wolk door convectie: de opgaande pluim die onder wolken kan worden gezien. Bij de wolkenbasis is het (gemiddelde) verschil ongeveer 1 ms^{-1} tussen de windsnelheid in en rondom wolken van maximaal 500 m dik. Ook vinden we een sterkere wind stroomopwaards en een langzamere wind stroomafwaards, zoals voorspeld door zeil-

theorie. Bij wolken met een dikte tussen de 500 - 1000 m is een circulatie zichtbaar, waarbij er over de hele luchtlaag onder de wolk horizontale convergentie plaatsvindt in tegenstelling tot de zeiltheorie waarbij alleen aan het oppervlak horizontale convergentie wordt verwacht.

Dit proefschrift laat zien dat de stapelwolken een duidelijke signatuur achterlaten in de atmosferische stromingen (wind). Hoewel bekende theorieën zoals de massa flux en eddy diffusie de impulstransport redelijk kunnen voorspellen, zijn er situaties waar deze theorieën niet geschikt zijn. De interactie tussen cumulus wolken en de wind blijft dynamisch en fascinerend.

1

Introduction

"Look up, marvel at the ephemeral beauty, and live life with your head in the clouds"

Gavin Pretor-Pinney,
Manifesto of the Cloud Appreciation Society

Who frequently looks up to the clouds can get an idea of the weather's mood: the threatening skies when it is about to rain, changing cloud decks that announce fronts, or high curving cirrus clouds that indicate a change in wind directions aloft. To a careful observer, clouds can tell a lot about the (upcoming) weather.

In climate and weather prediction models, clouds do not always accurately depict the state of the atmosphere. Clouds often form in shapes and sizes that are much finer than models grids, and in coarse-grid models they must therefore be represented through empirical and imperfect formulations. Clouds are one of the main sources of uncertainties in weather and climate prediction. Especially shallow convective clouds over the ocean are a major cause of the spread in climate sensitivity predicted by climate models (Bony and Dufresne, 2005).

The World Climate Research Program's grand challenge on clouds, circulation, and climate sensitivity, was initiated to advance the understanding of the coupling of clouds to large-scale circulations, and the implications for climate change (Bony et al., 2017a). Shallow clouds may impact circulations in several ways. The one that received most attention is the radiative cooling associated with shallow clouds (e.g. Shukla and Sud, 1981; Soden and Held, 2006; Webb et al., 2006; Li et al., 2015; Voigt et al., 2021). Clouds also directly impact the (local and large-scale) flow through convective momentum transport (Zhang and Klein, 2013). The interaction between clouds and wind has not received much attention, and it is hardly addressed from an observational perspective. This thesis specifically explores the relationships between clouds and winds through convective momentum transport, using observations.

1.1 The interaction between shallow cumulus, convection, and wind

Cumulus clouds are tightly linked to convection: they form in coherent warm and moist rising air that are called thermals. Upon reaching the so-called lifting condensation level, the thermals are visualized through the condensation of water vapour into cloud droplets. The cloud thickness, which is often called "cloud depth" by meteorologists, is an indication of the strength of convection: stronger convection leads to deeper clouds. The various cumulus types distinguish themselves mostly through their depth (see Figure 1.1): panel (a) shows cumulus humilis, characterized by very small vertical development, and capped by a temperature inversion. It is often a forced cloud that is formed due to the inertia of the thermals feeding them from underneath. It does not reach the level of free convection and remains negatively buoyant. Panel (b) shows a field of cumulus mediocris that have moderate vertical development but do not precipitate. Mediocris often develop into congestus or cumulonimbus (thunderstorm cloud)). Cumulus mediocris is an active cloud. Active clouds feed back on the sub-cloud layer and thus their lifetime do not solely depend on the presence of the parent thermal. Panel (c) and (d) show a cumulus congestus cloud, which is also an active cloud. It is characterized by a large tower (c) or large cauliflower (d) appearance. The threatening tops of the cauliflower cumulus congestus (d) may indicate it will develop into a thunderstorm. A strict definition of shallow cumulus does not exist, but in this thesis all cumulus clouds with a cloud top below 3 km are considered shallow.

Panel (c) also shows a schematic of the cloud's underlying thermal circulation. As air masses go up, other air masses go down to ensure mass balance. The full circulation with the up- and downdrafts is well known among competition sailors: below the upwind side of the cloud, the wind speed is locally enhanced (Marchaj, 1996). Downdrafts may also be located at the cloud edges (Heus and Jonker, 2008; Heus et al., 2009; Mallaun et al., 2019), caused by the evaporation of the cloud liquid in to the dry surrounding air. Downdrafts can also reach the surface, when saturated downdrafts contain precipitation. Part of the precipitation evaporates on its way to the surface cooling the air, which becomes negatively buoyant enough to reach down to the surface. There, the cold air spreads into all directions, forming a so-called cold pool that largely impacts the local (surface) wind speed and direction.

Knowledge of the influence of clouds on local winds is useful to improve weather (and thus wind) prediction, which is needed for instance for air traffic control, air pollution, wind chill indices, or wind energy. Furthermore, surface winds influence the surface fluxes (of moisture, heat, and momentum) that subsequently affect the atmospheric stability, transport of water vapour and other scalars, and the formation of clouds, establishing a feedback.

There are several ways in which convection can influence the wind. First the air masses transport the local momentum (wind) vertically to different altitudes, just like they transport heat and moisture. While updrafts introduce weaker winds from

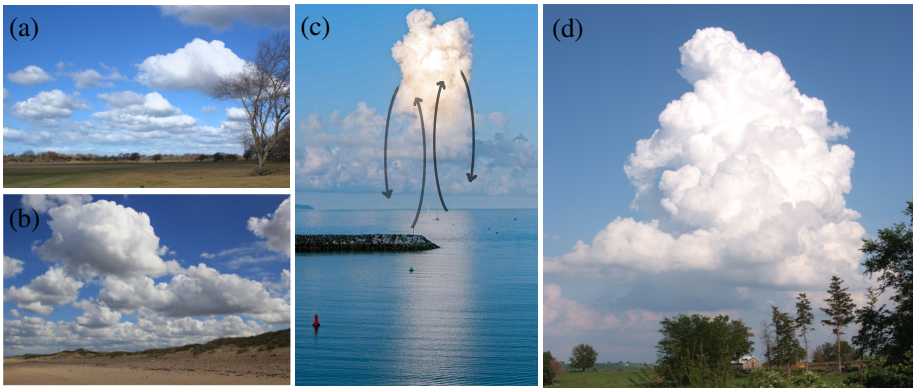


Figure 1.1: Examples of cumulus clouds. (a) Cumulus humilis is characterized by very small vertical development, often even shallower than on this picture. Cumulus humilis is often a forced cloud exists because of the inertia of the thermals feeding them from underneath. (b) cumulus mediocris (an active cloud) has moderate vertical development but does not precipitate. It often develops into congestus or cumulonimbus (thunderstorm cloud). (c) Towering cumulus congestus and its thermal circulation. (d) Cauliflower congestus that may develop into a cumulonimbus cloud. Pictures (b), (c), are obtained through the cloud appreciation society's cloud gallery. (b), (c), and (d) are copyrighted and printed with permission. Photographers: Julie Bestford (b), Tony Smith (c), and Carl Wycoff (d).

near the surface to higher levels, downdrafts introduce faster winds from aloft down to the surface. This is the process called convective momentum transport. It may be much more efficient through the faster precipitating downdrafts. Second, heating by condensation and evaporative cooling in clouds, as well as evaporative cooling in rain shafts, establishes heating and thus pressure gradients that drive the wind.

Convection is ubiquitous, and so are cumulus clouds. They form over the ocean and over land, in the mid-latitudes, sub-tropics, and tropics. The effect of clouds on the winds in mid-latitudes may differ from that in the sub-tropics, because they are embedded in different atmospheric flows. The mid-latitudes are known for its predominantly westerly flow that carries cyclones and anti-cyclones. The weather is dynamic, with fronts, periods of rain, clearings, low-pressure and high-pressure, and local convection. Day to day variations can be large. A strong diurnal cycle is present over land, with strong cooling during night and heating up quickly after sun rise, leading to strong diurnal variations in convection strength and hence in the depth of the convective boundary layer (e.g. He et al., 2013).

The sub-tropics are the inflow-branches of the Hadley circulation and are well-known for their steady easterly winds and ubiquitous fields of shallow cumulus clouds, making it an ideal laboratory for cloud and wind studies. Over sub-tropical oceans, the diurnality in surface temperature and convection strength is much smaller, although not insignificant (Brill and Albrecht, 1982; Vial et al., 2019). Cloud fraction and precipitation have a regular pattern with a maximum in the early morning and minimum in the (late) afternoon (Vial et al., 2019). The different atmospheric con-

ditions between mid-latitude land and tropical ocean may also show in the overall effect of transport of momentum (or wind mixing) through convection.

1.1.1 Convective momentum transport

The structure and dynamics of shallow convection and clouds depend on local processes such as turbulent mixing, microphysics and radiative forcing, processes that take place on scales much smaller than model grids (Neggers, 2015) which therefore need to be parametrized. The next sections detail the governing equations for momentum and explain the common methods to parametrize momentum transport, outlining our current understanding of convective momentum transport (CMT).

The equations of motion

The equations of motion (Navier-Stokes equation) is defined as

$$\frac{\partial u_i}{\partial t} + u_i \frac{\partial u_j}{\partial x_i} = -\frac{1}{\rho} \frac{\partial p}{\partial x_i} - g \delta_{i3} - f \epsilon_{ij3} u_j + \nu \frac{\partial^2 u_i}{\partial x_j^2}. \quad (1.1)$$

The first term represents the change in momentum in a given volume in time in all three directions ($i \in x, y, z$). The second term is the advection term whereby momentum can change due to the in- and outflow of momentum in all three directions. On the right hand side, the pressure gradient in all three directions predicts the movement from high to low pressure. The second term on the right-hand side is the gravitational force that only acts in the z -direction, as indicated by δ_{i3} , which drives vertical motion. The third term represents the Coriolis force that accounts for the rotation of the Earth, in which f is the Coriolis parameter and ϵ_{ij3} is the alternating unit tensor, which is 1, 0, or -1 depending on i, j, k . The Coriolis force acts perpendicular to the wind vector and its strength is proportional to the wind speed. $\nu \frac{\partial^2 u_i}{\partial x_j^2}$ represents the viscous stress that takes place on a molecular level (Garratt, 1992).

Usually a few simplification are applied before modeling the flow. Using Reynolds decomposition, the variables can be separated in a mean flow component and a fluctuating part:

$$\phi = \bar{\phi} + \phi', \quad (1.2)$$

where the average can take various mean forms: as ensemble average, time average, 1D (line), 2D (area) or 3D (volume) average, depending on the application (Garratt, 1992).

The fluid is assumed to be incompressible and the Bousinesq approximation is used, which states that density fluctuations can be neglected except in combination with the gravitational acceleration. Furthermore, viscous molecular stress is neglected since it is only important in the lowest few millimeters above the surface. After applying Reynolds decomposition and averaging, we obtain the Reynolds averaged Navier-Stokes equations:

$$\frac{\partial \bar{u}_i}{\partial t} + \bar{u}_i \frac{\partial \bar{u}_j}{\partial x_i} = -\frac{1}{\rho} \frac{\partial \bar{p}}{\partial x_i} - g \delta_{i3} - f \epsilon_{ijk} \bar{u}_j - \frac{\partial \overline{u'_i u'_j}}{\partial x_j}. \quad (1.3)$$

This equation contains most of the terms that are also present in Equation 1.1, but for the first moment (mean). The additional (and last) term on the right hand side represents turbulent transport and is also known as the Reynolds stress.

For Large Eddy Simulation (LES) models, a similar equation is solved. There, the variables are separated in a "resolved" or "filtered mean" variables, and sub-filter scale variables need to be parametrized. LES typically has grid-scales down to the order of 50 m. In other words, all "large" turbulent eddies with scales beyond 100 m are resolved, while small turbulent eddies that fall within a model grid box are parametrized using models for fine-scale turbulence. LES captures up to 90 % of the turbulent transport as it is able to resolve the majority of the convection as well as the largest, most energetic turbulent eddies (Heus et al., 2010).

In this thesis we are most interested in the Reynolds stress term in equation 1.3. Depending on the resolved length scale or the model type that is run, this term can include either transport by local shear-driven turbulence or also non-local mixing through convection. Whereas LES can resolve most convection and part of the turbulent eddies, numerical weather prediction models or climate models cannot. Whereas LES uses only a local mixing parametrization for the smaller eddies, NWP models have much coarser grid sizes and therefore need parametrization for both local mixing and convection. Local mixing is typically parametrized using K-diffusion models (also known as K-theory or eddy diffusivity), whereas convective transport is commonly parameterized with the mass flux approach. In the surface layer, a parametrization is always required, and it is usually based on Monin-Obukhov similarity theory. Figure 4.1 shows the various layers as well as an impression of convective and small scale turbulent mixing. Next paragraphs explain the three parametrization schemes.

Eddy diffusivity approach

Eddy diffusivity approach, also known as K-theory and gradient transport, is the most common first-order closure scheme that approximates turbulent vertical transport (turbulent flux) of any scalar ϕ in the boundary layer over relatively short (local) distances:

$$\overline{w' \phi'} = -K \frac{\partial \bar{\phi}}{\partial z} \quad (1.4)$$

This equation links the turbulent flux to the average gradient, whereby larger gradients correspond to larger fluxes due to an increase in ϕ' . The parameter K is known under various names, among the most common are eddy viscosity and eddy diffusivity. Eddy diffusivity approach only supports down-gradient transport. Therefore $K > 0$ and acts to reduce the gradient. An intuitive example may be given

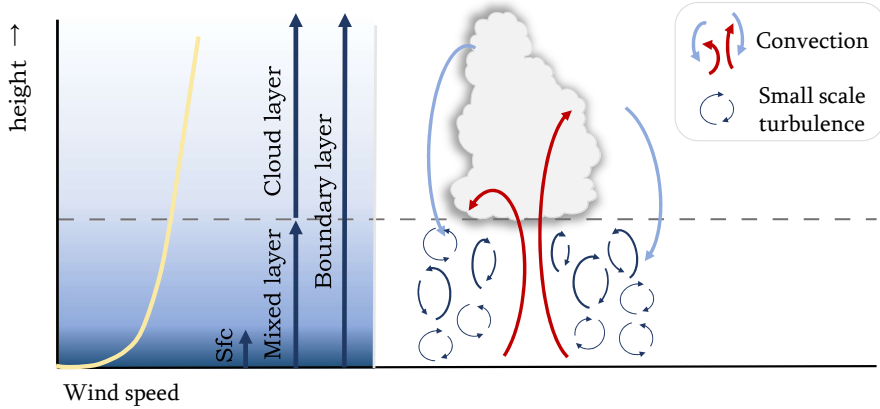


Figure 1.2: Convection and (small scale) turbulent mixing are important for transport of scalars and momentum. Whereas convection transports over longer vertical distances (length-scales), small eddies mix very locally. Momentum transport in the surface layer is commonly described by Monin-Obukhov similarity functions that depend on the local gradient of wind in this layer. In the mixed-layer and cloud layer a separate scheme is present for convective (mass flux) and local mixing (K-theory).

for temperature. Suppose an air parcel rises a small distance, so $w' > 0$. When the temperature decreases with height (as in an unstable atmosphere), the temperature of the original air parcel is larger than the temperature at the higher level, so $T' > 0$. Thus, $\overline{w'T'} > 0$. A negative $\frac{\partial T}{\partial z}$ and a positive K lead to a down-gradient flux. For up-gradient or counter-gradient transport, the opposite is true and the gradient is enhanced.

A few words of caution: First, K-theory is formulated analogous to molecular diffusion ($\overline{u'w'} = -\nu \frac{\partial u}{\partial z}$), but turbulence is much more efficient in mixing than diffusion (so K is orders of magnitudes larger than ν). Whereas viscosity is a property of the fluid, the analogous K is a property of the flow that varies with turbulence and is often parameterized as a function of atmospheric stability. Second, K-theory works well when mixing lengths are small and transport happens locally. The approach fails when larger-size eddies are present in the flow (p. 204 Stull, 1988). To represent the local and non-local flux more accurately, the eddy diffusivity is often combined with non-local transport. Various widely-used non-local approaches exist, especially for moisture and heat, among others those of Troen and Mahrt (1986) and Holtslag and Boville (1993), and Brown and Grant (1997). We mostly consider the mass flux approach (Siebesma et al., 2007) in this work, which is explained in the next section.

Mass flux approach

Thermals are mainly responsible for the transport between the well-mixed (sub-cloud) layer and the cloud layer. The mass flux, as proposed by Betts (1973), makes use of the fact that a thermal transports mixed-layer air through cloud base into the cloud (layer), effectively transporting mass over large vertical distances. Because we are interested in the flux throughout the sub-cloud layer and within the cloud layer, the flux of an arbitrary field ϕ can be expressed in terms of the fractional area of the updrafts (a_u), the vertical velocity of the updrafts (w_u, w_{env}) and the difference of the value of the field in the updraft and its environment ($\phi_u - \phi_{env}$):

$$\overline{w'\phi'}_{MF} = a_u(w_u - w_{env})(\phi_u - \phi_{env}). \quad (1.5)$$

If the fractional updraft area is small, i.e. $a_u \ll 1$, the flux can be further simplified to:

$$\overline{w'\phi'}_{MF} \simeq a_u(w_u - \bar{w})(\phi_u - \bar{\phi}) = M(\phi_u - \bar{\phi}), \quad (1.6)$$

where in the second step the convective mass flux (M) has been introduced. This result is extremely desirable for a parametrization point of view as now only a parametrization of the mass flux and the updraft field ϕ_u is required.

The mass flux was originally developed to represent the vertical transport of conserved variables by (deep) cumulus clouds (Arakawa and Schubert, 1974; Tiedtke, 1989), but has also been demonstrated to yield good results in shallow cumulus transport (Siebesma and Cuijpers, 1995). Its success can be explained by the strong correlation between heat (or moisture) with the updraft velocity that has a bimodal structure in the joint probability density function (Siebesma et al., 2007). The two modes correspond to a strong positive updraft that contains warmer and moister air than the environment and a downward return flow that is typically colder and drier.

Also momentum is often parametrized using the mass flux approach, treating momentum transport that is carried by thermals as scalar. For deep convection, it has been shown that pressure gradients cannot be neglected (LeMone, 1983), which led to an additional term in the parametrization that accounts for the pressure gradient, although it poorly captures the evolution in mesoscale systems (Badlan et al., 2017). Using LES, Brown (1999) showed that an in-cloud pressure gradient term also dominates the momentum budget in shallow cumulus convection, although this term is often neglected in their parametrization. Further benefits and caveats of the mass-flux approach using LES studies on shallow CMT are discussed in section 1.1.2.

Monin-Obukhov similarity theory

At the surface, turbulent fluxes are zero by definition because resolved fluctuations in the vertical velocity are zero at the surface. In models, whether LES or NWP, the turbulent flow from the surface up to the local roughness length is typically not resolved. Therefore, the heat, moisture fluxes, and the surface friction velocity in the

surface layer (~ 200 m) need to be parametrized. Monin-Obukhov similarity theory (MOST) provides a method to estimate turbulent fluxes in the surface layer (also called constant flux layer).

MOST assumes that the vertical gradient of the field-averaged wind should solely depend on the height above the surface, as it limits the (vertical) length-scale of the eddies that are responsible for turbulent transport. Two non-dimensional groups are formed, on which the similarity is based: the stability parameter and the ratio between the fluxes and the mean gradients. For momentum the flux gradient relation reads:

$$\frac{kz}{u_*} \frac{du}{dz} = \phi_M(z/L), \quad (1.7)$$

where z is height, k is the von Kármán constant, u_* the friction velocity, du/dz represents the shear (at height z), and ϕ_M is a similarity function that depends on the atmospheric stability (z/L), in which L is the Obukhov length (Moene and van Dam, 2014). Many empirical studies have aimed to find the similarity function. A well-known representation of the flux-gradient relationships is that by Businger-Dyer (Dyer and Hicks, 1970) that depend on the atmospheric stability:

$$\phi_M = \begin{cases} (1 - 16z/L)^{1/4} & \text{for } -2 \leq z/L < 0 \text{ (unstable)} \\ 1 + 5z/L & \text{for } 0 \leq z/L < 1 \text{ (stable)} \end{cases} \quad (1.8)$$

The relationships are well-defined in a limited range in which they have been tested, although the relationships do not work well in very weak wind conditions, or when u_* is zero. For a thorough overview of the history of MOST, its development, and universal functions found in empirical studies, see Foken (2006).

At the surface fluxes are typically calculated using the bulk flux formulation, which for momentum reads:

$$F_{s,M} = -C_M \langle U_1 \rangle (\tilde{U}_1 - U_0). \quad (1.9)$$

The flux (left-hand side) depends on the average drag coefficient (C_M) that can be determined using the (horizontal averages of the) Obukhov length and friction velocity that are determined using MOST, the wind speed at the first model level ($\langle U_1 \rangle$) as well as on the difference between the surface wind (U_0 , which must be zero over land) and the wind speed at the first height level. When the (horizontal average) Obukhov length and friction velocity are found, an average drag coefficient can be determined (Heus et al., 2010). Similar equations exist for the scalar parameters, but where the surface wind (U_0) is zero, moisture content and temperature are usually non-zero.

1.1.2 Insights from large eddy simulations

Studies that have explored shallow CMT have mostly done so using LES. LES studies are often based on measurement campaigns, such as the BOMEX case of shallow non-precipitating convection over the sub-tropical oceans (Siebesma1995). Based on this case, Brown (1999) was one of the first to study CMT in shallow convection, looking at the changes in momentum flux while varying the shear profile in magnitude and sign. He found that the scalar transports were little affected by shear: because buoyancy-production of turbulence dominated over shear-induced turbulence, momentum fluxes changed considerably. Brown (1999) hinted that with larger shear magnitudes, the shear production of turbulence likely increases with respect to the buoyancy. Later studies by Helfer et al. (2020) showed that cumulus growth, relating to convection strength, reduces under shear conditions which strengthens this argument.

From budget analysis (also based on BOMEX), Larson et al. (2019) show that turbulent advection and buoyancy terms are crucial for the occurrence of up-gradient momentum transport, emphasizing the importance of mixing on larger length scales, and hence the use of non-local parametrization schemes. For momentum, the mass flux parametrization is typically used. Schlemmer et al. (2017) looked into various cases of CMT, all based on previous measurement campaigns.

Schlemmer et al. (2017) highlighted the importance of clear-sky and small scale turbulence in contributing to the momentum flux even in the cloud layer. Using two idealized cases (RICO and CONSTRAIN), Schlemmer et al. (2017) also emphasized that knowledge of the in-cloud momentum transport at cloud base could lead to an improvement of the overall modeled flux in the cloud layer.

An earlier study by Zhu (2015) decomposed the resolved LES flux into different scales for several cases of stratocumulus, shallow cumulus, and deep convection. He made a similar point that, other than for the thermodynamic variables, turbulence cannot be neglected. Therefore, applying only a mass flux parametrization is not ideal for momentum transport. Furthermore, Zhu (2015) addressed a number of reasons to be cautious with approximating momentum flux using the mass flux approach:

1. Other than with thermodynamic variables, the wind structure shows large variation from case to case.
2. When a convective plume rises adiabatically, it conserves the reversible thermodynamic properties (to a good approximation), suggesting there is a good correlation between the updraft and the conserved variable. Therefore, the transport of these conserved variables can be explained by a few strong updrafts. Because the updrafts are thermally driven and not by dynamic forcing, the thermals do not necessarily possess similar horizontal momentum. The large variation in momentum fluctuations may lead to a small net flux of momentum due to the presence of both positive and negative perturbations that cancel out.

3. Horizontal momentum components are not conserved in adiabatic rising plumes. The pressure perturbation force impacts the momentum components even in shallow convection, as also pointed out by Brown (1999), and can thus cause differences in momentum flux at different heights.
4. Small-scale eddies transport momentum more efficiently than coherent plumes (which has also been observed in the surface layer by Li and Bou-Zeid (2011)). Shear-induced eddies that are typically small-scale and transport momentum efficiently may overlap the large convective plumes, incidentally making the mass flux work for momentum.

Periodic boundary conditions, simplified or highly smoothed large-scale wind forcing, limited domain size, and limited resolution, may all contribute to the fact that LES is not an accurate representation of the multi-scale flows present in nature (e.g Agee and Gluhovsky, 1999; Stevens et al., 2002; Mazzaro et al., 2017). Although LES developments are moving towards realistic simulations (e.g. Botnick and Fedorovich, 2008; Liu et al., 2011; Mazzaro et al., 2017; Sakradzija and Klocke, 2018; Dixit et al., 2021; Bauweraerts and Meyers, 2019), observations can be valuable in understanding momentum transport, as they capture the complexity of reality. Next section explains the common means of observing wind (profiles) and momentum transport.

1.1.3 Observational approaches

There are many platforms that can observe wind and its transport. This section details the measurement techniques that are used for each instrument, the benefits and limitations, and the most important findings from studies on shallow CMT using observations.

Observation sites, such as the Cabauw observatory, typically have a measurement tower that measures wind at various heights. Traditionally, cup anemometers and a wind vane are deployed to measure wind speed and direction. Nowadays, mainly sonic anemometers are used. They consist of three speakers and three microphones. Emitting sound at one end and recording at the other allows to calculate the three wind components. In both methods, momentum fluxes are calculated using the eddy covariance technique (see Wutzler et al. (2018) for an overview).

Such sites are usually based on land surface, which makes it easy to maintain compared to over the ocean. Furthermore, they are set-up with many co-located measurements and for long time spans (Cabauw was set-up more than 50 years ago (Bosveld et al., 2020)), allowing a wide range of applications and enabling statistical analysis. A drawback is that measurements are limited in height, as towers do not extend more than a few hundred meters. Furthermore, they provide only information on one location, whereas a network would provide a better overview of the environment.

Using radiosondes, the wind profile over a wide range of altitudes can be obtained by tracking the location of the sonde with time using the geopositioning system

(GPS) or radio direction finding (RDF). Alternatively, these type of measurements are used as dropsondes, releasing them from aeroplanes. In large field campaigns, such as BOMEX, TOGA COARE or the recent EUREC4A campaign, a specific pattern of radiosondes or dropsondes is released for momentum budget calculations (Holland and Rasmusson, 1973; Carr and Bretherton, 2001; Nuijens et al., 2022).

Deploying similar sonic anemometers on board an aeroplane allows measurements of turbulence and winds at a given height level across a distance on the order of 10 - 100 km. Flights are generally limited to a handful of case studies, due to the high costs.

A more continuous measurement over large vertical distances can be accomplished using a Doppler wind lidar (DWL). The DWL sends out a light pulse and the return signal contains a Doppler shift because the light scatters back on moving aerosols, from which the wind velocity is calculated. Sending out the pulse along a cone, it can obtain all three wind components in a larger air volume. DWLs are widely applied in the wind energy industry, for instance to study wind turbine wakes that cause power losses within the wind park, to estimate fatigue loads, for power prediction in the presence of a low level jet, or uneven loading on the rotor due to shear (Banta et al., 2013; Scholbrock et al., 2016; Pichugina et al., 2017; Maulik et al., 2021). DWLs are also taken aboard aeroplanes where it measures winds in a range of weather phenomena, among which tropical cyclones, gravity waves, and terrain flow (e.g. Krishnamurthy et al., 2013; Witschas et al., 2017; Bucci et al., 2018). Even momentum fluxes can be obtained from DWL (Kropfli, 1986; Eberhard et al., 1989).

With the launch of the AEOLUS satellite, carrying the first wind lidar from space, a big leap forward is taken to increase the amount of measured wind profiles worldwide, especially over the oceans where it is difficult to measure. But AEOLUS is less useful for local wind studies: validating missions using collocate airborne wind lidar observations using a prototype of the satellite instrument showed a bias of 2.6 m s^{-1} of the Aeolus winds in the Rayleigh spectrum, compared to that of the airborne Rayleigh retrieval (Witschas et al., 2020; Skofronick-Jackson et al., 2021; Lux et al., 2022). Furthermore, the horizontal resolution of 90 km (Rayleigh) to 10 km (Mie) and a vertical resolution between 1 km (Rayleigh) and 0.5 to 1 km (Mie) (Witschas et al., 2020) are too coarse for capturing cloud related boundary layer turbulence.

One of the few observational campaigns that targeted momentum transport in shallow cumulus conditions is the study by LeMone and Pennell (1976). Their flight campaign targeted the relationship between boundary layer turbulence and the overlying clouds. They showed that even in shallow convection, the momentum flux does not need to act to reduce the wind gradient (down-gradient transport), but can occasionally enlarge the gradient (up-gradient transport). This was only thought possible for deep convective cases (LeMone, 1983; Moncrieff, 1997). Other studies also report momentum fluxes (Pennell and LeMone, 1974; Nicholls and LeMone, 1980; Nicholls and Readings, 1981; Thompson et al., 1980), but do not specifically explore their relation to cloud convection.

Only recently, a few campaigns have been carried out to study clouds in relation to wind. One of them was especially designed for this thesis, the CloudBrake

campaign, that deployed two aircrafts that flew in three different cloud fields. One airplane measured wind profiles using down-looking wind lidar, the other took high-frequency in-situ measurements, much like LeMone and Pennell (1976).

Furthermore, a large field campaign, EUREC4A (and the US counterpart ATOMIC), took place in the trade wind region near Barbados early 2020. Having abundant simultaneous measurements from aeroplanes, ships, flying and sailing drones, and buoys the role of shallow clouds in a changing climate is investigated. Convective momentum transport in relation to these small convective clouds can be studied using cloud radar, wind lidar, and in-situ turbulence measurements like in LeMone and Pennell (1976), as well as 2000 dropsondes that have been released from aeroplanes. This is a great advancement for CMT studies as a month of time series significantly increases the available observational data. This thesis also reports findings from this data set, but an extensive use of the EUREC4A / ATOMIC dataset is expected, since BOMEX, RICO, and other older cases are still studied.

1.2 Research goals

To advance the understanding of convective momentum transport in shallow cumulus conditions, observations are complemented by pseudo-observations from LES. Where observations are limited in their vertical extent and usually target a small volume or provide a point measurement, LES can look at a larger area and at higher altitudes. Here, LES is not confined to idealistic cases, but rather simulates realistic days that encompass a large variety of atmospheric conditions and cloud fields. The combination of LES and observations provide a good foundation to answer the following questions about convective momentum transport:

1. How does the redistribution of sub-cloud momentum fluxes by turbulent transport change under various cloud- and weather regimes?
2. What is the interplay between the wind profiles and the momentum mixing?
3. How do different scales contribute to momentum transport?
4. Can new wind profiling measurements add to the understanding of thermal circulations on convective and meso-scales?

1.3 Outline

The remainder of the thesis consists of two papers that are published and peer-reviewed and a manuscript close to submission. With **Chapter 2**, we start in Cabauw, The Netherlands, with almost a decade of observations near the surface – in the lowest 200 m. An equally long time series of Large Eddy Simulations at Cabauw accompanies the measurements, which allows us to look at wind and momentum transport above 200 m. On mid-latitude land, we need to deal with a strong diurnal cycle and many different weather events, challenging us to find the (expected) small signal

induced by shallow cumuli in the many processes that have (larger) effect on the wind. Due to the long time series, we were able to do a statistical analysis over various cloud regimes. Averaging over all weather conditions enables us to isolate the cloud effect, with which we address question 1. Question 2 is also addressed for the surface layer.

Chapter 4 uses data from the EUREC4A campaign. At the tropical ocean near Barbados, a much weaker diurnal cycle, a more predictable wind, and a relatively steady cloud deck are present. About a month of data was collected during this campaign. Individual clouds were extracted from the dataset, and grouped according to their vertical extent. Because convection is still relevant during the night, also night-time clouds are included in the analysis, which provided a sufficient large data set to answer question 1 and 4.

Last, **Chapter 3** presents three case studies of cloud regimes from suppressed convection with shallow clouds to enhanced convection after a cold front in Germany. This time, the focus lies with the upper part of the sub-cloud layer and the cloud layer. The three cases provide a small insight into the variation in momentum transport between clouds of different thickness (even in similar conditions), and answer question 1,2, and 4.

Before expressing my thanks to the many people that supported me during my PhD, a summary of the main findings and an outlook for future research is provided (**Chapter 5**).

2

Surface-layer wind shear and momentum transport from clear-sky to cloudy weather regimes over land

2.1 Introduction

Accurate predictions of wind speed and wind direction near the surface are important, for instance to estimate energy generation in wind farms or to predict surface stress, heat and moisture fluxes that influence a range of atmospheric processes. The short-term local wind forecast relies on many processes, of which several are not resolved in numerical weather prediction (NWP) models but parameterized. Unresolved parameterized processes that impact the winds are surface drag and shear-driven turbulence, as well as convection and gravity waves. Over land the deepening of the boundary layer due to turbulence and dry convection is typically accompanied by the development of shallow cumulus clouds. The objective of this study is to investigate the relationship between wind shear and momentum fluxes with cloud or weather regimes and identify whether convective cloud regimes in particular, as opposed to clear sky regimes, have a different structure of wind and momentum flux near the surface.

There are a number of ways through which winds and clouds relate. First of all, clouds are inherently coupled to certain wind or weather regimes. For instance, in the Netherlands, cloudy days typically have westerly winds bringing moist air masses

This research has been published as: Koning, A. M., Nuijens, L., Bosveld, F. C., Siebesma, A. P., van Dorp, P. A., & Jonker, H. J. J. (2021). Surface-layer wind shear and momentum transport from clear-sky to cloudy weather regimes over land. *Journal of Geophysical Research: Atmospheres*, 126, e2021JD035087. <https://doi.org/10.1029/2021JD035087>

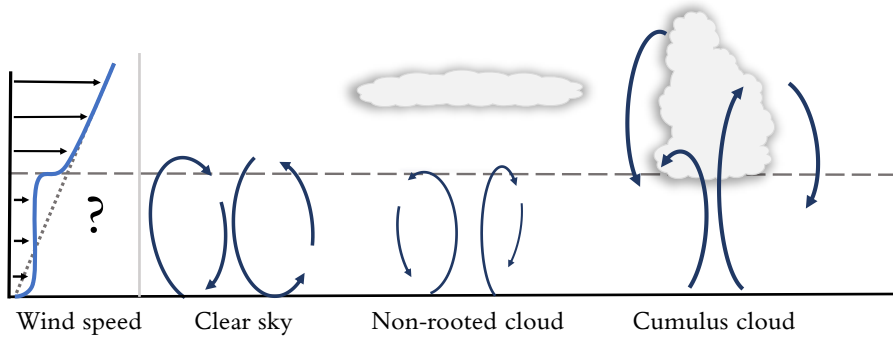


Figure 2.1: The main cloud regimes and associated boundary-layer scale circulations are shown. Stratus layers may obstruct a large part of the solar radiation, reducing the updraft strength. Thicker arrows correspond to stronger up- and downdrafts. The dashed horizontal line indicates the top of the mixed-layer (η). On the right, we specify the definitions of the boundary layer (for the cumulus regime), mixed-layer, cloud layer and surface layer (indicated as "Sfc" and taken as the layer up to 200 m). In the cumulus cloud regime, the mixed-layer is identical to the sub-cloud layer, whereas in the clear-sky and non-rooted cloud regime the mixed-layer comprises the entire boundary layer.

onto land, whereas days with easterly winds and high surface pressure tend to be associated with clear skies. Significant (deep) convective and stratiform cloudiness are associated with the passage of storm systems coming from the west, while congestus clouds prevail after cold-front passages and in cold air outbreaks from the north.

Second, as illustrated in Figure 2.1, clouds alter the surface energy budget through radiation, which influences turbulence and convection in the boundary layer. He et al. (2013) contrasted entirely cloud-free days (clear skies) over the Netherlands with days that have persistent low level cloudiness (cloud base height < 1.5 km, at least 10 cloud base detections out of a maximum of 20 detections per 10 min) and found that winds in the surface layer are less well-mixed (have larger shear) on cloudy days, because of reduced incoming solar radiation at the surface and reduced surface buoyancy fluxes, consistent with LES of (Brown and Grant, 1997).

Third, shallow cumulus clouds are naturally rooted within the surface layer and develop as a result of thermal circulations driven by the surface buoyancy flux (that may already be larger than on clear sky days). The turbulent mixing that drives clouds will also drive different winds. Detecting the convective plumes using wavelet analysis, Schalkwijk et al. (2010) exposed the thermal structure in the boundary layer up to 200 m (in observations), as well as the full boundary layer (in LES). They found that thermals are responsible for 40% of the total vertical heat transport. Thermals can however also violate the often used Monin-Obukhov Similarity Theory (MOST) to

estimate fluxes in the surface layer. Fodor et al. (2019) found that convective scale up and downdrafts may not have locally determined properties and may produce deviations from MOST estimated buoyancy flux in the limit of free convection. Even when MOST still holds, Li and Bou-Zeid (2011) found that momentum transport in the near surface layer (<10 m) became less efficient when the atmosphere became more unstable, opposed to buoyancy. They explained the lower efficiency by the increased importance of transport through convective plumes rather than through small-scale turbulent eddies.

Fourth, convective clouds may deepen the boundary layer and lead to deeper vertical mixing of scalars and wind Stevens (2007). Clouds may also alter turbulent circulations through mesoscale organization Bretherton and Blossey (2017); Holloway et al. (2017) or through evaporation-driven downdrafts, for instance, the gustiness associated with density currents driven by evaporation of rain (Jabouille et al., 1996, e.g.). Early flight campaigns showed that organization may change the turbulent momentum flux. LeMone and Pennell (1976) measured in three convective situations over the ocean near Puerto Rico: on a suppressed day with almost no clouds, a day with shallow roll convection, and a day with enhanced shallow popcorn convection and numerous clouds. The two days with suppressed convective conditions had down-gradient diffusive fluxes that act to reduce the wind shear, whereas the case with enhanced convection showed significant counter-gradient transport, especially below and near the bases of clouds, something that is typically associated with organized systems of deep convection LeMone (1983); Rotunno et al. (1988); LeMone and Jorgensen (1991); Wu and Yanai (1994); Tung and Yanai (2002). Convective cloud organization is currently an important topic in studies of trade-wind convection, where mesoscale variability in cloud, rain, wind and scalars is pronounced Bony et al. (2017b).

Over land such studies are rarer Moeng and Sullivan (1994); Zhang and Klein (2013); van Stratum et al. (2014) and the relationship between near-surface wind (wind in the lowest 10% of the mixed layer) and convective or boundary layer tops is not well described. Much of what we know about momentum transport by shallow convection in fact stems from Large Eddy Simulation of cumulus convection over the ocean (ATEX, BOMEX, RICO) Brown (1999); Schlemmer et al. (2017); Zhu (2015); Saggiorato et al. (2020). Even for the ocean, such cases are highly idealized, with constant large-scale (wind) forcing and domains too small to allow for convective organization. Zhu (2015) exemplified just how different the simulated turbulent flux profiles are and can even change sign depending on cloud regime and the scales of the transport e.g., small-scale shear-driven eddies or larger coherent circulations. This motivates studying momentum flux profiles for a wider variety of cases and conditions as present in real nature.

In our study, we use a long climatology (2009 – 2016) of cloud and wind measurements collected at Cabauw (now part of the Ruisdael observatory (<https://ruisdael-observatory.nl/>)) to study how near-surface wind and momentum flux change with cloud regimes. Measurements by a ceilometer and 200 m tall measurement tower are complemented by small-domain (8.2 x 8.2 km²) LES runs of the

same long period. The LES output provides insight into the turbulence processes, such as the momentum flux profiles, extending beyond 200 m. We distinguish non-convective days, clear-sky days, and days with clouds that are rooted in the surface layer (which we label convective clouds). Our analysis aims to answer how wind shear in the surface layer differs between these regimes, and whether convective cloud regimes are accompanied by different wind mixing behavior than the clear-sky regime, after accounting for differences in surface buoyancy fluxes, atmospheric stability and large scale winds.

In the next section, we will describe the measurements taken at Cabauw, the set-up of the LES and the selection method for the different cloud regimes. The cloud regimes as identified in the observations and in the LES will be verified and compared. In the results we first describe the differences in wind mixing and momentum flux in the surface layer, using data from both observations and LES. Second, we will discuss differences for the entire boundary layer, for which only LES results are used. Conclusions are presented in section 4.

2.2 Data

2.2.1 Cabauw (Ruisdael) observational data

The observational data contain 10-minute interval measurements of wind speed and direction taken at the tower using cup anemometers and wind vanes. The anemometers and wind vanes are mounted on 10 m long booms that are positioned at 40, 80, 140 and 200 m height. Because wind measurements are sensitive to flow obstructions, only the undisturbed measurements are selected from the three booms that measure wind direction and from two booms measuring wind speed. Winds at 10 and 20 m are measured at three different masts (70 m and 140 m NE, 30m SE from the main mast) to avoid flow disturbance by main mast itself and the small buildings attached to the main mast. The selection of these separate masts depends on the wind direction. Momentum fluxes are estimated from wind measurements of sonic anemometers located at 3, 60, 100 and 180 m height, and are available every 10 minutes. They are corrected for streamline tilt due to flow obstruction around the masts and by instruments. Low frequency losses are corrected for according to Bosveld (1999). Further details can be found in Bosveld et al. (2020)

Cloud base height (cbh) is measured by a LD40 ceilometer. The LD40 is situated on a field to the south of the tower, within 50 m from the mast, which justifies synergistic use of the data Bosveld (2020). On this field, also the net radiation and net surface fluxes are measured. The ceilometer measures back-scatter intensity from particles using a 855 nm wavelength. The maximum range (detection height) is 13600 m with a resolution of 7.5 m. It emits 65000 pulses every 15 seconds, and returns three cloud base heights, as well as vertical visibility and a precipitation index. We only use the first (lowest) measured cloud base, because the signal attenuates considerably after penetrating a cloud. Furthermore, we disregard any back-scatter retrievals from altitudes above 5 km, as convective clouds have cloud bases below 5 km and

we assume that clouds above 5 km do not have an influence on the mixed layer other than through radiation. The first detected cloud base height is not necessarily the height that corresponds to the lifting condensation level, where one expects convective clouds to have their base. It can correspond to cloud edges, sides of slanted clouds, or stratiform outflow. In section 2.3, we describe in more detail how we use this information to classify cumulus days. Note that we make a clear distinction between cloud cover and cloud fraction. We refer to cloud cover as the areal fraction of the sky that is covered with cloud, which is measured by the ceilometer and can be calculated from the LES output. We use cloud fraction only to refer to the amount of cloud at any height; such profiles are only available from the LES.

2.2.2 Large Eddy Simulations

Our LES data is generated with the commercially-used GPU-Resident Atmospheric Simulation Platform (GRASP), whose first version was based on the Dutch Atmospheric Large Eddy Simulation (DALES). For more information on DALES we recommend reading Heus et al. (2010). GRASP has been modified to run on Graphics Processing Units (GPUs) instead of Central Processing Units (CPUs), increasing the computational speed considerably, making it suitable for operational use in the wind energy industry. In our case, GRASP is run in hind-cast mode, obtaining its daily initial and large-scale forcing conditions from ECWMF's (European Centre for Medium-Range Weather Forecast) ERA5 data. This hourly forcing includes the radiative heating profiles, which means that the surface energy budget does not "feel" the clouds resolved by LES, but those produced by the Integrated Forecasting System (IFS). We will see later that this does not lead to a major difference as compared to the observations. For more information on the coupling to ERA5, please see Schalkwijk et al. (2015).

To enable the long period of daily hindcasts, the computations are limited to a domain of $8.192 \text{ by } 8.192 \text{ km}^2$ by 5.079 km with a horizontal resolution of 64 m and a vertical resolution that decreases with height from 16 m near the surface to 80 m at approximately 5 km. This is notably smaller than what is currently common, but in line with benchmark LES studies Stevens et al. (2001); Siebesma et al. (2003). Recently, Schemann et al. (2020) reflected on challenges in comparing point observations to large-domain LES, in which mesoscale flows evolve freely. They show that small domains remain closer to the synoptic conditions and therefore they are more suitable to compare with local observations.

The LES uses the sub-grid scheme of Sullivan et al. (1994). At the surface, MOST is applied in a local fashion, enabling a proper interaction between the surface and the overlying convective turbulence fields. Additionally, a heterogeneous surface model is applied to every grid box individually, following TESSEL ECMWF (2015), using high resolution land use data from the CORINE (<https://land.copernicus.eu/pan-european/corine-land-cover>) data-set. Apart from ensuring a correct local surface roughness, the heterogeneous surface conditions ensure a sensible roughness experienced by the in-flowing wind. This roughness is similar to the aver-

age roughness in the domain due to periodic boundary conditions, which is reasonable as the region around the domain are quite similar to the conditions at Cabauw.

Each run is initialised at 21:00 UTC and runs to 23:59 UTC the next day. To avoid spin-up influences and overlap in the data, we use the output data from midnight to midnight. Data output consists of domain and hourly averaged profiles of wind, temperature, and humidity for the exact location of the Cabauw tower and liquid water path (LWP) snapshots are given every 10 minutes for the full horizontal scale of the domain, from which cloud cover is estimated.

2.3 Cloud regime classification

We identify three different cloud (weather) regimes:

1. Clear-sky regime (dry convective boundary layer)
2. Convective cloud (shallow cumulus regime)
3. Non-convective (other) cloud regime

The dry convective regime is assumed to represent convection in a boundary layer whose top lies below the lifting condensation level. The convective clouds are separated into two regimes; one with a cloud cover ranging between 5 – 30%, associated with very shallow convection (or forced clouds, such as cumulus humilis, to mediocris), the second with a cloud cover between 30 – 70%, which may be associated with larger clouds or cloud decks approaching stratocumulus. Convective days with more than 70% cloud cover consist of both stratocumulus clouds and deep convective clouds that often reach the top of the domain. Having its top at ~ 5 km, these clouds are likely not well-captured. Also, after the visual inspection, which is described next, we found that days with large cloud cover that are classified as convective clouds by the algorithm have a larger resemblance with stratus clouds that do not have a convective origin (both in observations and LES). This category is excluded in the remainder of the paper.

The visual classification has been executed for each day in 2016, to validate the automatic algorithm. For observations we used the ceilometer backscatter to inform us about the growth of the boundary layer, whether cloud base grows with the boundary layer and whether there are multiple cloud layers. A hint of the presence of different cloud types can also be obtained. Satellite images (NASA's Moderate Resolution Imaging Spectroradiometer (MODIS) satellite images from Terra and Aqua, see <https://worldview.earthdata.nasa.gov/>), as well as the cloud camera provide further insight into the cloud type and the general cloud conditions around Cabauw. In the visual images and videos, we look at the cloud base, which should be flat for convective clouds, and at the structure: white tufts with cotton candy appearance, and sharp cloud edges. Stratus clouds can be easily identified as a uniform grey cloud without sharp cloud edges, usually stretching out over a long distance. In LES, both cloud movies and the evolution of the cloud fraction profile are used for the

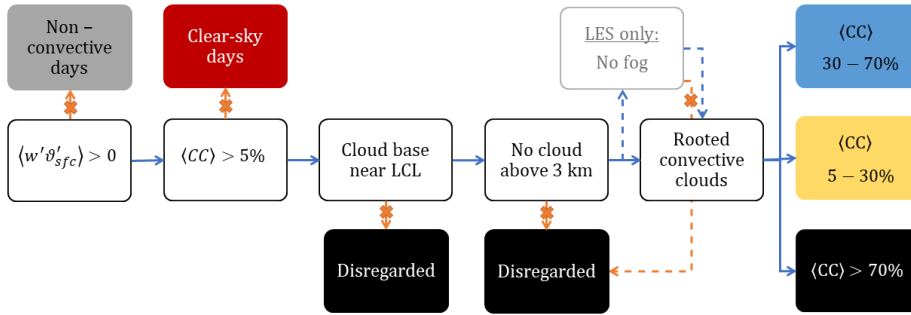


Figure 2.2: Process chart of the cloud regime classification. White boxes indicate the process steps, blue arrows indicate the criterion is met, red arrows indicate that the criterion is failed. The colored boxes show the cloud regimes that are selected, and the black boxes (including the convective cloud regime with cloud cover larger than 70% indicate the disregarded days. Selection is between 10–16 UTC. Further explanation is found in the text.

Table 2.1: The total number of convective cumulus and clear-sky days are shown below for both observations and LES.

Class	Obs	LES
Non-convective days	625	378
Convective days with clear-sky	316	482
Convective days with clouds	2207	2403
Total number of days	3148	3263

manual classification. For cumulus clouds, the cloud fraction usually peaks around the mixed-layer height (defined as the height of minimum buoyancy flux), becoming smaller towards the top. With cumulus congestus, another cloud fraction peak can be present higher up, characteristic of stratiform outflow.

The procedure for the automatic classification is shown in Figure 2.2. The white boxes indicate the process steps, the colored boxes show the cloud regimes that are selected, and the black boxes show days that were rejected from the dataset. The brackets $\langle \cdot \rangle$ indicate averaging between 10-16h UTC (12-18h local summer time, 11-17 local winter time), for which the cloud regimes will be contrasted. This time interval includes the mean local solar noon at 11:40 UTC, as well as the cumulus clouds that form before noon and disappear around 12-15h UTC (season dependent). We first select all non-convective days with a negative average surface buoyancy flux. The clear-sky days are then obtained by taking days with an average cloud cover of less than 5% (allowing a small cloud to pass by). The amount of days that are in these cloud regimes are summarized in Table 2.1.

Days with convective clouds are then characterised by having cloud bases near the lifted condensation level. This poses two challenges: first, "what should we de-

Table 2.2: Number of days in each of the two convective cloud regimes in observations for different settings of the distance from cloud base to LCL (D) and the fraction of the amount of measured cloud bases between 10–16 UTC that must satisfy this condition. Cloud cover above 3 km does not exceed 5%.

Observations	CC 5 – 30%	CC 30 – 70%
$d = 100$ m, $f = 33\%$	143	167
$d = 150$ m, $f = 33\%$	165	253
$d = 200$ m, $f = 33\%$	171	136
$d = 200$ m, $f = 50\%$	157	189
$d = 200$ m, $f = 70\%$	122	96

fine as near LCL?"; and second, "how do we handle days that have mostly convective clouds, but also (shorter) periods of non-convective clouds?" We introduce two parameters: the distance from the LCL (d) and fraction (f) of cloud bases within d from LCL between 10 – 16 UTC (observations) or fraction of time (LES) between 10-16 UTC with the lowest peak cloud fraction is near LCL. The settings for d and f are different for observations and LES, because they have other cloud measurements, which will be further discussed in the specific sections. Lastly, we added a restriction on the average amount of cloud at higher altitudes during daytime ($< 5\%$), because the LES is not setup to produce deep convection.

Cloud bases, cloud cover and LCL in observations

In observations, cloud related properties such as cloud cover, and cloud fraction above a certain height are inferred from the cloud base height measurements that are provided by the LD40 every 15 seconds, if any cloud base is present. Temporal cloud cover is constructed by dividing the number of detected cloud bases in 10 minutes by the total number of measurements (40 in total). LCL is obtained by converting Bolton's formula for temperature at LCL Bolton (1980) to a height from each temperature, relative humidity and specific humidity measurement at the tower at 200 m altitude during 10:00 – 16:00 UTC Romps (2017). The settings for d and f are evaluated using visual inspection. If more than 1/3 of the detected cloud bases are near LCL, this day is flagged as a day with convective clouds. The 1/3 is subjectively chosen and evaluated, using visual inspection.

Comparing again with the manual classification, and judging from the ceilometer quicklooks, we removed all days with more than 5% of its measured cloud bases above 3 km, to ensure the shallow convective regimes predominantly include shallow clouds. The sensitivity to the different thresholds are presented in Table 2.2.

Cloud bases, cloud cover and LCL in LES

In LES, 10-minute averaged aerial cloud cover is calculated from the vertically integrated LWP. The cloud base height is taken as the first height at which the hourly and domain averaged cloud fraction profile maximizes. To avoid detecting small excur-

Table 2.3: Number of days in each of the two convective cloud regimes in LES for different settings of the distance from cloud base to LCL (D) and the fraction hours between 10–16 UTC that must satisfy this condition. Average cloud fraction above 3 km does not exceed 5%.

LES	CC 5 – 30%	CC 30 – 70%
$d = 100 \text{ m}, f = 4/7$	190	416
$d = 150 \text{ m}, f = 4/7$	231	449
$d = 200 \text{ m}, f = 4/7$	238	453
$d = 200 \text{ m}, f = 3/7$	273	462
$d = 200 \text{ m}, f = 5/7$	191	438

sions from zero as the local cloud fraction maximum, we set a minimum value of 1% cloud fraction. If no maximum exists (e.g. when the upper domain is saturated with cloud), we use the first height at which the cloud fraction exceeds 1%.

The main difference between the selection method in observations and LES is the criterion to check whether clouds are rooted. LES gives a cloud fraction averaged over the hour, whereas in observations we have data every 15 seconds. Therefore the hourly cloud fraction in LES is likely to have clouds every hour, leading us to look only at whether (some) cloud is present during the individual hours. The sensitivity to the thresholds of the distance to LCL and the fraction of hours at which cloud base is near LCL is presented in Table 2.3.

The LES is not sensitive to changing the allowed distance to LCL from 150 – 200 m, unlike observations, but it is sensitive to changing d from 100 to 150 m. Comparing again with the visually assessed days, we find that $f = 4/7$ and a limitation on cloud fraction above 3 km yield the best classification. For simplicity, we kept d to 200 m, as in the observations.

2.3.1 Validating the LES against observations

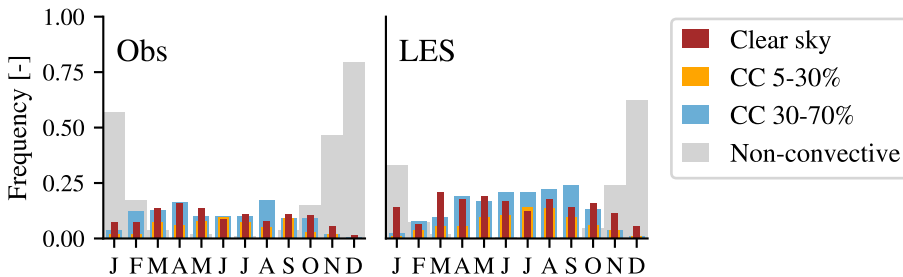


Figure 2.3: Distribution of the cloud regimes per month for years 2009–2017. Upper panel: Observations, lower panel: LES.

Intuitively, we expect more non-convective days in winter and more clear-sky or fair-weather cumulus days in the spring and summer months. This is reflected in the

Table 2.4: Confusion matrix comparing the cloud regime selection in observations and LES. Note that all convective days with clouds that do not have their base near LCL or too many cloud cover above 3 km are excluded from our analysis.

		LES					Total Obs.
		Clear sky	CC 5-30%	CC 30-70%	CC >70%	Non convective	
Observations	Clear sky	243	26	8	3	0	280
	CC 5-30%	18	80	47	2	0	147
	CC 30-70%	7	44	139	35	0	225
	CC >70%	0	2	39	125	16	182
	Non-convective	33	5	19	29	352	438
Total LES		301	157	252	194	368	1256

distribution of the cloud regimes over the different months, whose character is similar in observation and LES (Figure 2.3). The distribution of days falling into each cloud regime shows low cloud cover cumulus days become more numerous from spring to summer and decline again in autumn. The confusion matrix, which compares days classified in LES and observations for the entire climatology, reveals an overall good agreement in the relative distribution of days into the different cloud regimes (Table 2.4). We can see in the cumulus regimes that LES often produces too little or too much cloudiness, and the LES appears to favor the formation of convective clouds compared to the observations: more convective days are categorized from the LES at the expense of non-convective (cloud) regimes. We believe that the limited domain and a lack of variance in the large-scale forcing both play a role in constraining the LES' skill in reproducing cloud systems much larger and deeper than the domain size used, and that the cyclic boundary conditions and a lack of cloud radiative feedbacks may overemphasize convective structures. Coupling LES to large-scale flows in realistic ways remains an area of active research, whereby moving to large domains does not necessarily imply better comparisons with local observations Schemann et al. (2020).

In the remainder of our study, we compare statistics within the cloud regimes, which, as these tables indicate, do not necessarily include the exact same days. This is not a concern, because our objective is not to check whether the LES captures daily weather, but instead we are looking to expose the physics that accompany specific cloud regimes. As we will show next, the observations and the LES largely agree on the weather conditions that accompany the different cloud regimes.

2.4 Climatology of cloud regimes

Figure 2.4 shows histograms of observed mean temperature, relative humidity (RH), zonal and meridional wind speed (averaged over the lowest 200 m), and surface buoyancy flux during the daytime hours (10:00 – 16:00 UTC) for the four cloud

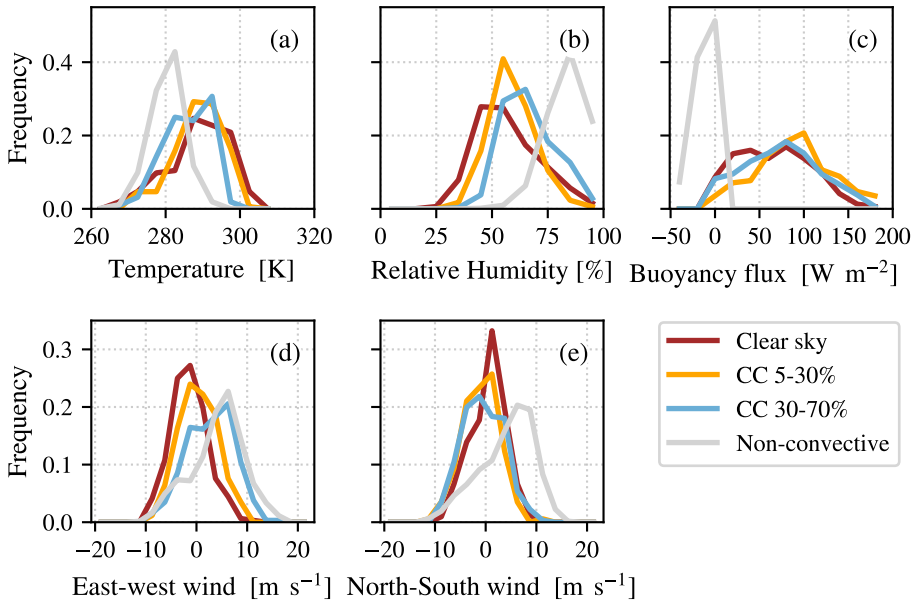


Figure 2.4: Distribution (histogram) of observed temperature, relative humidity, surface buoyancy flux, zonal wind u and meridional wind v for each cloud regime. Positive zonal winds indicate winds from the west and positive meridional winds indicate winds from the south. Except for the surface buoyancy flux, all variables are averaged over the lowest 200 m and between 10-16 h UTC.

regimes. Typical continental fair-weather in the convective regimes is associated with warm and relatively dry surface layers and positive buoyancy fluxes (by definition). This reflects that such regimes are most common in Spring and (early) Summer (Figure 2.3). The cloudier regimes occur on days with larger RH, which in the case of the non-convective regime is frequently in winter and likely associated with storm passages and (by definition) negative surface buoyancy fluxes. Cloudy days are generally days with westerly winds, which bring relatively moist air from the ocean on to land, whereas a relatively large portion of the clear sky days happen when winds are from the east. Convective clouds are not restricted to warm fair-weather. The Netherlands experiences regular occurrences of cumulus congestus and even deeper convection on days with cold air outbreaks (typically northwesterly winds) and after frontal passages (typically southwesterly winds). Some of which might be present in the CC 30-70% regime, although we believe most are filtered out in our cloud classification.

Figure 2.5 shows a similar climatology for the LES, but then in terms of averaged vertical profiles of cloud fraction, thermodynamics and the horizontal wind components extending up to heights of approximately 5 km. To maintain vertical structure, the height axis is scaled by the mixed-layer height (η), defined as the height of the minimum buoyancy flux and often coinciding with cloud base. The cloud fraction

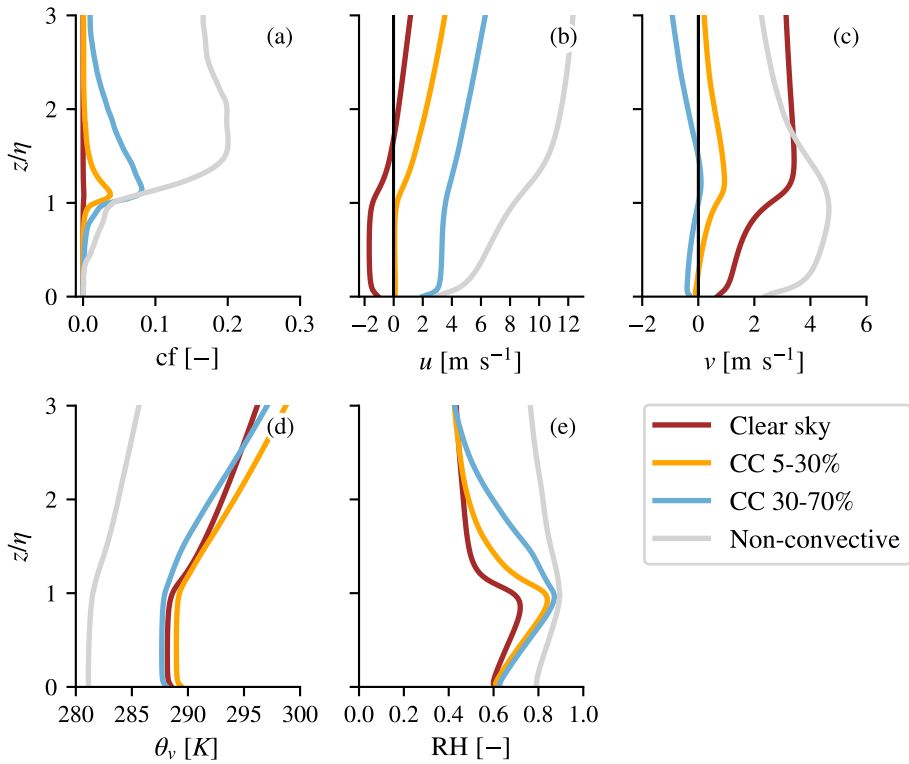


Figure 2.5: LES cloud regime averaged profiles of (a) the cloud fraction, (b) zonal wind speed (positive eastward) u , (c) meridional wind speed (positive northward) v , (d) θ_v and (e) relative humidity.

profiles confirm our classification, revealing the classical cumulus cloud fraction profile for the cumulus regimes (yellow and blue lines). The non-convective regime (*e.g.*, westerly storms, in grey) also contains days with fog and other stratus layers. Like the histograms (Figure 2.4) the clear sky and cumulus days are warm and relatively dry, with weaker westerlies or even easterly winds. The cumulus regime with a cloud cover between 5-30% shows a near zero u wind, which is an averaging artifact: as seen in Figure 2.4, it has a zero-centered distribution of east-west winds. Profiles of virtual temperature are well mixed in all cloud regimes. The mixed-layer height is clearly visible in the temperature, relative humidity as well as the wind speed profiles and often coincides with cloud base height.

From a careful observation of the wind profiles we can already notice that the zonal u wind is well mixed in the boundary layer in all regimes, except the non-convective regime. In turn, these have a larger wind turning throughout the boundary layer, reflected by larger wind shear (vertical gradients) in the meridional component. In the following, we will look more closely at wind shear in the surface layer and address whether there are notable differences in how winds are vertically mixed depending on the regime.

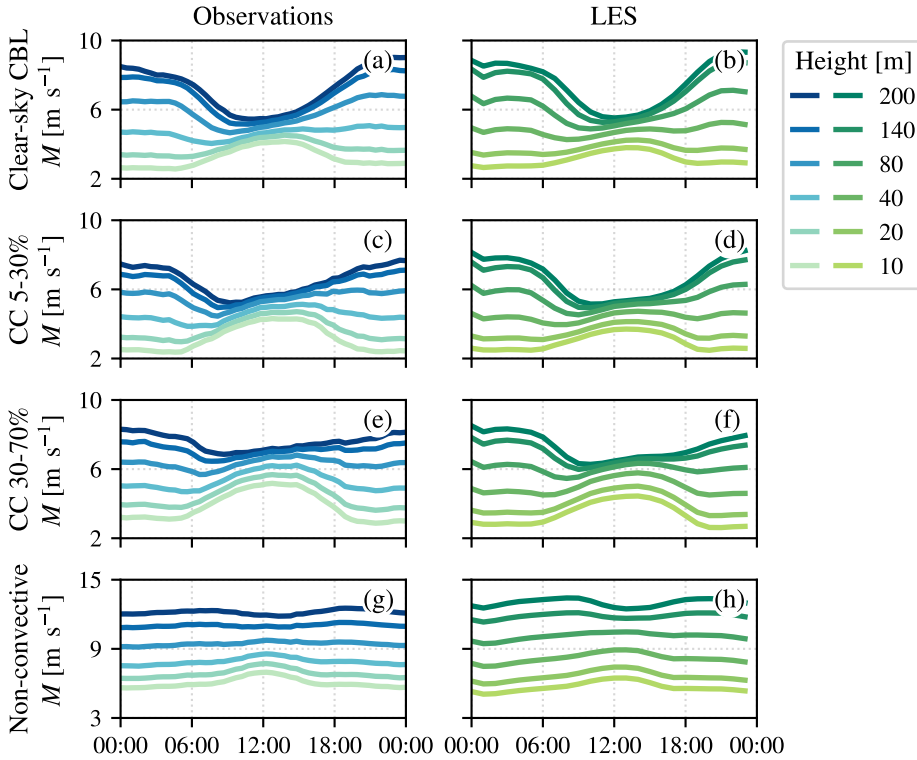


Figure 2.6: Average diurnal variations of wind speed (M) at five levels of the measurement tower at Cabauw under different cloud regimes. Observations (left column) and LES (right column) between 2009 and 2017 (incl.) are shown.

2.5 Wind gradients in the surface layer

To address surface layer wind gradients and the degree of wind mixing in the morning and afternoon we adopt the analysis of He et al. (2013) and plot wind speeds at different heights as a diurnal cycle. We do this for both the observations and the LES (Figure 2.6). Because the observation heights are not the same as the LES grid heights, we interpolated the LES wind linearly to the observation heights. The general characteristic of the wind diurnal cycle is a larger wind gradient (wind shear) during the night and a smaller wind shear during the day. During the night, the boundary layer becomes shallower and stratified, and turbulent mixing is reduced. At Cabauw, the boundary layer height sometimes becomes smaller than the tower enabling us to detect nocturnal low level jets (LLJ). LLJs are measured 20% of the nights, usually between 140 – 260 m above the surface and with wind speeds from 6 – 10 m s^{-1} Baas et al. (2009). The development of the wind during the day is in each regime well-captured by LES (Figure 2.6). The main difference with the observations is in the wind speed. At night the LES has faster winds between 80 – 200 m, whereas

during the daytime, observations usually show a stronger mean wind at 10 m. The wind bias at nighttime is a known issue in IFS, and a weak bias is also found in ERA5 through which the LES may inherit this wind bias. This should not affect the ability of the LES to reproduce the turbulence that underlines the convective influences we are studying here.

During daytime, wind shear is reduced in all regimes, especially between 80 and 200 m. The smallest wind shear (strongest mixing) is observed on shallow convective days, followed by clear-sky days. Based on the study by He et al. (2013), we expect better mixing on days with larger surface buoyancy flux, which is the case. The cumulus and clear-sky days have the largest surface buoyancy fluxes (Figure 2.4c). The more cloudy non-convective regime, with negative surface buoyancy fluxes, has larger vertical shear and mixing is almost absent.

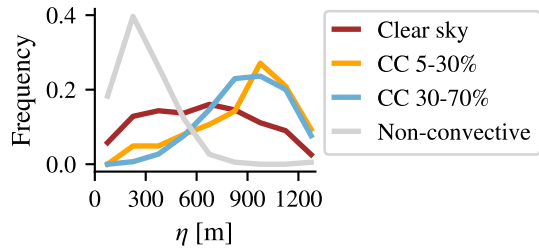


Figure 2.7: Distribution of the mixed layer top (η) within each cloud regime between 10-16h UTC, from LES.

At all heights levels, wind speed in the surface layer increases during daytime in the clear-sky and cumulus regimes. This may be caused by the deepening of the boundary layer, leading to entrainment of higher momentum air from the free atmosphere into the boundary layer. Indeed, the cumulus regimes are associated with deeper mixed layers, whose tops are identified as the minimum of the surface buoyancy flux (Figure 2.7). Increases in wind speeds may also be connected to sea breeze effects which have been observed in $\sim 8.3\%$ of the days from May to August (Arrillaga et al., 2018).

Figure 2.8a and b show that the total momentum flux at 60 m increases during daytime and peaks slightly after noon, when the buoyancy flux is large (panel c and d). At 12:00 UTC, when the wind shear is smallest in the cumulus regimes, the total momentum flux is slightly larger in the shallow convective regimes, than in the clear-sky regime. Likely because these regimes have larger near-surface wind speeds at daytime (Figure 2.6). The 3 m momentum flux observations are different than the measurements at 60, 100, and 180 m. Because of the much smaller footprint at 3 m, it only experiences roughness from the low-grass meadows in Cabauw, whereas the measurements at higher altitude are influenced by rougher surfaces further away. Therefore we chose to show the more representative 60 m measurements.

The total momentum flux in the non-convective cloud regime differs substantially between LES and observations, which cannot be explained by wind speed differences (they are comparable) and for now are not yet understood.

Evidently, the different climatology (weather regimes) associated with the different cloud regimes plays an important role in the degree of wind mixing in the

surface layer *e.g.* fair weather cumulus days form on days with larger buoyancy fluxes, weaker stability and weaker large-scale winds. Therefore, wind shear is by definition already smaller. In the following section, we account for the differences in stability and large-scale wind to identify which differences in wind shear across cloud regime remain.

2.5.1 Non-dimensional wind gradients following Monin-Obukhov Similarity Theory

Differences in wind speed and buoyancy flux are observed between the clear-sky and shallow convective days. Stronger winds and weak buoyancy flux may introduce a very different mixing structure and momentum transport than on days with weaker winds and stronger buoyancy flux Moeng and Sullivan (1994). The effect of the surface buoyancy flux and the large-scale wind is illustrated in Figure 2.9. The wind speed at the surface must go to zero, and therefore, the wind shear is largely determined by the 200 m wind. In Figure 2.9 we normalise the wind by the daily average wind speed at 200 m and show the composite diurnal cycle for days in three different surface buoyancy flux categories (on the y-axis) and three different 200 m wind categories, where we take the 200 m wind as a measure of the strength of the large-scale wind. The stronger the wind (towards the right in each row), the larger the shear. An increase in the surface buoyancy flux also leads to better mixed winds

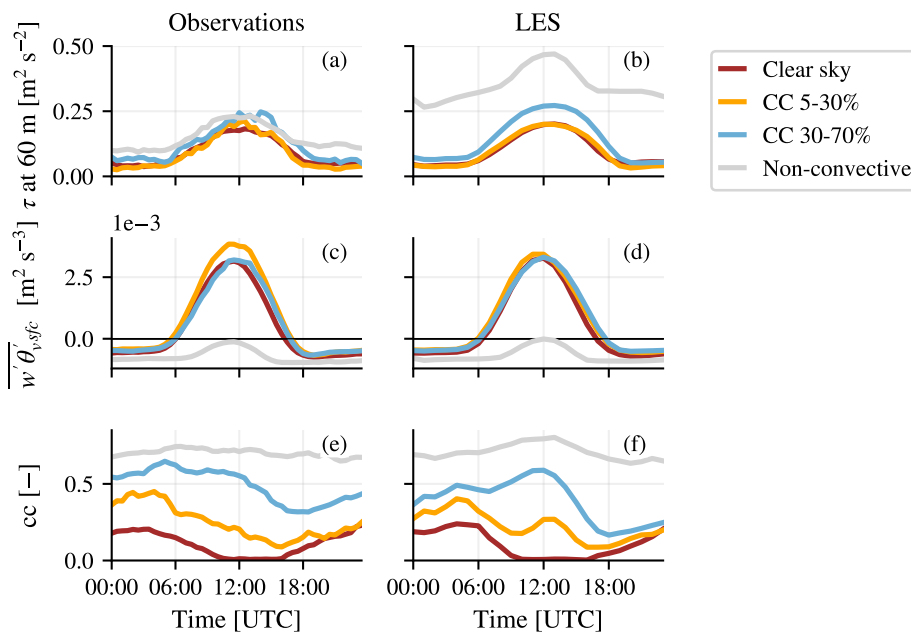


Figure 2.8: Average diurnal cycle of the total momentum flux (τ) at 60 m for each cloud regime in a) observations and b) LES.

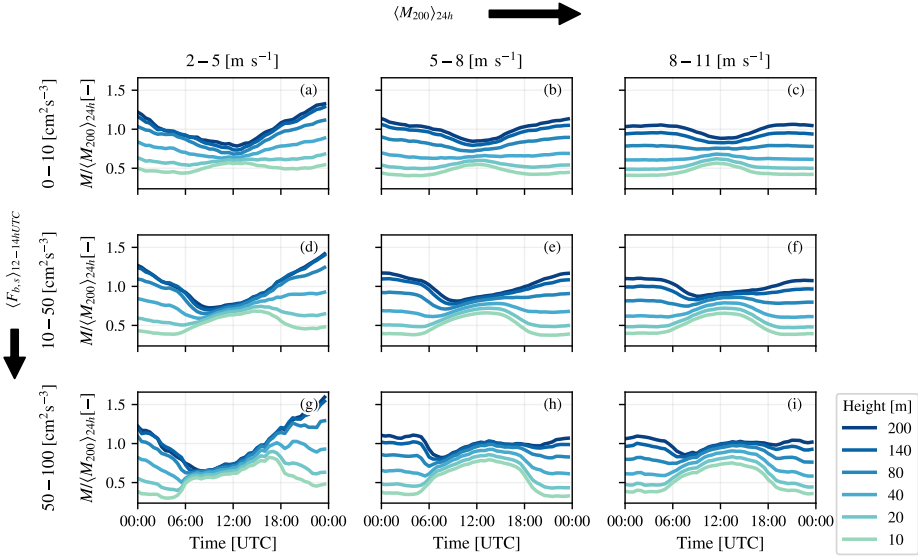


Figure 2.9: Diurnal cycle of wind speed as observed at the Cabauw tower when the data is separated on 12-14h UTC average surface buoyancy flux and daily average wind speed at 200m.

at first, but increasing it beyond $50 \text{ cm}^2\text{s}^{-3}$ does not make a major difference, other than making the winds more variable and causing a stronger increase in wind speed during the afternoon.

To account for the covariability between wind and stability with convection, we use the Obukhov length. The Obukhov length (L), given by:

$$L = -\frac{\overline{\theta_v}}{kg} \frac{u_*^3}{(w'\theta'_v)_s}, \quad (2.1)$$

in which θ_v stands for the virtual potential temperature near the surface, u_* for the friction velocity at the surface, k for the von Kármán constant, g for the gravitational acceleration, and $(w'\theta'_v)_s$ is the surface flux of θ_v , which we often refer to as surface buoyancy flux. The friction velocity u_* , defined as $u_* = (\overline{u'w'_{sfc}}^2 + \overline{v'w'_{sfc}}^2)^{1/4}$, denotes the turbulent momentum flux at the surface and is thus a measure of momentum destruction in the surface layer. Convective and stable conditions are distinguished by the sign of the buoyancy flux: a negative Obukhov length corresponds to a positive surface buoyancy flux and a more unstable atmosphere. Furthermore, a large negative Obukhov length implies either a small buoyancy flux and / or a large friction velocity, and thus more neutral conditions. Vice versa, a small negative Obukhov length indicates more unstable conditions.

If we contrast the different cloud regimes at a given Obukhov length, we may identify whether other processes than stability play a role in setting the surface layer wind shear. Figure 2.10 shows two parameters as function of classes of stability

$(-1/L)$, which are all averaged between 12:00 – 14:00 UTC, where wind speeds in the diurnal cycle were best mixed. We only look at an unstable atmosphere ($-1/L > 0$, with weakly unstable (more neutral) conditions on the left and more unstable conditions on the right). Panel a and b show the ratio of the 80 m and 200 m wind, as a measure of the wind shear: the closer the ratio to 1, the smaller the shear. Panel c and d show the universal similarity function $\phi_M(z/L)$, commonly known from Monin-Obukhov Similarity Theory (MOST), which is defined as:

$$\phi_M = \frac{\kappa z}{u_*} \frac{\partial u}{\partial z}. \quad (2.2)$$

We approximate ϕ_M from the 12:00 - 14:00 UTC averaged winds and estimate $\frac{\partial u}{\partial z}$ from M_{80} and M_{200} . ϕ_M is another way of looking at wind mixing, but it also allows to remove a hidden dependency on u_* . The general behavior of ϕ_M is to decrease from neutral to unstable conditions as L is reduced (towards the right).

In the observations (left panels), across all stability classes, the regimes with convective clouds with cloud covers 5-30 and 30-70% (yellow and light blue) have a relatively larger M_{80} to M_{200} ratio than the clear-sky regime (red). This also shows in the ϕ_M curves. The regimes have separate curves, whereby the convective cloud regimes (yellow and light blue) exhibit smaller ϕ_M values than clear skies. In other words, at a given wind gradient these regimes have larger frictional velocity (larger momentum fluxes) near the surface. This suggests that deeper or stronger convective circulations sustain larger 80 m wind speeds compared to a situation where only shear-driven turbulent stresses are present. The vertical bars indicate the standard error and reveal that variability is larger in more unstable classes. These classes also include less samples (days), but it may also reflect that convective scales do not make a large difference when the atmosphere is already unstable.

The LES (right panels) confirms this picture, although there are notable differences. For instance, values for ϕ_M are overall smaller in LES than for the observations, which is probably because the observed and simulated roughness lengths are different. Cabauw is known to have a complicated land surface, with grassland and small roughness lengths felt close to the surface, and trees and a larger roughness length felt at greater heights.

In general, the LES reproduces the different character of the momentum mixing under clear skies and (shallow) convective days, and therefore, we can examine additional statistics from the LES. As we saw earlier in Figure 2.7, the convective cloud regimes are associated with deeper mixed layers. Next, we will explore wind profiles and momentum flux profiles for the different regimes across the entire boundary layer and not just near the surface.

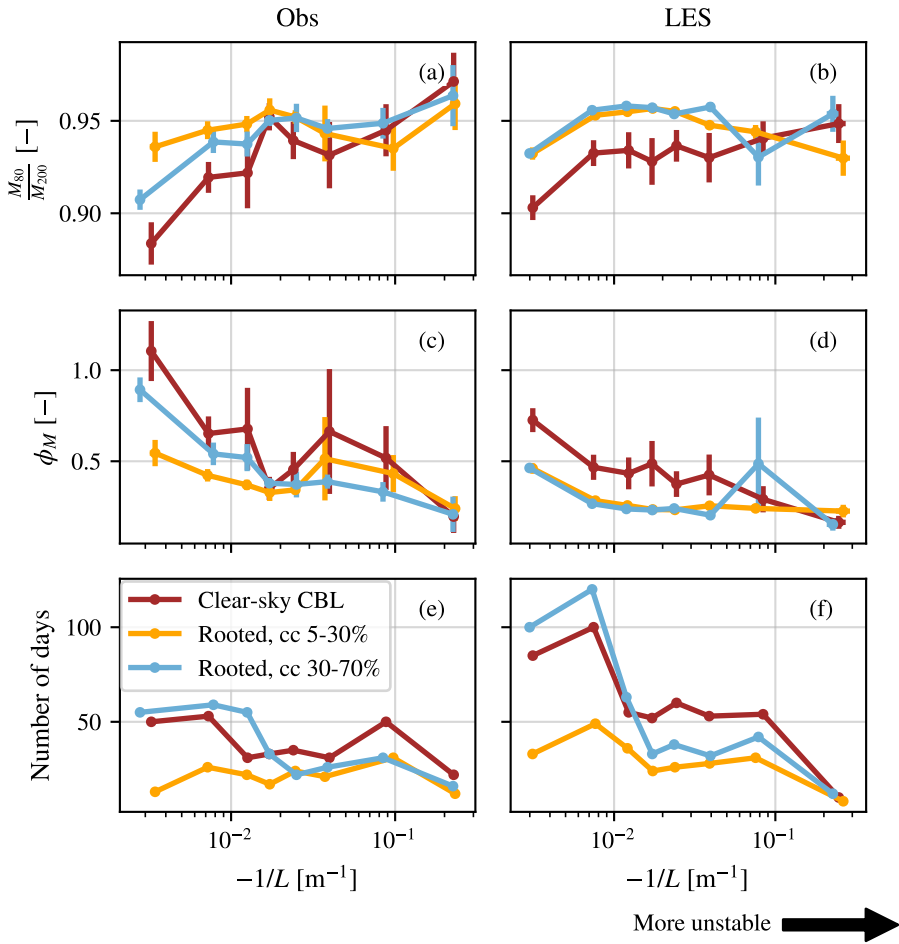


Figure 2.10: Observations (left) and LES (Right): a,b) Ratio between the wind speed at 80 and 200 m, c,d) universal similarity functions, and d,e) the number of days within each $-1/L$ bin for the five cloudiness categories. Error bars in panel a – d) indicate the standard error of the mean. All data is averaged over the hours 12-14 UTC, when the winds are best mixed.

2.5.2 Wind and momentum flux profiles

Can we identify differences in momentum transport between cloud regimes? This is where the LES output is particularly valuable, because it provides momentum fluxes at height levels extending beyond the tower height. Not only the wind speed, but also the wind direction varies at Cabauw. For instance, there are regular episodes with easterly winds and westerly winds in the clear sky regime, see Figure 2.4. Changes in wind directions are associated with a change in sign of the momentum flux, which upon averaging, can bias the momentum flux towards small or zero values. We therefore transform the winds to a natural coordinate system whereby the positive (stream-wise) s -axis is aligned with the direction of the hourly mean of the wind at 65 m height (which is well within the surface layer), while the (normal) n -axis is defined perpendicular and anti-clockwise from the positive s -axis. From the along-wind and cross-wind components at each height we calculate the momentum fluxes, which are then normalised by the friction velocity squared and plotted against the non-dimensional height axis z/η . The mean along-wind and cross-wind profiles for each regime are shown in Figure 2.11 a and b. In essence the cross-wind component tells us how the wind is turning with height in the boundary layer with the wind at the lowest 10% of the mixed layer as a reference. A negative cross-wind implies a (clockwise) veering of the wind with height. The average flux corresponding to a veering or backing cross wind, is similar of shape but has a different sign (panel e). In the cumulus regimes, the magnitude of the flux differs between backing and veering winds: the slower backing winds have smaller (normalised) fluxes for the low cloud cover convective regime, whereas for the higher cloud cover convective regime the behavior is reversed. The general tendency is similar for all cases: in the lower mixed-layer the wind is slowed down, whereas in the upper part the cross wind is typically sped up. As in Figure 2.5 d and e, days that are not convectively driven tend to have strong westerly winds (e.g., storm passages) and larger wind shear across the mixed-layer. The cross-wind component for $z/\eta < 1$ is small in all regimes, implying a well-mixed sub-cloud layer. Substantial wind turning is pronounced near the mixed-layer height (or cloud base).

The other panels in Figure 2.11 show the skewness of the vertical velocity (c) and the non-dimensional along- and cross-wind fluxes (d, e), as well as the total momentum flux τ (f). Note that the average of the total momentum flux τ is unequal to the sum of the average along- and cross-wind fluxes as we first calculate τ , normalise it, and then average over each cloud regime. The momentum fluxes clearly reveal how turbulent mixing extends beyond $z/\eta = 1$ for the cloudier categories (light blue to grey). For instance, the normalised total momentum flux τ decreases with height approximately linearly (Figure 2.11 f), but is still at least 30% that of its surface value at $z/\eta = 1$ for the often overcast non-convective regime in grey, as well as the high CC cumulus regime in light blue.

The clear-sky and cumulus regimes have a normalized total momentum flux at $z/\eta = 0.5$ that is close to 1 (Figure 2.11 f). The relatively large flux is primarily generated in the cross-wind component (Figure 2.11 e). The strong wind turning or wind jump at the top of the mixed layer can play a role at producing larger shear-

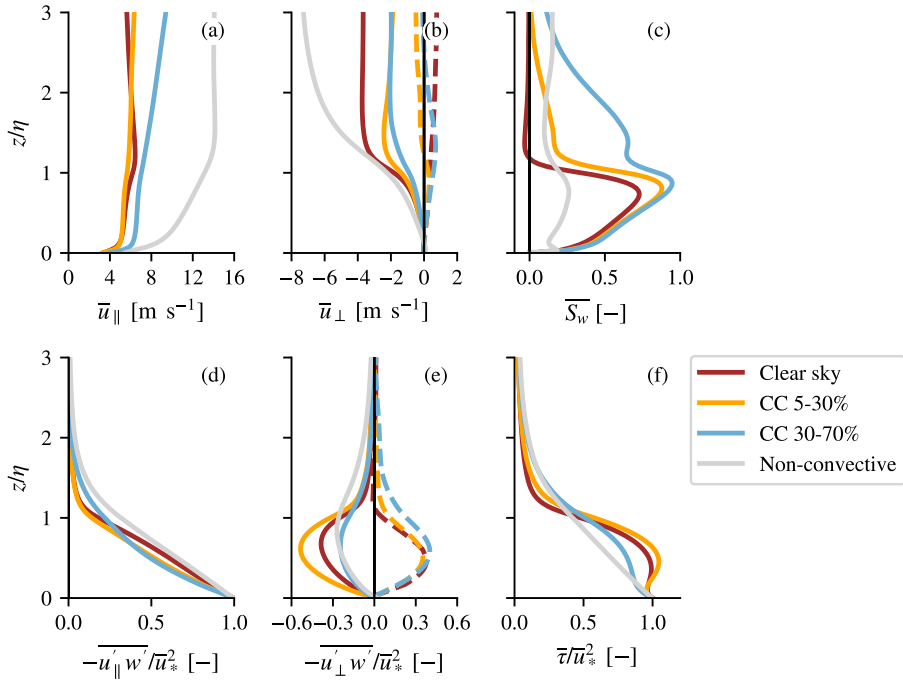


Figure 2.11: Cloud regime averaged LES profiles of the (a) mean wind, (b) cross wind (c) skewness of vertical wind, momentum fluxes in (d) parallel and (e) cross wind direction , and (f) total flux for the five cloud regimes. Dashed lines in panel (b) and (e) indicate the backing wind cases. All variables are normalised by the mixed-layer height, fluxes are also normalised using the surface friction velocity.

driven stresses. Additionally, (convective) eddies can contribute to flux at these levels. These regimes (in blue and yellow) have the largest vertical velocity skewness in the sub-cloud layer (Figure 2.11 c), indicating stronger updrafts and more coherent plumes may be more effective at transporting slow momentum from the surface towards the mixed-layer top. This is in correspondence with the observational study by Lareau et al. (2018) who found that medium cloud cover cumulus (30-50%) have largest skewness.

In the along-wind component of the momentum flux (2.11 d), profiles are more similar, but there is less flux below $z/\eta = 0.7$ in the cumulus regimes (yellow/blue). Perhaps, because the wind profiles are already better mixed in these regimes (Figure 2.11 a), there is less momentum flux generated within the mixed-layer.

The momentum tendency is determined by the negative flux divergence as:

$$\partial_t u_{\parallel}(z) \propto -\partial_z \overline{u'_{\parallel} w'}(z), \quad (2.3)$$

where $\partial_t = \frac{\partial}{\partial t}$, and similarly for ∂_z . A decrease of the flux with height implies that $\partial_t u_{\parallel} < 0$: the wind speed in the direction of the mean flow reduces. In the

parallel wind direction, we find strongest shear near $z/\eta = 1$ where the flux changes rapidly with height in clear-sky and cumulus (5-30%) days.

2.6 Conclusion & discussion

This study aims to answer: "Do the surface-layer wind shear and momentum flux profiles change in different cloud regimes?" In particular, we are motivated by the idea that convective clouds are associated with different momentum transport and winds in the layers below. To explore such statistical relationships, we used a long time record of observations and daily LES hindcasts, which allow us to group different cloud regimes together across a wide range of atmospheric states.

We designed an automated classification that flags a day as belonging to a convective cloud regime based on several criteria, including having a positive surface buoyancy flux during daytime, having a cloud base close to the theoretical LCL, and no cloud above 3 km. We contrasted these convective days - with two classes of cloud cover - to clear sky days and days not driven by convection that often have other types of clouds, such as mid or high-level cloud not rooted in the surface or mixed layer. In the LES, we removed all days where convection or the large scale forcing saturated the upper layer of the model domain, leading to less days falling into that category especially. It is these days with deeper and larger cloud regimes, for which the LES was not traditionally designed and for which the domain size is too limited.

Overall, we have confidence in the LES' skill to reproduce the type of clouds expected for certain weather regimes, and also the turbulence characteristics associated with clear-sky and shallow convective regimes. The wind, temperature and humidity climatology and mean diurnal cycle of winds belonging to the different cloud regimes are very similar in LES and observations, even if the days within the classifications do not always match.

We find that clear sky days and shallow convective cloud days have a very similar diurnal cycle of the surface layer wind, with a large wind gradient during nighttime that is mixed away during daytime. Shallow cumulus days generally have weaker winds and larger buoyancy fluxes than clear-sky days, and therefore have a head start in mixing away the nighttime wind shear. They also produce a steady increase in mean surface layer winds during the afternoon associated with the development of a deeper boundary layer and presumably the entrainment of higher momentum air.

However, we must keep in mind that shallow cumulus days tend to be warmer days from late spring to early autumn. Hence, because of the larger insolation in these months, the average buoyancy flux is larger than that of the clear-sky regime that is better distributed over the year.

The factors that help form convective clouds in the first place such as large surface buoyancy fluxes also help reduce surface layer wind shear. By further grouping the data into different stability classes defined by the Obukhov length, we attempt to remove the influence of surface buoyancy fluxes and surface friction velocity (set by

the large scale wind) on the wind gradients. Doing so shows that convective cloud regimes have smaller surface-layer wind gradients compared to clear sky days at a similar neutral or weakly unstable stability. We also find that the Monin-Obukhov non-dimensional wind gradient function ϕ_M , which relates the surface friction velocity to the surface layer wind gradient, is smaller for the convective cloud regimes. This would imply that for a similar wind gradient (large scale wind), more momentum flux is generated on those convective cloud days compared to clear sky days. It also suggests, as shown by Brown and Grant (1997); Liu et al. (2019a); Fodor et al. (2019), that empirical Monin-Obukhov similarity functions do not explicitly include the effect of large scale up- and downdrafts associated with convective eddies (using the scaling of boundary layer depth) underestimate the momentum flux that is generated in the surface layer.

The non-dimensional momentum flux profiles throughout the entire boundary layer in the direction of the mean near-surface wind are very similar for the different regimes at midday, which suggests that small-scale shear-driven momentum diffusion still dominates the momentum flux. Larger differences are found in the non-dimensional cross-wind momentum fluxes, where the clear-sky and shallow convective clouds regimes have much more momentum flux in the mixed layer. These regimes also have stronger updrafts. Compared to clear sky days and shallow cumulus days, the non-convective (cloud) regime has much more cross-wind momentum transport extending beyond the mixed layer top: up to 30% of the surface momentum flux is still present in the cloud layer ($z/z_i = 1.3$).

A fair question to ask is whether the clouds themselves, by triggering larger or more effective momentum transport, lead to weaker surface wind shear, and thus whether these results could be generalized to other locations over land. We cannot fully answer this question without a detailed budget study that samples the momentum tendencies introduced by convective and cloudy plumes and by small-scale turbulence in LES, or by spectral analysis of the scales that contribute to the total momentum flux in observations and LES. However, we may point to a few recent studies that reveal the influence of convective momentum transport on near-surface winds.

A recent study using Atlantic-wide ICON-LES hindcasts reveal that dry convective plumes coupled to moist convection overhead carry significant flux that tend to accelerate near-surface winds Helfer et al. (2021). A spectral decomposition of momentum fluxes by eddy sizes derived from LES of organized shallow convection in a cold air outbreak demonstrates that larger eddies are accompanied by a momentum flux profile that can maximize in the mixed layer and accelerate near-surface winds Saggiorato et al. (2020).

Whether our results of Cabauw can be generalized depends on whether specific mechanisms are at play over the Netherlands, which drive both weaker surface layer wind shear and more shallow cumulus convection. A land-sea breeze effect could be at play, driving stronger onshore winds at daytime and moister air masses that favor cumulus convection regardless of locally driven buoyancy fluxes. We suspect that mesoscales and regional scales can make a difference in the real world, but

not adequately captured in 10 min averages eddy-covariance flux data or small LES domains with cyclic boundary conditions Dixit et al. (2021).

A number of efforts are underway that will address these challenges. Foremost, the Ruisdael Observatory (<https://ruisdael-observatory.nl/>) will realize near-real time DALES hindcasts with open boundaries at 100 m resolution over the entire Netherlands combined with a dense measurement network that includes scanning cloud radars and a wind lidar at Cabauw that are currently being analyzed.

3

Momentum fluxes from airborne wind measurements in three cumulus cases over land

3.1 Introduction

Observations of the vertical profile of wind are valuable for reducing forecast errors and for advancing the understanding of processes that influence wind variability, including large-scale and mesoscale dynamics and small-scale turbulent processes. In this paper we combine state-of-the-art airborne Doppler wind lidar (DWL) combined with traditional in situ turbulence measurements to measure the profile of wind and turbulent wind fluctuations within cloud-topped boundary layers, in which thermally-driven (convective) plumes are thought to play an important role in transporting wind. By measuring wind profiles at levels beyond meteorological towers and ground-based operational DWLs, we aim to investigate wind and momentum flux variability beyond the surface layer.

On local and regional scales, the growing wind energy industry has boosted wind profiling observations in the lowest layers of the atmosphere through the deployment of Doppler wind lidars (DWLs). DWLs conventionally measure high-resolution wind to the top of the wind turbine or to hub height (the centre of the wind turbine's rotor, up to 250 m). Such measurements are used to understand turbulent wind fluctuations in the surface layer that are influenced by weather, terrain, turbine wake

This research has been published as: Koning, A. M., Nuijens, L., & Mallaun, C. (2022). Momentum fluxes from airborne wind measurements in three cumulus cases over land. *Atmospheric Chemistry and Physics Discussions*, 1-22. <https://doi.org/10.5194/acp-2022-59>, and could not have been done without the contributions of Witschas, B., Reitebuch, O., and Lemmerz, C.

effects or shear across the rotor-swept area (Bakhshi and Sandborn, 2020; Banta et al., 2013; Iungo and Portè-Agel, 2013; Krishnamurthy et al., 2013; Mann et al., 2010).

One source of wind in the surface layer is the (downward) mixing of momentum from higher levels. Not only dry convection, but also moist convection plays an important role in this process, because clouds extend the boundary layer height, tapping in regions aloft with faster moving winds. This transport of momentum (momentum fluxes) by convective eddies (thermals) and through clouds is broadly called convective momentum transport (CMT). Like small-scale turbulence, CMT is an unresolved process in forecast models that contributes to uncertainties in local wind predictions. However, unlike the turbulent wind fluctuations measured in the surface layer through most commercial DWLs, few high-resolution wind profiles extend beyond the surface layer (> 200 m) to target wind fluctuations and momentum transport at heights where moist convection develops.

Our understanding of turbulent wind fluctuations throughout the boundary layer largely stem from a handful of in situ turbulence measurements during research aircraft flights at selected height levels in subtropical settings. A seminal study is that by LeMone and Pennell (1976), where flight tracks below and through cumulus fields near Puerto Rico were used to derive wind and flux profiles. This work highlighted that the momentum flux profile can take a very different shape depending on clouds overhead. In particular, they found that in fields of cumulus clouds organized in rolls, the rolls were responsible for a significant amount of the momentum transport even though clouds were extremely shallow. In fields of more significant and randomly distributed clouds, the linear flux dependence disappeared, becoming counter-gradient at various altitudes. However, some doubt remained as to whether the wind profile could have evolved during the flight, because the profile itself was only sampled by the turbulence measurements at selected legs.

Large-eddy simulations (LES) have revealed the very different nature that momentum flux profiles can take depending on the scales and domains considered (Zhu, 2015; Schlemmer et al., 2017; Saggiorato et al., 2020). LES output suggests that turbulent fluctuations on scales larger than 400 m explain a considerable part of the momentum flux, in particular above the surface layer towards the mixed-layer top and within the cloud layer. Recently, Dixit et al. (2021) suggest that the absence of mesoscale circulations in idealised periodic-boundary LESs lead to an underestimation of momentum flux that tends to be counter-gradient in the cumulus layer. So far, we lack understanding about the contribution of mesoscale horizontal flows to the momentum flux and its net effect on the wind. However, both observations and simulations clearly show the spatial variability in wind that is large in areas of convection, especially in the presence of precipitation whose evaporation can lead to cold pools and associated gust fronts (Zuidema et al., 2012; Li et al., 2014; Helfer and Nuijens, 2021).

Three prototype flights were carried out focusing on measuring the wind environment in convective situations to evaluate turbulent to mesoscale (up to 7 km) wind fluctuations and implications for the momentum flux profile. The campaign involved

dual-aeroplane flights over Germany using the Falcon and Cessna research aircrafts from the German Aerospace Center (Deutsches Luft- und Raumfahrt e.V., DLR) in Oberpfaffenhofen. The Falcon flew at high altitudes deploying a downward-looking scanning 2-micron Doppler wind lidar (DWL), used here, as well as the 20 degrees off-nadir looking ALADIN airborne demonstrator (A2D) lidar - the airborne prototype to the space-borne Aeolus instrument ALADIN. A comparison of the A2D, DWL and Aeolus measurements can be found in Witschas et al. (2020) and Lux et al. (2020). The smaller Cessna aeroplane flew below the Falcon at lower altitudes in the boundary layer collecting in situ wind and turbulence measurements. The three collocated flights captured conditions ranging from fair-weather shallow cumulus developing over hilly terrains to pre- and post-frontal convection with popcorn convection over flat terrains. Land use below the flight track was often agricultural with grass or low crops with very few bare lands. Few patches of trees were encountered, especially during the flight on 24 May 2019, as well as few villages.

The amount of statistics collected with just three flights is limited, but demonstrate the value of wind profiling by the DWL by showing on the one hand how robust the wind profile is as derived by the in-situ measurements, and on the other hand by revealing variability in winds carried at different scales. The questions we address in this manuscript are as follows:

- How do the DWL wind profiles match with in situ wind measurements?
- Are the measured momentum flux profiles in the sub-cloud layer and in the cloud layer in line with our expectation and can they be explained by convective updrafts?
- Which scales contribute significantly to wind variance and momentum flux?

The manuscript includes a description of the flight strategy, measurement techniques in section 3.2, which also includes a short explanation of down-gradient turbulent momentum transport and the updraft detection method. Section 3.3 describes the meteorological conditions during the three flights. Section 3.4 explores the different momentum fluxes in relation to the wind profiles and convection, including an analysis of the contributions of updrafts and scales that carry most of the momentum. Our findings are summarized in section 3.4.3.

3.2 Flight measurements and data processing

3.2.1 Flight strategy and measurements

The CloudBrake measurement campaign took place in Germany at the end of May and beginning of June 2019, a period that is known to often display (shallow) cumulus clouds. Starting from around noon until 13:30 or 14:30 local time (CEST), the flights targeted a time of the day during which cumulus clouds are typically well developed. An impression of the cumulus and weather conditions during each flights

is given in Figure 3.1. The first flight on May 24 (2019) was a typical shallow cumulus day: starting out with clear skies and weak winds, local shallow cumulus started forming over the hilly parts of the Swabian Jura. Clouds remained shallow, reaching a thickness of approximately 500 m. The second flight was under the influence of an approaching cold front, providing an interesting and dynamic mixture of shallow cumulus- and stratocumulus-topped boundary layers. Above the shallow cumulus that were around 1 km thick, mid-level alto-cumulus and stratus layers were present. The third flight, on June 4th 2019, experienced post cold front conditions. There was a large cumulus field with very diverse cloud tops. Clouds were at most 800 m thick and were typically thicker at the northern part of the leg.

During the 2–2.5-hour-flights, the two aeroplanes flew back and forth across the same pre-defined tracks. Because the two planes have different cruising speeds (the Cessna about 70 m s^{-1} , for the Falcon about 200 m s^{-1}), the pre-defined tracks ensure overlap in space and time to the degree possible. Flight legs were mostly flown cross wind and ranged from 50 to 100 km in length to ensure sufficient low-frequency wind variability. During some of the flights the tracks were moved or shortened with respect to the original plan to ensure cumulus clouds were captured. All flown tracks are shown in Figure 3.1. The terrain below was mostly used for agriculture with low crops, occasionally encountering patches of trees or villages. On the first two flights a hilly topography was present, whereas the last flight was above flat land.

Turbulence measurements using an in situ (3D) turbulence probe aboard the DLR Cessna Grand Caravan were taken at 100 Hz along the track at four different altitudes: within the mixed-layer, near cloud base, within the cloud layer and through the tops of only the thickest clouds. Employing the downward staring Doppler wind LiDAR at a measurement rate of 40 s, the DLR Falcon remained around 7.5 km altitude throughout the flight. The instruments are described next.

In situ turbulence probe

The DLR Cessna Grand Caravan was equipped with (i) a meteorological sensor package (METPOD) that measures temperature, humidity, pressure, and wind, and (ii) the IGI systems' AEROcontrol system, which combines measurements of a Differential Global Positioning System (DGPS) with a high-accuracy inertial reference system (IRS). Calibration of the devices before the flight and applying corrections afterwards result in a horizontal wind measurement uncertainty of 0.3 m s^{-1} and 0.2 m s^{-1} for the vertical wind component. Further details on the instrument specifics, calibration, correction procedure, and uncertainties can be found in Mallaun et al. (2015).

The high-frequency 100 Hz wind measurements, taken with a boom-mounted Rosemount model 858 AJ air velocity probe, are used for flux calculations. The aircraft movements are corrected using IGI. A linear fit is subtracted from the data before flux calculations. All scales from 10^{-2} Hz are included in this calculation, unless stated otherwise.

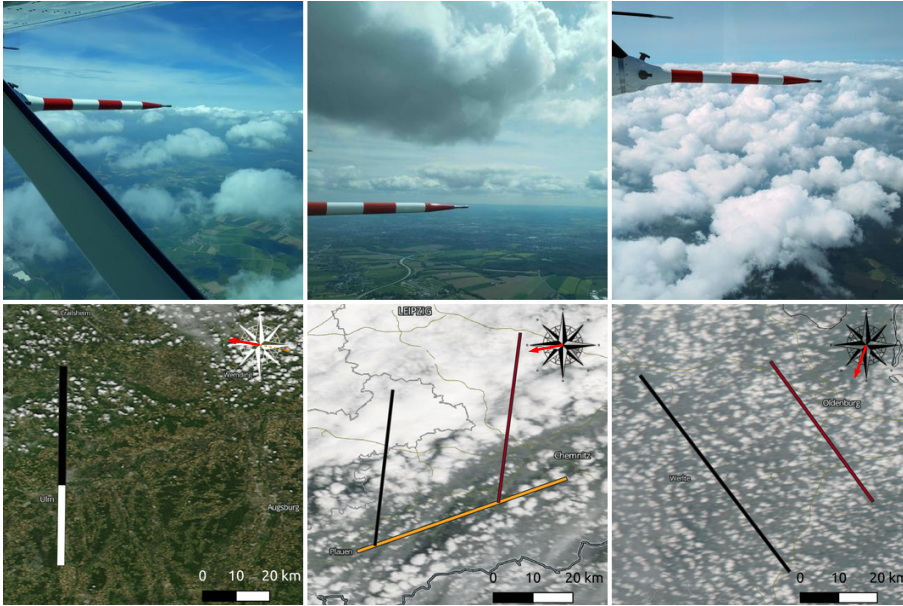


Figure 3.1: Photographs (upper row) and Modis satellite images from NASA Worldview Snapshots (lower row) of the cumulus fields during the flights on 2019-05-24 (left), where white is the cloud free area and black the cloudy area, 2019-05-27 (middle), where the west track is indicated in black, the east track in red and the southern track in yellow, and 2019-06-04 (right), where the west track is indicated in black and east in red. In each satellite picture, the horizontal black and white bar indicates a total distance of 20 km and the mean wind direction during the flight is drawn in the wind rose.

Energy spectra

To check the quality of the measurements, we calculated the power spectral density (based on the Fast Fourier Transform), after subtracting a linear trend from the data. Welch method was used with a Hann window with 1000 samples and 50% overlap to reduce noise in the spectrum. The spectra of the streamwise, cross and vertical wind components at four heights are displayed in Figure 3.2 for the western track on 4 June. Note that the streamwise and cross wind do not change much from zonal and meridional winds. The legs flown in the sub-cloud layer and in cloud layer contain more energy than the legs flown near cloud base and cloud top. Comparing the three wind components, turbulence appears to behave anisotropic: from 0.01-1 Hz, w contains similar (or in the sub-cloud layer more) energy than u and v . Between 1-10 Hz, the streamwise component has most energy, and w least. The characteristic $5/3$ slope of the inertial sub-range (dashed line) is seen from $\sim 0.2 - 15$ Hz (equivalent to a spatial resolution of 350 m down to 5 m, assuming a typical cruising speed of $65-75 \text{ m s}^{-1}$). From 15 Hz onward, the dampening of the fluctuations in the tube becomes visible and the signal falls off faster, except for one peak at 30 Hz, which is attributed to propeller effects (Mallaun et al., 2015). For calculations of the (eddy-covariance) fluxes and variances, we apply a high-pass filtering after linear detrending, removing

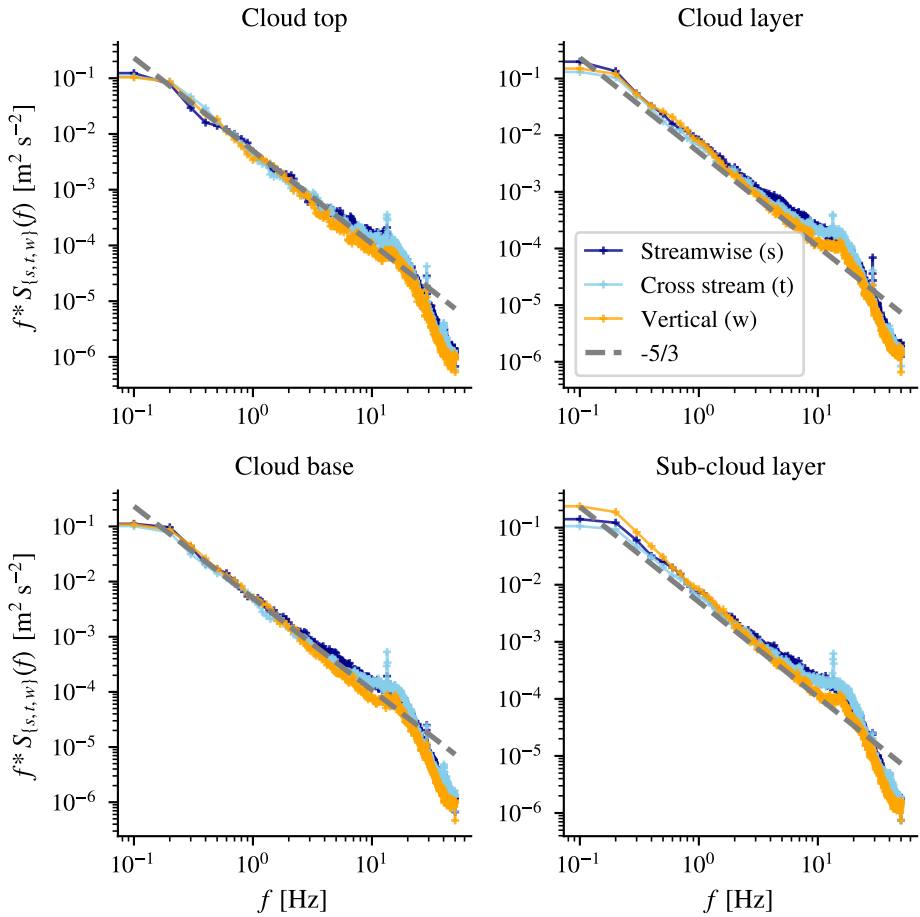


Figure 3.2: Power spectrum of the streamwise, orthogonal and vertical wind components for the western legs flown on 2019-06-04. Each altitude is shown in an individual panel. The dashed line represents the $-5/3$ slope corresponding to the inertial sub-range. Welch method with a Hann window of 1000 samples and 50% overlap has been applied to reduce noise.

the contributions by eddies with a horizontal length scale larger than 7 km (having a frequency lower than 0.01 Hz), a method that is also followed by Brilouet et al. (2021). Filtering out these frequencies will lead to an error because we lose information, however the random error that is generated by the finite sample size will be reduced (Lenschow et al., 1994).

Eddy-covariance fluxes

The time series are partitioned in leg-averaged values $\bar{\phi}$ and fluctuating parts ϕ' by subtracting a linear trend from the time series and applying a high-pass filter, a method that has also been applied by Brilouet et al. (2021). Doing so removes the

influence of larger scales having frequencies lower than the cut-off frequency and will lead to a loss of information (Lenschow et al., 1994). Fluxes and variances are then calculated by multiplying and averaging the fluctuations of w and ϕ over a specific time window, known as the eddy-covariance method. For instance, the leg average flux of ϕ is given by:

$$\overline{w'\phi'} = 1/N \sum_{i=1}^N w'_i \phi'_i \quad (3.1)$$

The smallest resolved frequency depends on the length of the leg, *i.e.* on the number of samples N : $f_{min} = f_s/N$, in which f_s is the sampling rate in Hz. Flying at a cruising speed of $\sim 65\text{-}75 \text{ m s}^{-1}$ at a constant height, and with constant ground speed, it is reasonable to assume that a static turbulent field is sampled. However, the statistical representation of the low frequencies is poor and therefore needs cautious interpretation.

Airborne Doppler wind LiDAR

Doppler wind LiDARs (DWLs) are the international standard for wind measurements and have been used for among other things 1) data assimilation experiments (Horanyi et al., 2015; Pu et al., 2017; George et al., 2021, e.g.), 2) to study for instance turbulence, gravity waves, orographic effects (Yuan et al., 2020; Gisinger et al., 2020; Baidar et al., 2020; Witschas et al., 2020, e.g.), and 3) to monitor the flow in wind farms (Kasler et al., 2010; Wagner et al., 2017; Zhan et al., 2020; Schneemann et al., 2021, e.g.). The coherent detection DWL employed in this study has a wavelength of 2022.54 nm (approximately $2 \mu\text{m}$), being eye-safe and operating in the Mie scattering regime. The (vertical) resolution of the wind measurements depends on both the duration of the pulse, also called pulse width, and the distance that the signal can travel during the sampling time. The shorter the pulse, the better the spatial resolution, although a reasonable sampling duration is needed to ensure sufficient accuracy of the velocity estimation (Liu et al., 2019b). With a pulse width of ~ 400 ns and an averaging time of 1 s, we have a vertical resolution of 100 m (Witschas et al., 2017). Furthermore, the aircraft speed influences the horizontal resolution. Flying with approximately 200 m s^{-1} and having a sampling frequency of $\sim 40 \text{ s}$, the horizontal resolution (distance traveled between two measurements) is about 8 km. Pulsed LiDARs have a blind spot of tens to hundreds of meters near the beam source, depending on the pulse duration and range gate width (Liu et al., 2019b). Therefore, although flying at 7.5 km, the first wind velocities are obtained from approximately 7 km altitude down to the surface. The DWL employed in this study has previously been compared to dropsonde measurements, in which the mean systematic error has been found to remain below 0.1 m s^{-1} and the mean random error to vary between 0.92 and 1.5 m s^{-1} (Weissmann et al., 2005; Chouza et al., 2016; Schäfler et al., 2018; Witschas et al., 2020).

The Velocity-Azimuth Display technique (Browning and Wexler, 1968) with an off-nadir angle of 20 degrees, is used to retrieve all three wind components. The

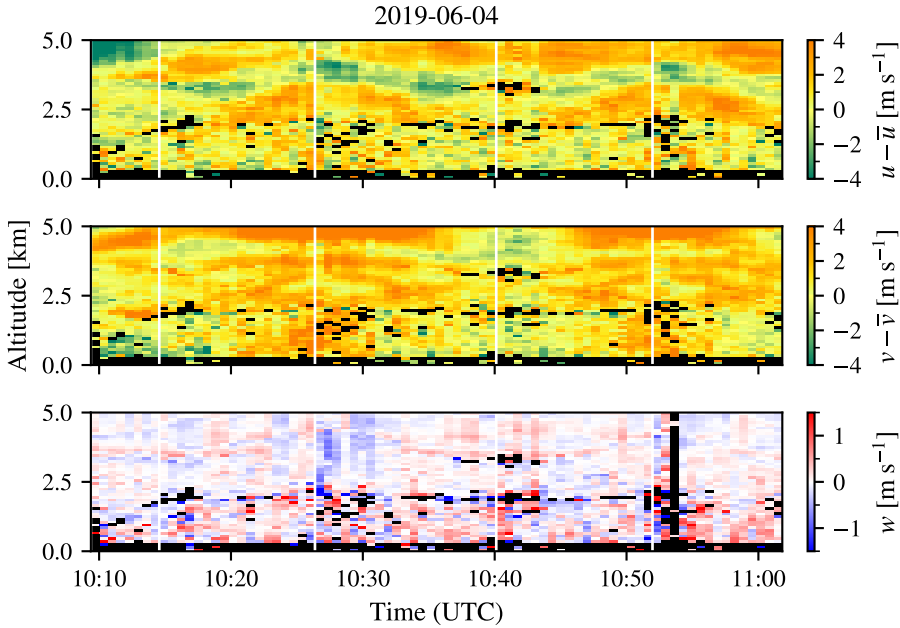


Figure 3.3: Anomalies of zonal (u), meridional (v), and vertical (w) wind measurements from the DWL, zoomed in on the lowest 5 km. Measurements taken on 2019-06-04. Missing values are indicated in black and often correspond to clouds (1-2 km altitude). White vertical lines indicate turning points at the ends of each the track.

processing algorithm that is applied to retrieve the wind vectors from one revolution of line-of-sight measurements is described in Witschas et al. (2017).

Figure 3.3 shows an example of the wind anomalies (i.e. the wind measurements of which the average wind during the measurement flight is subtracted) on June 4 2019. The turning points indicating reverse heading on the same leg are indicated with white vertical lines, revealing similar but mirrored wind structures on subsequent legs. On this particular flight, the track was moved further to the east around 11:40 UTC, where different structures are visible. Data gaps, which can be associated with clouds, are indicated in black.

The top of the boundary layer that is around 2 km altitude is clearly visible in the w fluctuations, with larger fluctuations below, and smaller above. The top of the boundary layer is marked by predominantly blue colours, indicating negative velocities produced by overshooting thermals that become negatively buoyant. Within the boundary layer updrafts generate the largest fluctuations, while a few downdrafts extending to the surface are also evident. It appears that the DWL can at least to some extent observe the coherent convective features that are responsible for mass transport of scalars and momentum. DWL is able to measure w with a much higher resolution, as used in (Witschas et al., 2017), but at the cost of having no information of u and v .

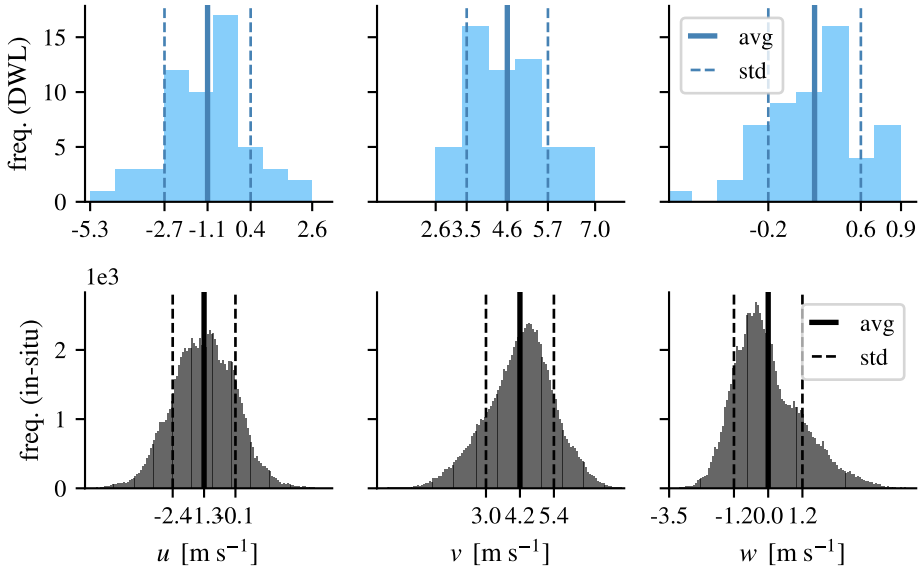


Figure 3.4: Distribution of u , v , and w wind in the sub-cloud layer of the western track at 617 m altitude on 2019-06-04, as measured by the Doppler Wind LiDAR (top panels, blue) and the in situ turbulence probe (lower panels, black). The DWL range bin closest to the in situ flight height have been used.

For one of the legs on 4 June, the histograms of the sub-cloud layer u , v , and w wind are compared in Figure 3.4. Mean horizontal wind measurements over this leg are comparable for the DWL and in-situ measurements. Despite its much coarser resolution and its missing v winds $< 2.5 \text{ m s}^{-1}$, the wind variance observed by the DWL is only slightly smaller (0.1 m s^{-1} less than in the in-situ measurements). This gives us confidence that the DWL can provide complementary information of the (horizontal) wind profile at heights where in situ measurements are absent. It also tells us that horizontal wind fluctuations are largely set by scales of 8 km or larger and that cloud convection scales of 1-2 km are less important. On the other hand, the vertical wind shows much less variation than the in situ measurements. This is explained by the much larger area that is measured by the DWL: it can only see the average vertical velocity in this area, which on average is much lower than the vertical velocity of vertical transient small eddies than can be better captured by the in situ measurements.

3.2.2 Updraft detection algorithm

Using conditional sampling we identify updrafts, following the method described and tested by Lenschow and Stephens (1980). We conditionally sample on updrafts ($w' > 0$ & $w > 0$) that are wider than 100 m, and that have an excess in absolute humidity $\rho'_v > 0.5 \sigma_{\rho'_v}$. This method is more robust than using virtual temperature

Table 3.1: This table shows the number of updrafts, relative updraft area, average updraft size, and average updraft speed for the legs flown on 4 June 2019.

Updraft statistics	Number of updrafts	Updraft area [% of leg]	Chord length [m]	Updraft velocity [m s^{-1}]
West (thicker clouds)				
Cloud top	8	2.3	264	1.6
Cloud layer	12	5.4	412	2.2
Cloud base	20	8.1	328	1.4
Mixed layer	16	8.2	333	1.7
East (thinner clouds)				
Cloud top	1	0.6	372	2.1
Cloud base	3	1.8	412	1.5
Mixed layer	10	4.7	289	1.4

or buoyancy, and can be applied both in the sub-cloud and cloud layer.

Table 3.1 shows the updraft statistics of the legs flown on 4 June 2019. It lists the number of updrafts, the relative length of the leg that they occupy, the average horizontal size and the average updraft velocity. We find that the fraction of the leg that is covered by updrafts (updraft area) decreases with height, although the average updraft chord length (the length of the updraft slice that we passed through) peaks at cloud base for the thinner clouds on the eastern track on June 4th as well for the clouds on 2019-05-24 (not shown). On May 24th, we find more and stronger updrafts in the cloud-topped mixed layer than under clear-skies, whereas updraft chord length is comparable. This is in correspondence with findings of *e.g.* Nicholls and LeMone (1980), who found stronger sub-cloud and lower cloud-layer vertical velocity standard deviation in more cloudy conditions. The largest average updraft velocity is found at cloud base, suggesting that the stronger mixed layer updrafts reach the lifted condensation level and benefit from the energy released at condensation. On June 4th, fastest average updraft speeds are found in the cloud layer in the case of thicker clouds. With the thinner clouds fastest updraft speed is found at cloud top, although we must be careful as this includes only one sample.

3.3 Flight conditions: wind and thermodynamic profiles

Although the three flight days all captured a shallow cloud regime, they differed substantially in their characteristics of the wind (wind speed, wind shear and directional shear), providing a set of diverse case studies, whose wind and thermodynamic profiles are described next. For the wind, an entire profile of the mean and variance are

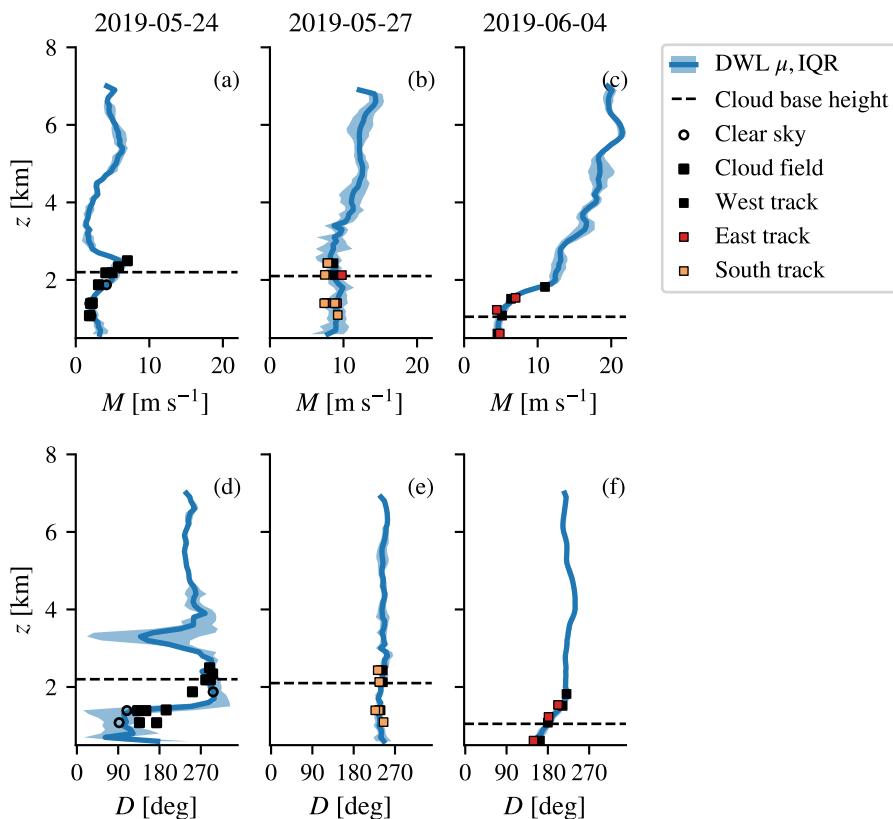


Figure 3.5: Average wind speed and wind direction profiles for each flight date. Average DWL profile indicated in blue, shading indicates the range between the first and third quartile. Average in situ measurement indicated with squares (measurements in/below cloud field areas) and circles (cloud free areas). Cloud base height (cbh) has been estimated during the flight and is indicated with a horizontal dashed line.

shown from the DWL, with the in situ measurements denoted on top (Figure 3.5). Except for the wind direction on May 24th, which varied greatly in the sub-cloud layer, the mean DWL and in situ winds compare very well.

The first flight (May 24) took place after a number of overcast days and heavy rain. Southern Germany was under influence of a broad area of high pressure west of Europe and over the Northern Atlantic and the conditions were very stable with hardly any clouds in Southern Germany. The northern part of the leg was flown over the Swabian Alps, where numerous gliders were making use of the thermal structures that typically develop here and shallow cumulus with cloud bases near 2 km (dashed horizontal lines) and tops near 2.5 km developed. These were the focus of our measurements. Winds were weak and reasonably well mixed up to 1400 m, topped by a layer with strong wind turning near 1.5 km (some 500 m below cloud

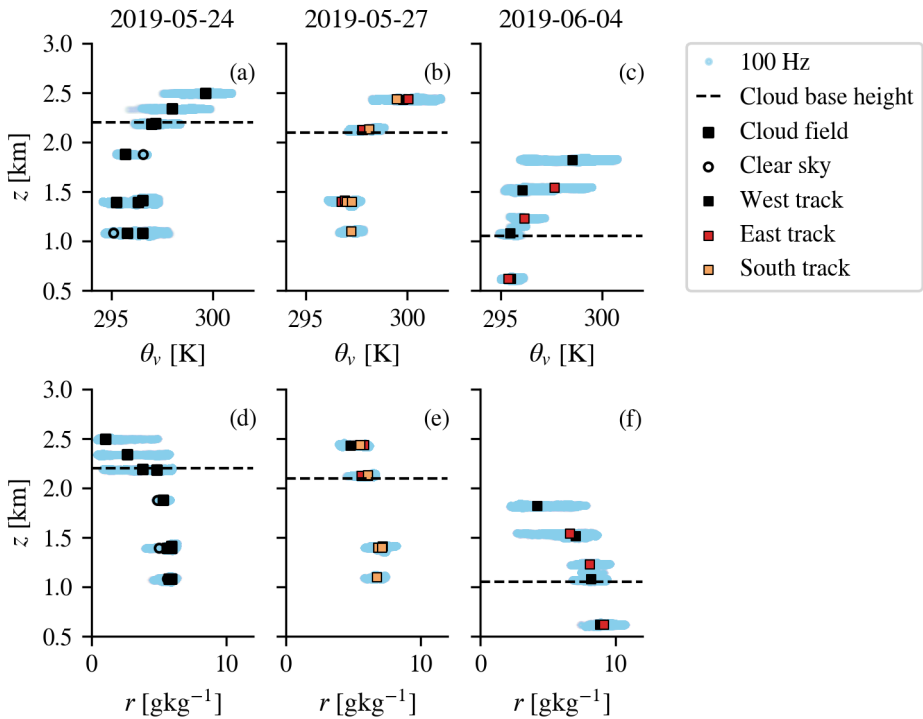


Figure 3.6: Virtual temperature and mixing ratio during the three flight days. On the first flight there were three legs that were partly below clear-sky and partly below cloudy sky. They have been separated and are represented by open circles and closed squares, respectively. The other two cases had multiple tracks that are indicated with different colours. The raw 100 Hz data is indicated in light blue. Cloud base is indicated by the dashed horizontal line.

base), and wind speed increased up to 2500 m in a layer extending through cloud base (Figure 3.5). In contrast, temperature and humidity were very well-mixed vertically. The atmosphere was relatively dry, with a pronounced inversion in temperature and moisture starting near 2.2 km (Figure 3.6), as well as a typical region of negative buoyancy flux below cloud base (Figure 3.7) that has not been captured in the other two flights.

Considerably stronger wind speeds, but far less wind shear were present during the second flight (May 27) when we sampled air masses ahead of a cold front located SW-NE across eastern Germany (Figures 3.1(b), 3.5 (b,e)). The air masses were somewhat warmer and moister, but with a thermodynamic structure and a cloud base similar to that of the first flight (Figure 3.6). Besides shallow convection, there was plenty of mid- and upper levels cloud, which we encountered at the end of the first flight leg towards the north. Later, the front seemed to break up and skies were clearer, especially towards the southeast. Eventually, also in the southeastern area of our operations, shallow cumulus made way for stratocumulus layers, with only rare

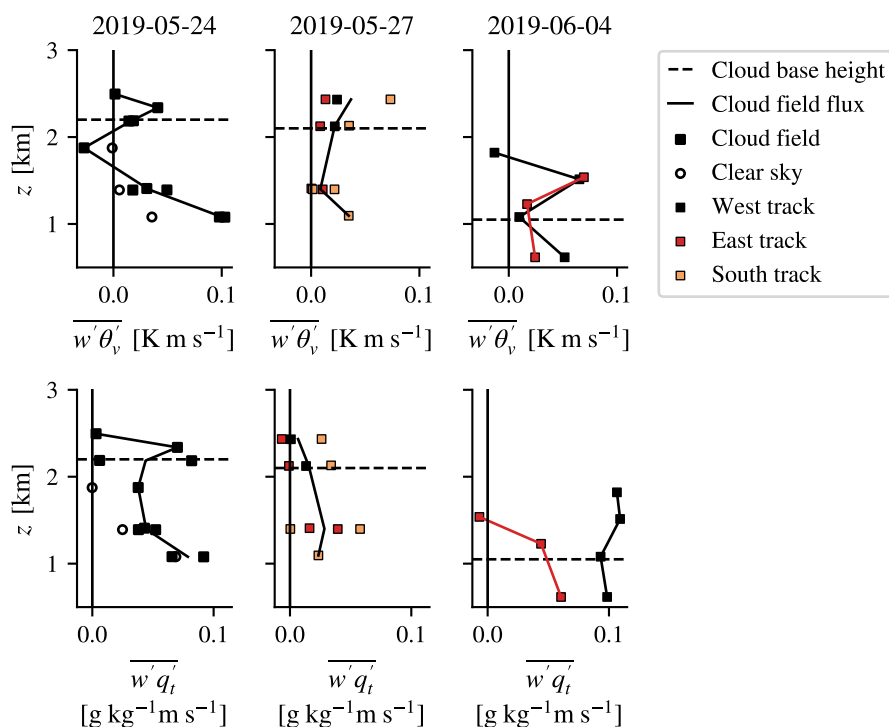


Figure 3.7: Profiles of buoyancy and the moisture flux for the three flight days. On the first flight there were three legs that were partly below clear-sky and partly below cloudy sky. They have been separated and are represented by open circles and closed squares, respectively. The other two cases had multiple tracks that are indicated with different colours. The average flux below cloudy skies has been indicated by a solid line, of which two are present in the last flight day to show the difference between the western and eastern track. Cloud base is indicated by the dashed horizontal line.

sights of clear sky and sunshine.

During the third flight (June 4th), we measured an extended field of shallow cumulus clouds that developed behind a cold front over northwestern Germany in air masses that were considerably colder and moister (Figure 3.6 (c,f)), with much lower cloud bases near 1000 (western N-S leg) and 1200 m (eastern N-S leg) and very diverse cloud top heights (see Figure 3.1(c)), with maximum tops near 2 km. The cloud field was organised in patches of alternating cloudy and cloud-free air masses. As the clouds were getting deeper towards the northern parts of the leg, the relative sizes of the patches increased. Difference in the inversion strength of the temperature profile is clearly visible between the western and eastern leg (Figure 3.6(c), as well as a large difference in moisture flux (Figure 3.7). Near- surface winds were weak and from the south, with strong shear and a turning from southeasterly to southwesterly winds right around cloud base (Figure 3.5(c,f)).

Based on the wind profiles, the three flights could be classified as having weak wind and strong shear either in the sub-cloud layer (Flight 1) or in the cloud layer (Flight 3), and having strong wind but little shear (Flight 2). In the next section, we will explore the associated turbulent statistics of these flights and evaluate whether the derived momentum flux profiles are in line with our expectations *e.g.*, that momentum fluxes throughout the mixed layer and cloud layer increase with wind shear as predicted by K-theory.

3.4 Momentum flux profiles

3.4.1 Sub-cloud and cloud layer profiles

In Figures 3.8 and 3.9 we consider the profiles of wind and momentum flux for the vector wind components u and v separately. As in Figure 3.5, the wind speed is shown for both the DWL (in blue) and the in situ turbulence probe at the flight levels (circles, squares). A guideline for the flux profiles in cloudy conditions are indicated with solid black lines, which are linearly interpolated between leg averaged values at the different flight levels (and are sometimes averaged over two legs the same level).

When fluxes are dominated by small-scale turbulent diffusion, it may be modeled (parametrized) by using so-called flux-gradient relationships, also known as K-diffusion. We find that most of the fluxes and their relationship with the wind gradient lead to a K-value that is in line with down-gradient diffusion, acting to reduce the wind gradient.

On May 24th, ignoring the strong gradients in u below ~ 700 m, $\partial_z u > 0$. This implies that air parcels that are displaced upward ($w' > 0$) generally have a negative u perturbation compared to their environment ($u' < 0$), acting to remove the wind gradient, in line with K-theory. This holds generally for all flight days. Negative u perturbations are in particular evident from the actual wind in air masses sampled within updrafts, which tend to be several m s^{-1} slower (pink triangles in Figure 3.8 and 3.9). Similarly, the meridional momentum fluxes are also down-gradient. For example, the gradient $\partial_z v < 0$ above 1 km on May 24th, corresponding to a positive meridional momentum flux ($\overline{v'w'} > 0$), and $\partial_z v > 0$ on June 4th, corresponding to $\overline{v'w'} < 0$.

The profiles of $\overline{u'w'}$, $\overline{v'w'}$ reveal that larger fluxes are measured on May 24th than on May 27th, in line with the stronger shear present in u and (to a lesser extent) in v . Fluxes typically decrease towards the boundary layer height (cloud top or mixed-layer top in case of clear sky), as the variance of vertical velocity decreases towards the top of the boundary layer (Figure 3.10).

Evidently, on May 24th the momentum fluxes throughout the mixed-layer increased considerably from the first transect of the flight, which captured a dry convective boundary layer (open circles), to the second transect, which is when cumulus clouds developed on top of the mixed layer (filled squares), although both transects have comparable u, v profiles (Figure 3.8 and 3.9). The larger fluxes reflect the pres-

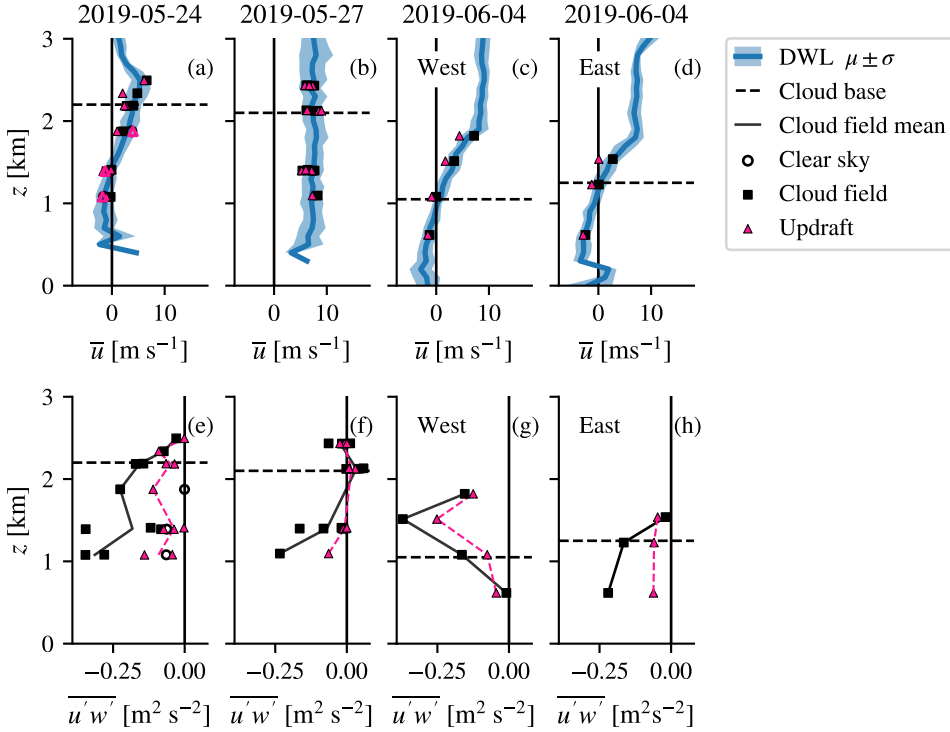


Figure 3.8: Average u (a-d) and $\overline{u'w'}$ (e-h) profiles for each flight date. The u -axis is positive eastward. To obtain these profiles, we applied the same averaging procedure as in Figure 3.5 and the eddy covariance method as described in Section 3.2.1. On 2019-05-24 (a,e), the clear-sky measurements are indicated with open circles, whereas measurements in cloud fields are indicated with filled squares. Pink triangles represent the wind speed within updrafts (upper panels) and updraft contribution to the total flux (lower panels).

ence of stronger turbulent eddies. Especially just below and at cloud base, much larger variances are present in u and v and throughout the mixed layer in w (Figure 3.10).

While on May 24th, 27th and the eastern leg on June 4th the fluxes decreased towards cloud base, with little flux remaining in the cloud layer, the western leg on June 4th shows an increase in momentum fluxes with height (in particular $\overline{u'w'}$ but also $\overline{v'w'}$). Whereas the flux in the mixed-layer below clouds is almost negligible, one of the largest fluxes was measured in the cloud layer ($\overline{u'w'} \sim 0.4 \text{ m}^2\text{s}^{-2}$). Clouds on this western leg had a lower base (just above 1 km) and higher cloud tops (up to 2 km) and thus were thicker than the clouds that were encountered on the eastern track. The thicker clouds do not only have larger momentum transport in the cloud layer, but also a much larger (percentage) contribution of the updraft to the total flux than any of the other measurements (Figure 3.6). The fraction of the leg that

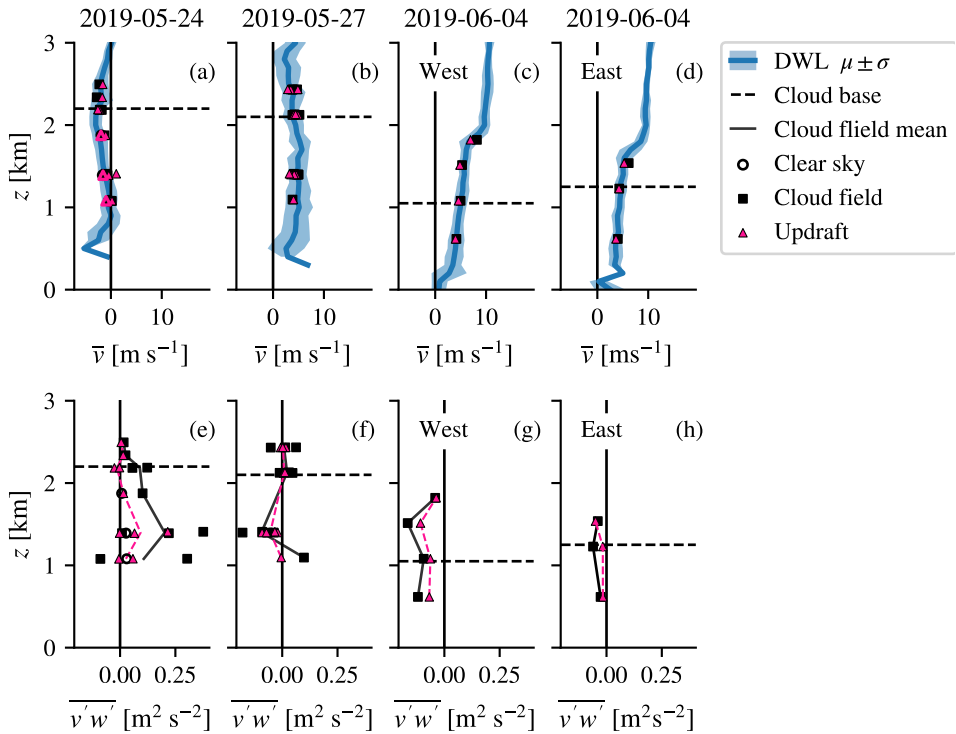
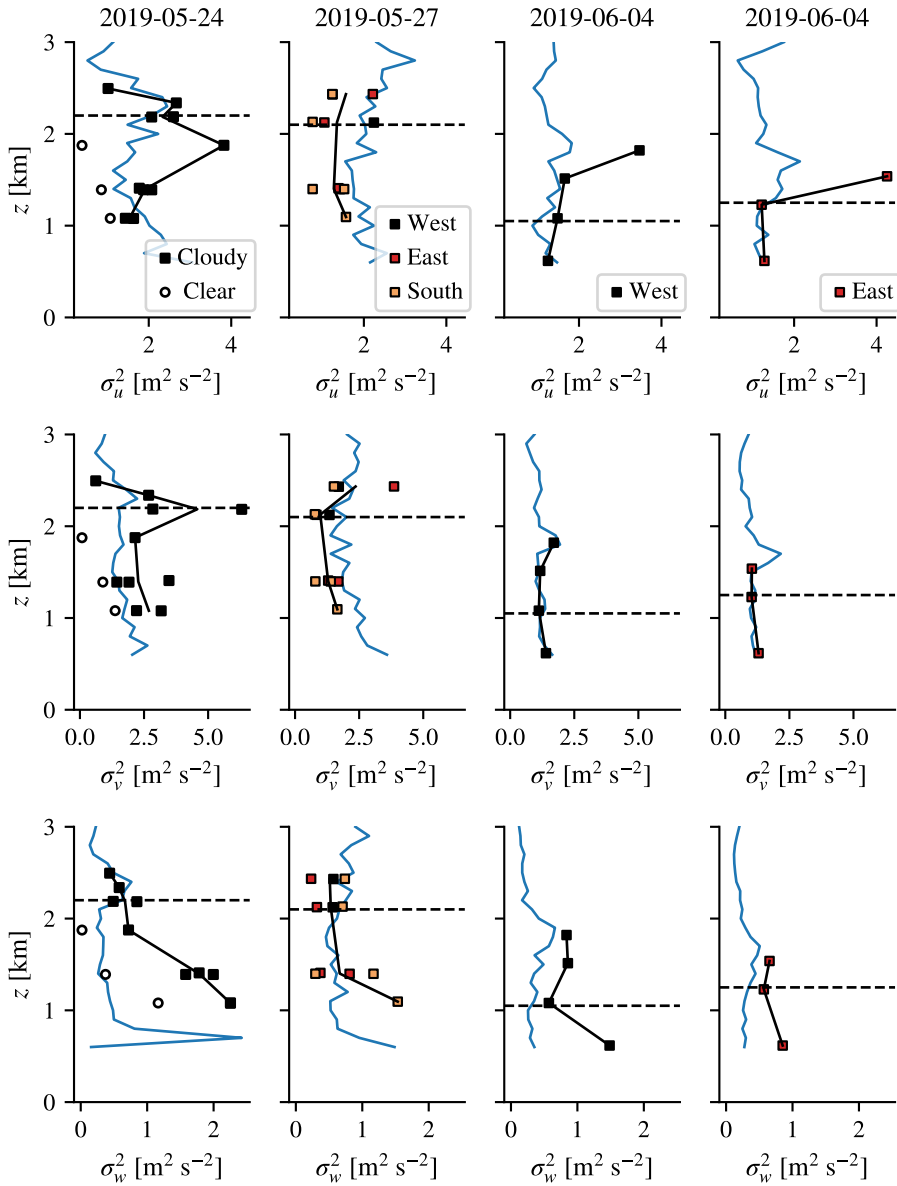


Figure 3.9: Same as Figure 3.8, but then for v and $v'w'$. The v -axis is positive northward.

was occupied by updrafts was also significantly larger than in all other cases. The deeper clouds may have been accompanied by wider updrafts with better protected cores that may be responsible for carrying larger fluxes.

Figure 3.11 shows a time series of turbulence measured at 600 m in the mixed layer on the western track on June 4th. In grey the unfiltered turbulence statistics are shown, while black shows the linearly detrended and high-pass filtered ($f > 0.01$ Hz) statistics. Cloudy updrafts can have vertical speeds up to 5 m s^{-1} , in both altitudes. Evidently, large buoyancy fluxes ($w'\theta'_v$, top row) are associated with large momentum fluxes (bottom row), which reveals the importance of convection in generating a large momentum flux. Sometimes, for instance at 11:33 UTC, the convergence (panel (e)) is closely tied to convection. Typically, updrafts carry wind speeds that are much slower (up to 5 m s^{-1} for cloudy updrafts) than the environment. Looking carefully, one might see that u' and w' peak at different times and that u' has a different sign in various updrafts. This could explain a much lower momentum flux. We discuss this further in the next sections, where we explore the fluxes sampled on (cloudy) updrafts, as well as how eddies of different scales contribute to the fluxes.

Figure 3.10: Variance of u' , v' , w' for each flight.

3.4.2 Scale contributions to flux

Observations in the surface layer, for instance during the Kansas experiment, show that the cospectra of the $\overline{u'w'}$ flux follow a fixed slope, with the large scales more significant (Kaimal et al., 1972). However, throughout the boundary layer, Large Eddy Simulations of various cases indicate that the momentum flux carried by small-scale

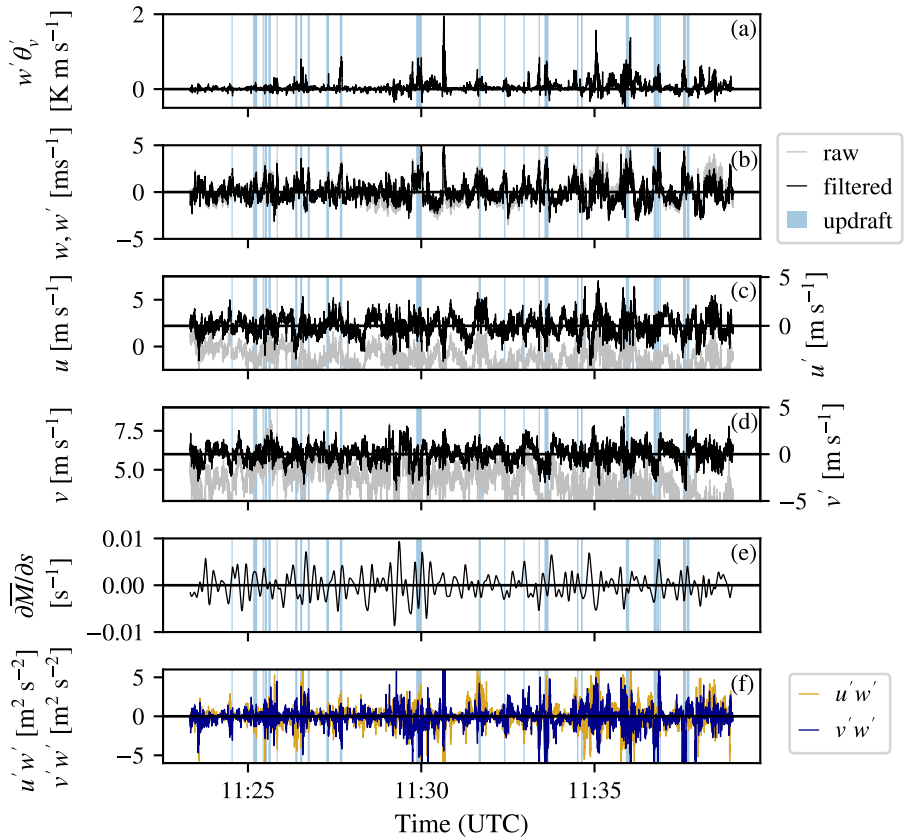


Figure 3.11: Raw (unfiltered) and fluctuating (filtered: linear detrended, high-pass filter cut-off 0.01 Hz) time series of (a) buoyancy flux, (b) vertical velocity, (c) zonal wind, (d) meridional wind, (e) convergence and divergence of the wind speed in the streamwise direction calculated using a low-pass filter that considers all scales larger than 700 m ($f_c < 0.1$ Hz), and (f) momentum fluxes measured using the Cessna probe on 2019-06-04 at 600 m, in the middle of the mixed layer of the western leg. Updrafts are indicated with light-blue shading.

shear-driven turbulent eddies (with a size smaller than ~ 200 m) can contribute more than 50% of momentum fluxes. Small scale turbulence may also transport momentum in an opposite direction than larger more coherent eddy structures (Zhu, 2015). This is particularly true for the lower mixed-layer and near cloud tops. However, in shallow cumulus cases, especially from the middle of the mixed-layer (sub-cloud layer) to the middle of the cloud layer, the net momentum fluxes are almost entirely carried by eddies with scales greater than 400 m (Zhu, 2015).

In Figure 3.12, the total (net) momentum flux is shown for the legs in the sub-cloud layer, near cloud base, within the cloud layer and near cloud top for June 4th.

The momentum flux at different scales is calculated using a high-pass filter filters that removes larger scales with increasing cut-off frequency. The flux all the way to the right is for instance carried by eddies up to a scale of $\sim 7\text{km}$, corresponding to a cut-off frequency of 0.01 Hz. When the flux magnitude increases rapidly from left to right, it implies that larger-scale eddies contribute more to the momentum flux than smaller scales. If considerable flux is already at smaller scales (higher cut-off frequencies), as is the case in the zonal flux at cloud top in the eastern leg, the smaller eddies play a more important role.

The results suggest that momentum fluxes carried by eddies of different scales can counteract to reduce the overall flux. The relatively small flux (in the profiles, Figures 3.8,3.9) for instance in $\overline{u'w'}$ in the mixed layer on the western leg with thicker clouds, is produced by a positive $\overline{u'w'}$ carried by scales larger than 2.8 km up to maximally 7 km ($f_c = 0.025 - 0.01\text{Hz}$), which almost compensates for the negative $\overline{u'w'}$ flux carried by turbulence on scales less than 2.8 km ($f_c = 0.025\text{Hz}$).

The same is true for $\overline{u'w'}$ near cloud top in the eastern leg with thinner clouds, and to a lesser extent, in the flux of $\overline{v'w'}$ in that leg within the mixed layer and near cloud tops. In the leg with thick clouds, the change in sign of the $\overline{v'w'}$ flux takes place already between 0.7 - 2.8 km. In other words: the profiles deviate from a profile where fluxes linearly decrease with height when scales beyond 1-2 km (cloud scale) play an important role.

Having less shear, for instance on 27 May, the fluxes are much smaller in general (Figure 3.8 and 3.9). There, smaller scales do not matter much and the flux is solely generated by the largest scales (not shown).

3.4.3 Conclusions

In this paper we aimed to investigate the variability in wind profiles and momentum fluxes under convective conditions, motivated by a lack of knowledge on the nature of the momentum flux profile in cloud-topped boundary layers. As in seminal marine cumulus field studies, we used traditional in-situ turbulence measurements on board a Cessna aircraft that flew 50 - 100 km tracks at different legs below and within the cloud layer. These measurements were complemented with downward profiling Doppler Wind Lidar (DWL) measurements onboard a Falcon aircraft that flew the same track at higher altitudes. DWL are not typically employed in field studies of convection and clouds, but can help elucidate flows on mesoscales that accompany (organized) convection.

We carried out a limited number of flights in different wind and convective conditions: from a day with calm winds, strong directional shear and clear-sky and convective cumulus humilis (of maximum 500 m extent) to two days with pre- and post-frontal convection that was deeper and embedded in flows with strong winds and weak shear respectively strong shear.

First, we aimed to answer how the wind profiles and variance in the in-situ and DWL measurements compare. Both the mean horizontal wind and the variance of horizontal wind at given heights compared well despite the much larger horizontal

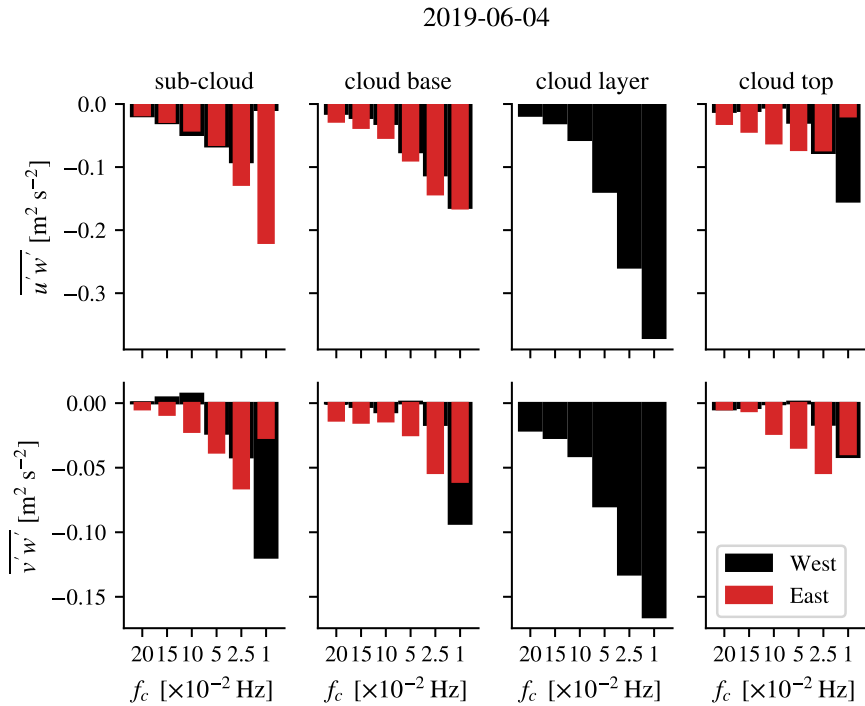


Figure 3.12: Scale contributions to the momentum flux $\overline{u'w'}$ (upper panels) and $\overline{v'w'}$ (lower panels) for different heights in the atmosphere. The bars in each panel represent the flux contribution, in which the left-most bar only includes small scales (frequencies exceeding 0.2 Hz) and the right-most bar includes all scales that are represented in the measurements limited to 7 km (with a cut-off frequency of 0.01 Hz, excluding lower frequencies). Filter scales are 0.20, 0.15, 0.10, 0.05, 0.025, and 0.001 Hz that, when assuming a cruising speed of 70 m s⁻¹, correspond to length scales of 350, 467, 700, 1400, 2800, and 7000 m. The black bars represent the western leg with thicker clouds, the red ones the eastern leg with thinner clouds.

sampling scale of the DWL (7 km opposed to 70 m). Wind fluctuations on scales larger than turbulence and (cloudy) updrafts (on meso-gamma scales from 2 - 20 km) were found to be up to ± 5 m s⁻¹. This emphasises that flight legs need to be sufficiently long to capture mesoscale fluctuations in the mean wind (and its variance).

The profiles of wind derived from the few sampling legs of the Cessna compared reasonably well with the DWL profiles, in other words, the wind profile did not evolve majorly during the course of the flight as the Cessna transitioned from one leg altitude to another. The DWL also revealed the location of up- and downdrafts, such as negative vertical velocities at the top of the boundary layer where thermal plumes encounter a warmer environment and become negatively buoyant.

Second, we asked whether the measured momentum flux profiles in the sub-cloud layer and in the cloud layer are in line with our expectation, as well as to

what extent we can explain them from convective updrafts alone. On the same flight day and even on the same track, substantial differences in the momentum flux could be seen associated with regions of convection. Most of the momentum flux profiles revealed down-gradient momentum transport that was generally strongest within the mixed-layer and decreasing towards cloud tops, but counter-gradient transport was also observed on the third flight day with post-frontal convection and strong shear, on which distinct alternating patches of clear-sky and sheared clouds of about 1 km deep were seen. Different flight segments, even on that same flight day, had a very different momentum flux profile that was not explained by turbulent transport across the local vertical gradient in the wind.

Although momentum fluxes generally increased in areas with (cloudy) updrafts, the contribution of the updraft to the total momentum flux was typically (only) a third to two-thirds, which is comparatively small considering the contribution of the updraft to the buoyancy flux. Horizontal momentum perturbations carried by updrafts below and within clouds were clearly distinguishable on all flights, but especially large on the third flight (up to almost 5 m s^{-1} in the cloud layer).

Finally, we asked which scales contribute significantly to wind variance and the momentum flux. We found that scales beyond 1 km contribute significantly to the momentum flux and there is clear evidence for compensating flux contributions from different scales. In the post-frontal convection day, cancellation of fluxes of different signs may have explained a differing momentum flux profile with relatively small fluxes in the well-mixed sub-cloud layer (compared to the fluxes in the cloud layer).

The limited number of flights do not allow us to draw a general conclusion across a wide range of convective states. Nevertheless, they highlight that momentum flux profiles and their variability require understanding of motions across a range of scales, with non-negligible contributions of the clear-sky fluxes and of mesoscales that may be coupled to the convection. Wind lidars can help elucidate the flows on larger than cloud scales and should be used more deliberately in studies of clouds and their spatial organization.

4

The wind structure below marine trade-wind cumulus

4.1 Introduction

Sailors have long used clouds to guide their ships into an area of favorable wind. Scientifically, the relationship between cumulus clouds and the wind is not trivial. In this chapter, we combine simultaneous observations from cloud radars and wind lidars, taken over the ocean, to visualise the wind structure around shallow trade-wind cumulus clouds and look at the wind mixing below clouds.

Winds can be modified by clouds in various ways. First, coming back to the sailors' wisdom, surface winds can be accelerated or slowed down when they align with or against the thermal circulation that is associated with the clouds (Marchaj, 1996, Fig. 245), as depicted in the left panel of Figure 4.1. This mechanism is especially strong if clouds are organised in roll convection that form "cloud streets" (LeMone and Pennell, 1976). Convective up- and downdrafts, the roots of cumulus clouds, also redistribute momentum throughout the boundary layer, a process known as convective momentum transport. Often momentum transport acts to reduce the wind gradient. However, more vigorous and randomly organized convective clouds have also been shown to transport momentum *counter gradient*, increasing the local wind shear (LeMone and Pennell, 1976).

Precipitation also changes the sub-cloud winds: As precipitation evaporates on its way to the surface, the air cools and becomes denser, accelerating downward. Near the surface, this pool of cold air spreads out in all directions, drastically changing the wind's speed and direction over areas several tens of kilometers (Figure 4.1, right panel). The gust fronts at the diverging edge of the cold pool are perhaps best known as occurring along with deep convection (Kurowski et al., 2018; Fournier and Haerter, 2019; Kirsch et al., 2021), but also evident for shallow precipitating systems

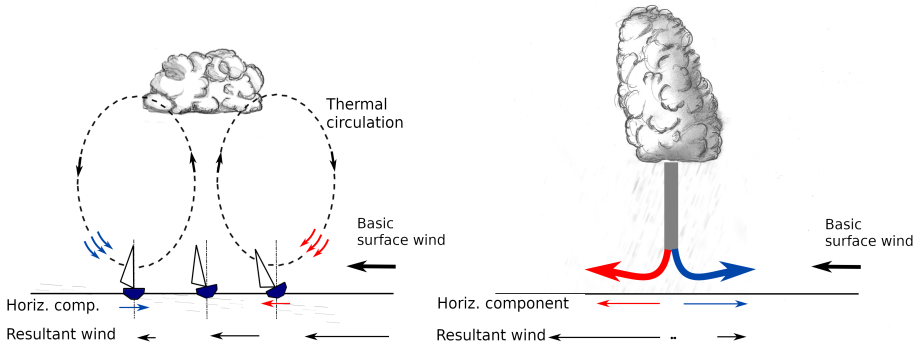


Figure 4.1: The different cloud impacts on wind. At the left the effect of a thermal circulation that is typical for cumulus cloud convection is shown (made after Marchaj (1996)). When branches align with the prevailing wind, they accelerate the local flow (red arrows). Opposing the prevailing wind leads to a local deceleration (blue arrow) of the wind. At the right, a thicker precipitating cloud is displayed that generates a cold pool effect on the wind. As the radial outflow aligns or opposes the prevailing flow, the wind is accelerated or decelerated. However, with a similar background wind, the resultant wind is faster upwind for the thermal circulation and faster downwind in case of cold pool conditions.

(Zuidema et al., 2017). The convergence zone between the fast gust front generated by the cold pool and the prevailing wind typically leads to new formation of clouds at the downwind side of the cold pool (Helfer and Nuijens, 2021).

Understanding what drives boundary layer winds matters because winds influence surface heat fluxes and modulate the surface friction, which influence the atmospheric stability. Winds furthermore affect wave formations, and thus air-sea interaction and the mixing in the ocean (e.g. Melville, 1996). Higher up in the atmosphere, wind shapes the cloud's macro-physical structure, impacting its vertical and horizontal dimensions and thus the radiative impact at surface (Malkus, 1949; Neggers et al., 2003; Yamaguchi et al., 2019; Brown, 1999; Helfer et al., 2020, e.g). The longevity and re-triggering of the cloud is also impacted: when the cloud is tilted, its precipitation shaft with downward motion is separated from its updraft, whereas clouds that grow vertically produce rain shafts that interfere with subsequent updrafts (Helfer and Nuijens, 2021).

Because shallow cumulus clouds are abundant around the world, their effect may be non-negligible. A former study over Cabauw, The Netherlands, showed that days with predominantly cumulus clouds (with a cloud cover up to 70%) have relatively weaker sub-cloud layer wind shear and stronger near-surface winds compared to days with only dry convective boundary layers (Koning et al., 2021). More coherent circulations in the sub-cloud layer accompanying moist convection overhead may be responsible for the larger and better mixed winds. Monin-Obukhov similarity functions, a common surface parametrization, may underestimate the surface friction that can be sustained in presence of convection: These functions do not account for larger-scale influences (circulations) from outside the surface layer, which may be

introduced when downdrafts penetrate the surface layer in the presence of convective shallow cumulus (Fodor et al., 2019; Liu et al., 2019a).

This study focuses on visualising what is rarely viewed: the local wind circulation that accompanies individual cumulus clouds. Because of the omnipresence of shallow cumulus clouds, the steady easterly winds, and a well developed boundary layer both during day and night, the trades provide an ideal laboratory to study this interaction. A large field campaign, EUREC4A (for more information, see (Bony et al., 2017b, 2020; Stevens et al., 2021)), took place over the ocean near Barbados between 20 January and 20 February 2020, in the drier winter season. During the campaign, which aimed to gain a better understanding of the role of shallow cumulus clouds in influencing the large-scale circulation, many measurement platforms and instruments were employed to measure a range of processes. In this work, we use the simultaneous measurements of the cloud radar and wind lidar aboard the research vessel Meteor – a unique high (time-) resolution dataset spanning a full month, which to our knowledge has never been measured before over the ocean. Such time series will contain sufficient amount of cloud observations, enabling us to separate the clouds into sufficiently large groups with which we can address the following questions:

- How do sub-cloud layer wind speed and wind shear change with cumulus clouds of varying thickness?
- Is there evidence in the wind measurements for (1) thermal circulations attached to clouds, or (2) correlations between vertical and horizontal winds that support the mass flux approach?

We expect to find signals that could prove the sailor’s theorem, which would imply an acceleration below the upwind edge of the cloud and a deceleration at the downwind side (the opposite signal is expected in case of a cold pool).

Furthermore, we look out for signatures of momentum transport by thermal updrafts that support the mass flux approach. That is, we expect that thermals transport slower surface winds upward into the clouds. With deeper clouds, an indication for stronger convective conditions, stronger updrafts and a more coherent plume are anticipated. The correlation between anomalies in horizontal and vertical winds may shed some light on the usability of the mass flux approach in representing (shallow) convective momentum transport.

The remainder of this chapter outlines the typical weather conditions during the EUREC4A campaign. The various measurement instruments are introduced along with the algorithm that identifies individual clouds in the cloud radar data set. Section 4.4 shows and discusses the wind structures for the various cloud groups. Last, we summarise the findings and put them into a broader context.

4.2 Data description

The EUREC4A campaign took place in the trade wind regions east from Barbados from January to February, 2020. During boreal winter there is less precipitation than during summer and subsidence prevails, maximizing to 30 hPa/day. Clouds are typically located between 1 and 3 km (Stevens et al., 2016). An overview of all participating measurement platforms can be found in Stevens et al. (2021). This study exploits the full EUREC4A measurement period of two instruments aboard R/V Meteor, the long range wind lidar and the cloud radar, which are described in the next sections.

4.2.1 Long-range wind lidar

The wind lidar data were obtained in a collaboration of TUD with Fraunhofer IWES (Dr. Julia Gottschall) and DTU Wind Energy (Prof. Dr. Jakob Mann) who were commissioned to perform measurements with a Ship Lidar System consisting of the two lidars and motion sensors during a research cruise from Emden / Germany to Barbados (on the R/V Merian), as well as during the intensive campaign near Barbados in January/February and during the back transfer to the Azores/Portugal (both on the RV Meteor). The instruments were monitored remotely by IWES Fraunhofer and on the ship by TUD graduate students Kevin Helfer and Geiske de Groot. All collected measurement data (from wind lidars and motion sensors) were combined and processed to high resolution (approximately 1 Hz) and as 10-min averages by Hugo Rubio Hurtado and Dr. Julia Gottschall at IWES Fraunhofer.

This study only uses data from the WindCube WLS70 aboard the R/V Meteor, in the full time period of the EUREC4A. The WLS70 measures wind at a wavelength of 1.54 micrometer, by measuring the movement of aerosols. With a resolution of 100m, it has a range between 100 m and 2 km. However, because the air above the mixed-layer is often too clean, wind measurements above 1 km are problematic. To minimize the number of erroneous wind measurements, we also exclude observations that have a carrier to noise ratio (CNR) less than -22 dB. The value of -22 dB is based on the work of Dias Neto et al. (2022). Figure 4.2 displays the average CNR during the campaign together with its standard deviation, showing that CNR generally exceeds (is more negative) the threshold between 640 to 960 m height. It also displays the hourly average wind during the campaign. There is a small gap in the wind data, when the lidar was not operational (see Figure 4.2, just before 4 February).

The smallest (horizontal) scales that can be detected, are determined by the half-opening angle of the wind lidar and the vertical distance. The lidar measures at four locations along a cone, with a sampling rate of 6 seconds per line of sight (LoS). The opposing measurements (180 degrees apart) determine the wind speed in a certain direction. Having an opening angle of 14.7 degrees, the opposing measurements near cloud base (800 m) that are considered representative for the movement of air along that line are $2 \cdot \tan(14.7^\circ) \cdot 800 \text{ m} = 420 \text{ m}$ apart. To obtain the wind

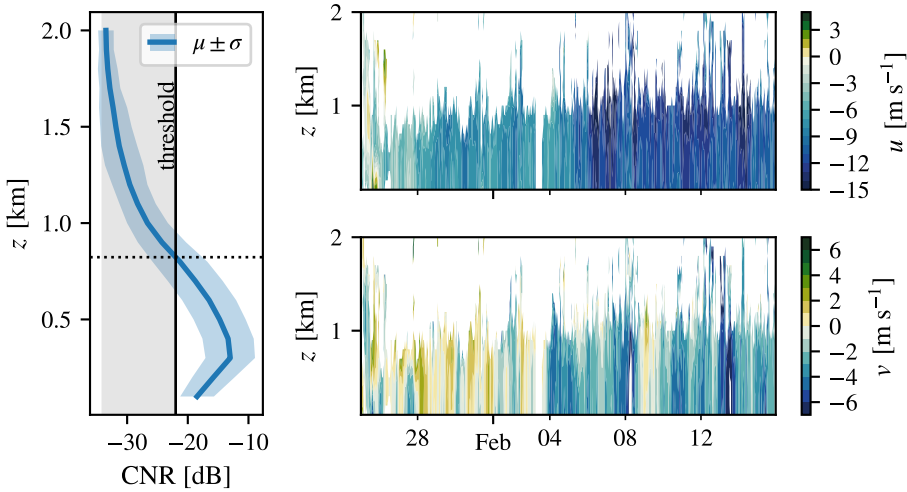


Figure 4.2: Left panel: Average (μ) and standard deviation (σ) of the carrier to noise ratio (CNR). Right panels: Hourly average u wind (top) and v wind (bottom) during the EUREC4A campaign. Although the WindCube WLS70 can measure up to 2 km height the air is often too clean. Furthermore, wind measurements that have a carrier to noise ratio (CNR) below -22 dB are disregarded. The horizontal dotted line indicates the average height of 825 m above which the CNR is lower than -22 dB.

components from the line of sight measurement, a sine curve is fitted through the raw measurements (see Ishwardat et al. (2017); Dias Neto et al. (2022) for the exact method). A difference in the wind speed measurement along the opposing line of sights would result in a change of wind speed (adjusting the amplitude of the fitted curve) or in a different vertical wind speed (a change in equilibrium position). No direct vertical pointing measurements were made.

To correct the lidar measurements for atmospheric conditions and ship motions, a weather station that collects temperature, relative humidity, and precipitation is installed, as well as a xSens MTi-G attitude and heading reference sensor and a Trimble SPS261 satellite compass. In the post-processing, the ship's cruising speed and heading are taken into account to find the actual wind speed in the north-south and east-west direction. Wind may also be affected by heave, roll and pitch. While on smaller vessels a 10 minute mean will average out these effects, on a larger vessel like the Meteor, this may not be the case. Assuming a random motion along the three axes, the effects are averaged out when the sample groups are large enough. The corrected LoS measurements were used to estimate the vertical wind speed, using the method described by Ishwardat et al. (2017); Dias Neto et al. (2022), which provide insight into the convective structures in the mixed-layer.

4.2.2 Doppler cloud radar

The bi-static Doppler cloud radar aboard the R/V Meteor stood on a passive stabilization platform, ensuring it is always pointing vertically upward. The radar works at a frequency modulated continuous wave stabilised at 94 GHz (W-band). The emitted microwave radiation is reflected (back-scattered) on hydro-meteors such as cloud droplets, ice crystals and rain. Reflectivity is used to identify cloud entities, cloud base and cloud top. Because the signal also includes rain, it is not possible to detect cloud base and cloud top during heavy rain, although in light rain conditions the cloud top can still be detected. The return signal is resolved in time, using an integration time of 1.5 - 3 seconds (1.5 s from 1 February onward, before 3 s), as well as in height, with a range resolution of 20 - 40 m.

4.3 Data Processing

4.3.1 Cloud entity selection

To investigate the momentum transport associated with different cloud conditions, we use a segmentation algorithm to detect echo objects in the cloud radar reflectivity that correspond to typical trade wind cumuli. This algorithm was developed to look at the development of trade wind cumuli in different environments (Lonitz et al., 2015). It sets a threshold for the reflectivity and then looks for all connected points along the time and height dimension, as well as in the diagonal (across both). We use a threshold of -50 dB, following Klingebiel et al. (2019). An example of a cloud entity selection is shown in Figure 4.3. After the entity selection, clouds with less than 5 points in total and clouds that pass by in less than 2 seconds are disregarded to avoid false cloud hits. Furthermore, we consider only clouds with a cloud base between 400 - 1000 m to lessen the inclusion of precipitation events, where cloud base is biased low. Isolated stratiform cloud that may have a higher cloud base are also excluded. For each cloud entity, a cloud overpass time and cloud chord length are obtained, which is used to select a window of wind measurements surrounding the cloud.

To separate cases of different convection, we divide the cloud population into groups based on cloud thickness (vertical depth). The first two groups contain clouds with a thickness between 250 - 500 m (613 clouds) and 500 - 1000 m (185 clouds), which are interpreted as shallow cumulus. The third group has clouds with a thickness between 1000 - 1500 m (45 clouds), which also contain raining clouds and clouds with stratiform outflow. Shallow clouds are most abundant in our dataset. Their appearance can be tied to specific organisation: on NASA's worldview images, 6 and 11 February 2020 displayed "sugar" patterns: very fine granular looking clouds with little clumping (Stevens et al., 2019). These days greatly contribute to the amount of observed shallow cumulus throughout the dataset, as on such a day around 100 clouds passed over our measurement location.

The distributions of cloud chord length, cloud base, cloud top, and aspect ratio

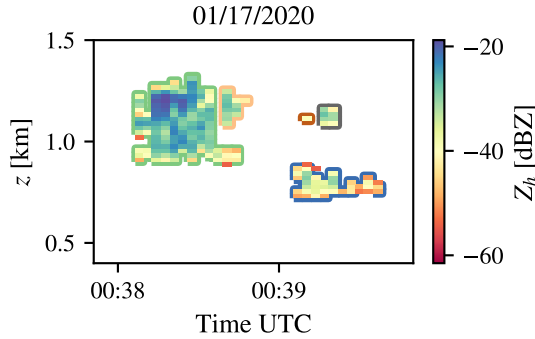


Figure 4.3: Cloud radar reflectivity (Z_h) for a few minute's time window. The coloured contours around the clouds show the different selected cloud entities. Grid-boxes with $Z_h < -50$ dB are not selected as part of the cloud.

are shown in Figure 4.4. Here, cloud chord length is defined as the distance between the left most edge and the right most edge of the cloud as it passes over the cloud radar. Cloud thickness is defined as the distance between the lowest detected cloud base point and the highest detected cloud top. Aspect ratio is the ratio of cloud chord length over cloud thickness. The figure shows that the chosen cloud groups are clearly separated and confirms that thicker clouds tend to have longer cloud chords. The aspect ratio is similar between groups.

The shallowest clouds have a cloud chord length around 100 m. Their duration is about 1-2 minutes, which is similar to the findings of Lamer et al. (2015) who report that non-precipitating cumulus are commonly around 300 m thick and have a duration of about 1 minute. Our second and third group are shallow clouds that have a cloud chord length of 150 - 250 m (overpass time between 1 - 3 minutes) and somewhat deeper clouds that may develop into precipitating clouds having a cloud chord length between 250 - 450 m (overpass time of 2-4 minutes). For each group, cloud chord length scales quite well with cloud thickness, peaking at an aspect ratio of 1. The peak is slightly asymmetric towards a larger aspect ratio, which indicates clouds that are wider than they are thick.

Wind anomalies

The local impact of clouds on the sub-cloud winds, can be seen when removing the average wind. We calculate and visualise the wind anomalies in the sub-cloud layer directly below and within a few cloud radii around the cloud. The wind anomalies are defined as:

$$u'(t, z) = u(t, z) - \langle u([t - \Delta t, t + \Delta t], z) \rangle \quad (4.1)$$

where $u'(t, z)$ denotes the anomaly at time t and height z , $u(t, z)$ the measurement value at the same time and height, from which $\langle u([t - \Delta t, t + \Delta t], z) \rangle$,

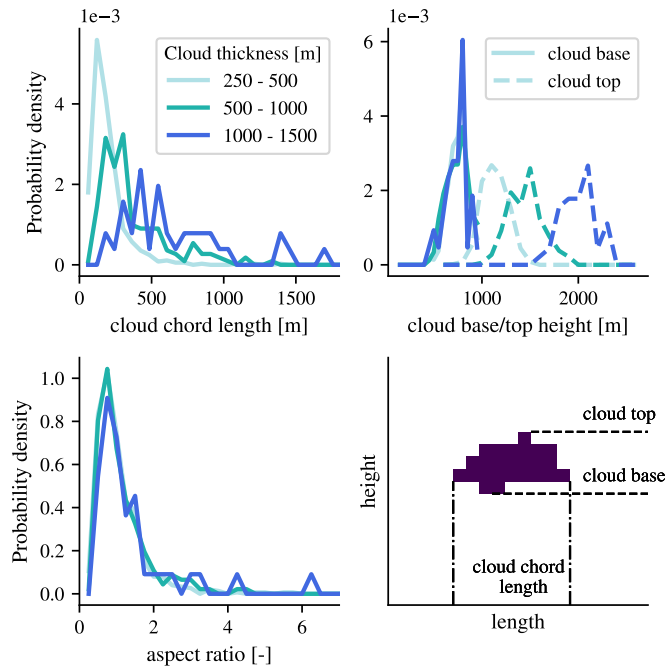


Figure 4.4: The normalised histogram (probability density) of cloud chord length (top left panel), cloud base and cloud top (top right panel), and aspect ratio (cloud chord length/cloud thickness, bottom left panel) is shown for each of the cloud thickness groups. Each group is represented by a different color. Cloud base and cloud top are shown in full and dashed lines, respectively. The cloud chord length and aspect ratio graph are truncated, as there was only small fluctuation in the tail. The bottom right panel shows how cloud base height, cloud top height, and cloud chord length are defined.

the moving average over $2\Delta t$ is subtracted. Taking a larger or a smaller Δt can be seen as taking a different filter size, filtering out certain turbulence scales (seconds to minutes) or even synoptic scales (hours). We took a time window ($2\Delta t$) of 10 min. This is closer to the life-time of a cumulus cloud, which is about 10-20 min, whereas a time scale of 30 minutes is often used for turbulent flux calculations. We tried a range of time windows (ranging from a few minutes to a few hours), where $\Delta t = 10$ minutes showed the clearest structures. The corresponding (horizontal) length scale is about 4.25 km (taking an average wind speed of 7 m/s). This time window includes turbulence and convection, but excludes synoptic, meso-alpha, and meso-beta scales. The diurnal cycle is also not considered.

4.4 Results

The results consists of three parts. First, the cloud appearance and its surroundings are shown, visualizing the average (normalised frequency of the) cloud occurrences

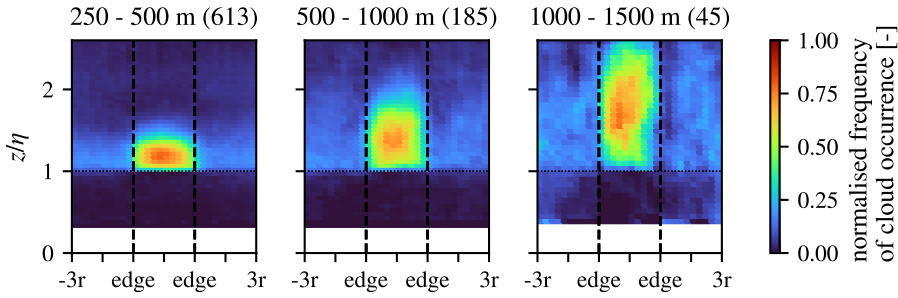


Figure 4.5: For each group with increasing cloud thickness, the normalised frequency of cloud occurrence is shown, as function of distance from the middle of the cloud base. In each grid point, a clear sky pixel has value 0 and each pixel containing cloud has value 1. The figure results from averaging all cloud environments in each groups. Cloud base is located at $z/\eta = 1$ and indicated with a dotted line. The cloud edges are shown with vertical dashed lines. The upwind side is right of the cloud, with positive cloud radii, whereas the downwind side has negative cloud radii distances. The number between brackets shows the amount of clouds within the group.

in a window of 3 cloud radii around each shallow cloud. Next, the campaign average (u, v) wind profiles are shown and compared to the average profiles that are present around clouds in each group. Last, we show the composites of anomalous wind in the sub-cloud layer that represent the wind structures around in each cloud group. There, we also answer the research questions that were defined in the introduction.

Appearance of cloud groups

To get an idea of the basic cloud shape of each group, as well as whether surrounding clouds are present within the three radii around the center of the cloud, the normalised frequency of cloud occurrence as function of the distance from the cloud center at the base of the cloud is shown in Figure 4.5. Scaling each cloud with cloud base and chord length, the (horizontal and vertical) grid points where the cloud resides are assigned a value 1, whereas all cloud-free points are assigned value 0. This is repeated for every cloud and averaged over all clouds within the group, yielding the normalised cloud occurrence. In Figure 4.5, cloud base is indicated with a horizontal dotted line at $z/\eta = 1$, cloud edges with a vertical dashed line. The downwind side of the cloud is indicated using negative cloud radii distances, the upwind side has positive values.

With increasing cloud thickness, the peak in cloud occurrence moves upwards and the number of normalised occurrence reduces, implying that cloudy points are more spread out. Cloud groups with thicker clouds contain more slanted clouds, precipitating clouds, clouds with stratiform outflow and occasionally some cumulus clouds that connect to a stratiform layer, which is identified as a single cloud. Around the thickest clouds there are more occurrences below $z/\eta = 1$, which are likely re-

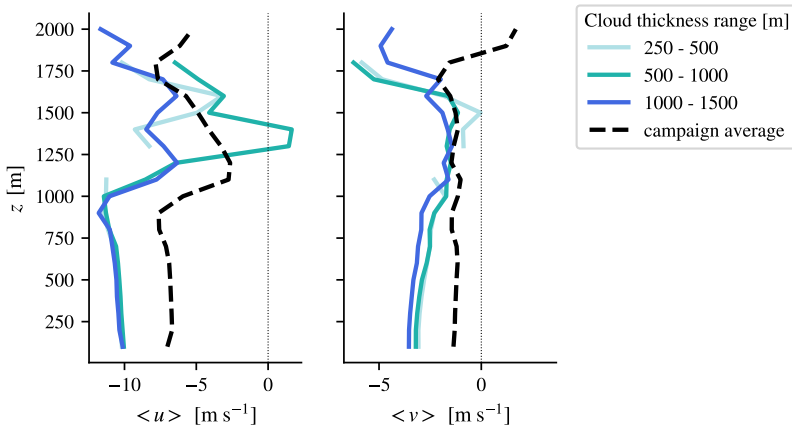


Figure 4.6: Composite of the average u and v wind within three cloud radii from the center of each cloud. A moving average of 10 minutes is applied to the wind vector time series before selecting the time window.

lated to rain events. The clouds seem not restricted to the indicated cloud edge: deeper clouds are embedded in larger cloud structures and individual clouds are less easily identified. Also horizontally, we find cloud occurrences, where they may not be expected. We saw that clouds often surround each other and many clouds are located above or below one another, and extend away from the selected cloud.

Wind profiles

Figure 4.6 shows the campaign average wind profiles and the wind within 3 cloud radii of the cloud (which is the second term on the right hand side in Equation 4.1 using $2\Delta t = 10$ min, averaged within 3 cloud radii from the center of the cloud). Around cumulus clouds, sub-cloud layer winds tend to have a stronger northerly and easterly component compared to the campaign average. This reflects that cloud are generally favored in conditions of stronger winds (Nuijens et al., 2009). On average, the sub-cloud wind profiles (below 800 m) are well-mixed below 800 m, which often covers the full sub-cloud layer. A significant difference between the campaign average shear and that of the three cloud groups was not found.

The campaign average profile as well as that of the two thicker cloud groups shows a maximum in the u wind near cloud base and a decrease in wind speed above, which is typical for the winter trades (Holland and Rasmusson, 1973; Brümmer et al., 1974; Brueck et al., 2014). However, we must be careful with interpreting the wind profiles above 1000 m, because of the absence of sufficient aerosols and a deterioration of the signal in clouds themselves.

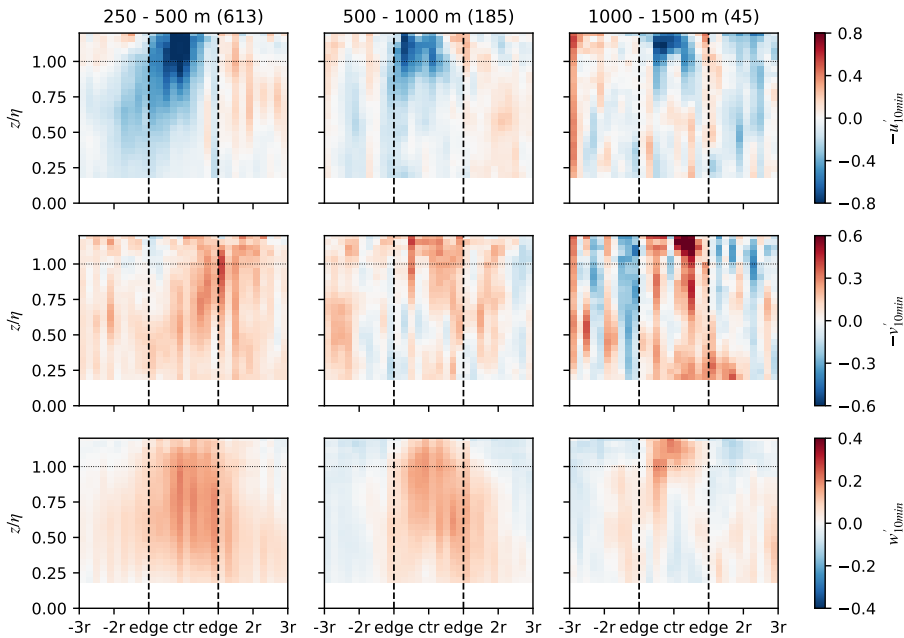


Figure 4.7: Composite of the anomalies in the three wind components having used a moving average of 10 minutes. The sign for u' and v' have been altered so that faster winds are indicated in red, slower winds in blue (for easterly and northerly winds). Please note the different colour scales for each wind component. Cloud edge is indicated with the vertical dashed line. The horizontal dotted line indicates cloud base height. The wind structure has been vertically normalised to cloud base height and horizontally scaled to show 3 cloud radii from the cloud centre. Upwind is to the right, indicated with positive cloud radii.

Anomalous sub-cloud layer wind structure

Following the procedure described in Section 4.3.1, wind anomalies are computed. After horizontal and vertical scaling, a composite of the (average) wind anomalies is obtained and shown in Figure 4.7. The number of clouds included in the composite is shown between brackets. The top panels show the zonal wind anomalies, the middle row the meridional anomalies. A minus is introduced in the zonal and meridional anomalous winds, so that positive anomalies (red) indicate faster wind, and negative values (blue) indicate slower winds compared to the average within a 10 minute time window around that measurement point. The vertical wind anomalies have a conventional sign: positive (red) upward and negative (blue) downward. To better see the wind structures, the color scales have a different range for each wind component.

Although clouds are typically present in faster easterly winds, as shown in Figure 4.6, inside clouds winds are slower than the mean easterly winds and faster than the mean southward flow around the clouds. The u -winds show a clear signal of slower winds near cloud base in all cloud groups, a signal which extends below cloud base.

The slower in-cloud wind speeds may be explained by updrafts that carry a few ms^{-1} slower easterly wind from near the surface towards cloud base, where the easterly wind maximizes (Fig. 4.7). The largest friction is present in the shallowest cloud group, also resembled in the signal of the medium thick clouds. The group with clouds thicker than 1 km show a different structure. Therefore, we will discuss the clouds up to 1 km thickness together before we analyse the thicker clouds.

Below 250 - 1000 m thick clouds (the first two cloud groups), we find regions (plumes) of stronger vertical motion, compared to their surroundings. Although such a signature is in itself unsurprising, as we believe the clouds have strong roots in the sub-cloud layer, the signal was expected to be stronger for thicker, more convective clouds. The updraft structure (w') becomes more distinct in the medium thick clouds: with a clearer downward motion at each side of the updraft. McMichael et al. (2020) observed that subsiding shells in shallow cumulus can reach down to 400 m below cloud base, with cloud base between 700-1000 m, this roughly corresponds to the $z/\eta = 0.5$ that we find for the shallowest clouds. Both plumes with faster w winds look slightly slanted, trailing from the lowest measurements at the upwind (right) side of the cloud to right below cloud base, following the shear in the average wind profiles (Fig. 4.6). However, because no direct vertical pointing measurement has been performed, we do not over-interpret this signal. In the u wind, mostly in the shallowest cloud group, a hint of a plume structure is found: an area of slower wind is present from $z/\eta = 0.5$ at the upwind edge of the cloud slanting up to above cloud base. However, the direction of the slope in u is directed opposite to that in the vertical component. The thickest clouds show a strong correlation between the two updraft plumes and anomalies in the u and v components, where the v component anomalies are more pronounced than in the other categories.

Looking for structures that indicate the presence of a thermal circulation, on which the sailor's theorem is based, we expect faster (surface) winds at the upwind side of the cloud and slower winds at the downwind side (see Figure 4.1). Indeed, the zonal anomalies, which are very similar to the wind speed anomalies (not shown), show faster u upwind of the cloud and slower wind at the downwind side. However, for the thinnest clouds, this signature is only present upwards from the middle of the sub-cloud layer. Also the structure of the vertical wind is not as we expected: within 3 radii from the middle of the cloud, there is mean upward motion with some neutral (non-moving) air at both sides around cloud base ($z/\eta = 1$). With somewhat deeper clouds, associated with stronger convection, subsiding areas surround the cloud and the slightly tilted updraft. The circulation structure becomes more visible when visualising the u, w vector in Figure 4.8. The shallowest clouds have a thermal and horizontal convergence from winds that are much slower below and downwind of the cloud. The medium thick cloud group does show a circulation pattern, which extends further down to the surface at the downwind side.

The sailor's theorem is not found for the shallowest clouds, the medium thick cloud comply better with the theorem. However, whereas the circulation extends towards the surface at the downwind side, the return flow at the upwind side of the cloud takes place at higher altitudes. This implies that the sailor's would not benefit

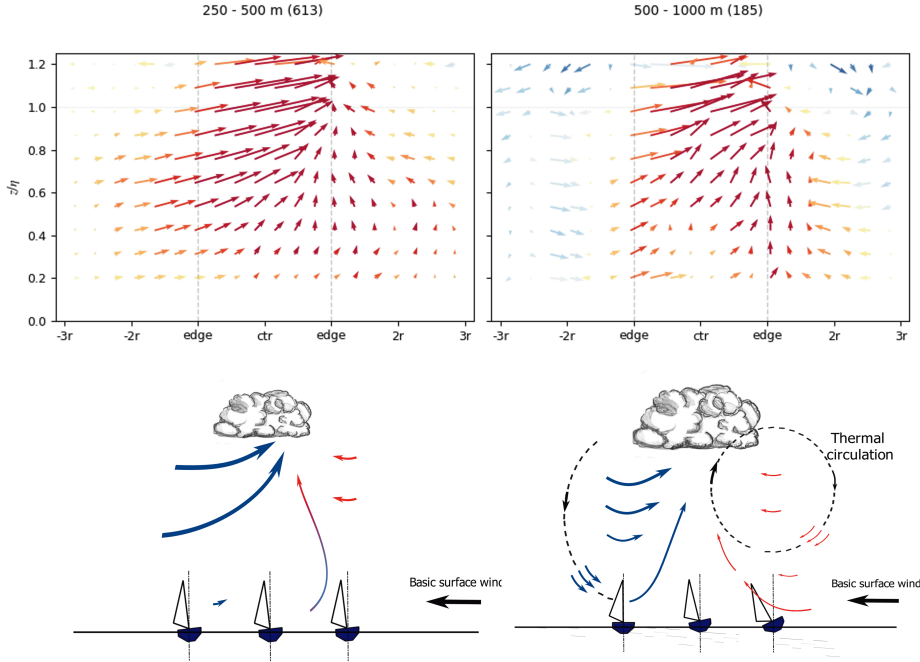


Figure 4.8: The top panels visualize the anomalous air-movement in the u, w domain for the shallowest clouds (left) and middle thick clouds (right). The deeper red the arrows, the stronger the updraft, whereas deeper blue depicts stronger downdrafts. Yellow arrows represent the near neutral vertical movements. The bottom panels give a schematic interpretation of the wind structure. As u is the dominant wind direction, it resembles the structure for wind speed. The v -component (near-cross wind) picture is omitted, but may add some complexity to the flow.

from a faster wind at the upwind side of the cloud, but do experience hindrance at the downwind side. A schematic overview is also given in the bottom panels of Figure 4.8.

Considering the validity of the mass flux approach, a correlation between an upward plume and slower u and faster v winds would be expected. (Faster v winds are expected based on the v wind profile where the southward movement becomes weaker with height.) Strongest indications of a mass flux are present near cloud base in all cloud groups, where the horizontal wind anomalies correlate best with the vertical motion. There, the (anomalous) upward motion is faster below the cloud than in its surroundings, likely due to latent heat release by condensation. Zonal winds are also slower than outside the cloud, reaching differences in the anomaly composite that slightly exceed 1 ms^{-1} in the shallowest clouds and that are around 0.5 ms^{-1} for the middle category. The anomaly structure of the thicker clouds is not as clear as in clouds between 250 - 1000 m. Two plumes of upward motion contain signals of slower u wind and faster v winds. This category may have signals from

raining clouds (cold pool effects) and stronger mesoscale circulations.

4.5 Summary and outlook

This chapter explored the wind structures around shallow cumulus clouds using syn-ergetic measurements of a cloud radar and long-range wind lidar aboard the R/V Meteor during the EUREC4A campaign that took place in the oceanic trade wind region near Barbados from January to February 2020. A cloud entity algorithm identified (shallow) cumulus clouds, around which we selected a window of 3 cloud radii (extending to either side of the cloud's center) to look at the wind speed, wind shear, and the wind anomalies that expose the wind structure. We asked how these differ between groups of diverse cloud thickness and whether we observe indications of thermal circulations or a mass flux in wind structure as represented by wind anomalies.

The wind is dominated by the easterly winds that have a magnitude around 7 m s^{-1} . Within all cloud groups, the easterly winds have a larger magnitude of 10 m s^{-1} . Cloud formation typically favours faster winds, which can explain this difference. Wind shear is generally small, both in the cloud conditioned wind profiles as well as in the campaign average. A significant different shear has not been found.

Composites of the wind anomalies reveal the wind structures in each cloud group. The structures in the shallowest and medium thick cloud groups are quite similar. Although the clouds prevail in periods of faster wind, they tend to move slower than the mean zonal wind, and faster than the average meridional wind. Vertical wind anomalies are positive in cumulus cloud conditions. The effects in the horizontal winds can be explained by lifted parcels that carry winds from the surface where weaker easterlies and stronger northerlies are present compared to the cloud layer. The "cumulus friction" is maximally 1 ms^{-1} in the zonal wind near cloud base. A circulation matching the sailor's theorem has been found accompanying clouds between 500-1000 m thick, although the circulation is not as symmetric as in Figure 4.1 and suggests that especially in the downwind disadvantage of cumulus clouds should be emphasized. Horizontal convergence is not confined to the surface layer and extends all the way to cloud base, where it gets even stronger. Although the patterns of the anomalous wind in u are similar between the smaller and medium thick clouds, the smaller clouds are embedded in an atmosphere with mean upward motion and have strong horizontal inflow in the u direction from the downwind side of the cloud. This is summarized in the bottom panels of Figure 4.8.

The strongest cumulus friction, here defined as the difference in wind speed inside and outside of the cloud, is observed in the shallowest cloud group. Although the medium thick cloud group strongly resembles the structure around the shallower clouds, there are also some differences: First, cumulus friction within the cloud is somewhat weaker; Second, upwind of the cloud, subsidence is more evident and extends further down. This may contribute to the faster winds that are observed upwind of the cloud, that are also present over a deeper layer than with the shallower clouds. The thickest clouds show a more complex structure in all wind components,

likely due because they are accompanied by precipitation, mesoscale flows and occur as part of large cloud clusters. However, a stronger correlation between the three wind components is visible, hinting at more coherent plumes throughout the sub-cloud layer corresponding to a structure that is expected from the mass flux approach.

Continuing this work, the effect of yaw, pitch, and roll on the wind anomalies should be reviewed. Furthermore, one could look more into the detailed surface-layer wind structures using a short-wave lidar that was also deployed aboard the R/V Meteor. Because surface fluxes have been measured aboard the R/V Meteor, opportunities also lie in analysing the surface fluxes during a cloud passage. Moreover, the Barbados cloud observatory collected simultaneous measurements of clouds and wind profiles during a couple of months from March to September 2019 that may provide additional statistics and can shed light on the wind structures in a setting of slower winds and less suppressed conditions.

5

Conclusions and perspectives

The interaction of cloud and winds through (shallow) convective momentum transport (CMT) is an uncertainty in weather and climate prediction that has received relatively little attention by the community. Thus far, the scarcity of wind measurements through cloudy boundary layers have not led to much insights or constraints on the influence of CMT on the wind.

This thesis investigates the role of shallow moist convection on wind profiles and momentum transport in the boundary layer from an observational perspective. The focus is on (shallow and mediocre) cumulus clouds that are abundant over land in the mid-latitudes as well as over the sub-tropical oceans. The overarching question of this thesis is:

"How do clouds affect momentum transport and the wind profile in the atmospheric boundary layer?"

Specifically,

1. How do the wind and momentum transport in the surface, sub-cloud, and cloud layer vary from dry to moist convective regimes?
2. Which scales contribute most to (convective) momentum transport?
3. What are the implications for parametrization schemes such as Monin-Obukhov similarity theory (surface layer), eddy diffusivity (sub-cloud layer) or the mass flux approach (sub-cloud and cloud layer)?

Because the research in this thesis is mostly based on observations, but observing momentum transport is not without challenges, the first section is dedicated to a discussion of the available observations for answering these questions. After that, the main findings are summarized and future research directions are discussed.

5.1 Observations and pseudo-observations

This thesis uses four data sets, each having its own challenges and benefits for the study of momentum transport. Chapter 2 uses observations from the Cabauw site, The Netherlands, which has employed a measurement mast since 1972, expanding the number of instruments considerably since then. It developed into a platform for joint atmospheric research, first by the CESAR consortium (2002) and now as part of the Ruisdael Observatory.

The many collocated observations consist of in-situ measurements in the surface layer and remote sensing measurements for the rest of the lower troposphere. The long data record allows for statistical sampling across various weather regimes. For example, in this thesis, nine year of data of wind profiles, cloud base height, surface radiation, heat, moisture, and momentum fluxes were used to study how momentum transport changes with different weather and cloud conditions.

The tower measurements that are based on high frequency sampling of wind and scalar quantities have several disadvantages when it comes to studying convective momentum transport:

- Measurements are taken at discrete heights and do not extend above 200 m.
- Measurements represent a single point (or at most the footprint) and may not be representative for a broader area.
- Flux measurements are derived using a 10 minute averaging window, defining a relevant time scale for flux transport a priori.
- The observed flux can be driven by many processes (advection, pressure gradients, turbulence, etc.). Therefore, the *convective* momentum transport cannot be extracted. Scale or wavelet analysis must be used to get an idea of the contribution of convection to the flux.

In this thesis, we overcome some of the challenges by using complementary pseudo-observations in the form of high-resolution large-eddy simulations. Nine years of daily realistic hindcasts were performed with a model that is optimized for running on GPUs, which uses much less computational power. The LES was run on a relatively small domain with dimensions of approximately 8 by 8 km² (horizontal) by 5 km (vertical). Although this is arguably small compared to the LES runs performed nowadays (on the order of 100 - 200 km in one horizontal dimension), it is not necessarily a drawback: for a comparison against a single point observation small LES domains have been shown to follow the synoptic conditions more closely, aiding comparison to local measurements (Schemann et al., 2020).

Two other observational datasets have been used: one was collected as part of the European Research Council (ERC) CloudBrake project (Chapter 3), and one as part of the broader international field campaign called EUREC4A (Chapter 4).

The CloudBrake project involved a flight campaign that encompassed three flights or case studies of cloud-wind interaction in shallow convective cloud conditions over

Germany in May 2019. The three measurement flights targeted different convective conditions.

The first flight took place after a number of days with heavy rain. The atmosphere was relatively dry with weak winds and a strong inversion. There were areas of clear-sky and areas of cumulus humilis (~ 500 m thick) that developed over the sun-lid sides of the hills, providing a clear view downward for the wind lidar.

The second flight took place just ahead of a cold front, capturing a mixture of shallow cumulus and stratocumulus layers. Above the shallow clouds (that were about 1 km thick), also mid-level altocumulus and altostratus layers were present, often reducing the DWL's view on the winds below. The planned tracks needed to be moved more often to keep targeting shallow cumulus conditions, due to the changing cloud decks associated with the movement of the front, which was faster than expected. Although the set flight levels for each track were thus not all completed, the atmospheric conditions were quite similar throughout the area, likely strongly driven by the synoptic conditions. Therefore, the transport and wind mixing associated with shallow clouds was difficult to assess.

The third flight took place after the passage of a cold front. Deeper popcorn-like convection was found and two tracks were flown approximately 40 km apart, but with different cloud thicknesses (300 m vs. 700 m). This was a very good case for comparing different convection strengths in similar atmospheric conditions. Sufficient clear sky was present between the clouds to obtain good wind profiles from the DWL.

The flight strategy included high-frequency (100 Hz) in situ wind measurements from a Cessna aeroplane in the cloudy boundary layer combined with downward looking Doppler wind lidar (DWL) profiling from a Falcon aeroplane flying the same track overhead at high altitude. (Measurements are thus not fully collocated, but do target the same area.) Although in situ turbulence measurements have been collected in previous cloud studies, never has a DWL been flown at the same time.

DWL profiling is not suitable for turbulence studies, but provides information of changes in the large-scale wind profile during the flight, exposes the mesoscale flows that accompany (organized) convection, and thereby helps interpret the momentum flux that is calculated from local wind measurements. Despite DWL's much coarser resolution compared to the in-situ measurements (due to the larger measurement volume and the lower sampling frequency, and faster air speed of the aeroplane), the DWL largely captures the range of the variance of the horizontal wind when comparing in-situ and DWL observations at the same height.

Momentum transport observations are only obtained from the in-situ measurements. Other than at the Cabauw tower, the measured time-series is often regarded as a spatial measurement of a (static) turbulent field, as the aeroplane moves much faster than the air mass (Taylor's frozen turbulence hypothesis). The smallest scales that are captured for the momentum flux calculations are limited by the sampling frequency, whereas the largest scales depend on the flown leg length. Typically the largest length scale that can be discerned from these flights is somewhat over 7 km. Furthermore, a choice must be made for obtaining the fluctuations for the flux calcu-

lations. Linear fits (trends) are often subtracted to obtain the fluctuations, but here a filtering is applied to remove contributions from length scales that are not properly captured (in this case scales larger than 7 km).

The last data used in this thesis targets a very different location: the marine subtropical boundary layer, where winds are much steadier, diurnal cycles are predictable, and (shallow) cumulus are ubiquitous. Designed for the study of cloud-circulation coupling, EUREC4A collected a wide variety of airborne and shipborne measurements during a month long period. Winds were measured in several ways: wind profiles throughout the sub-cloud mixed layer (up to cloud base) were collected by ship- and ground-based scanning DWLs, while radiosondes and dropsondes were launched at regular time intervals to probe a deeper atmospheric layer. Near the surface, wind measurements were taken as part of standard meteorological measurements at the BCO sites, at all research vessels, but also on board unmanned aerial vehicles and sail drones. This thesis targeted the long-range DWLs deployed on board of the research Vessel *Meteor*. This DWL was able to measure up to 2000 m, the aerosol loading in the cloud layer was often too low to get good returns, so that the wind lidar data is mostly confined to below cloud base. Simultaneous measurements by the cloud radar onboard the RV *Meteor* enabled a link between wind and the observed clouds.

5.2 Observation-based insights into (C)MT

Wind mixing and momentum transport in the boundary layer

Shallow cumulus clouds can be found in a large variety of weather situations, as can be seen from the three flight cases, but also when looking at individual days over Cabauw. On some days, the change in the synoptic flow during the day is pronounced, for instance on second flight (Chapter 3), which makes it difficult to address the influence of convection on the mean wind of a particular day. Differences in wind found on shallow cumulus and clear sky days thus only become visible when averaging over many days. The Cabauw study looked at groups of clear-sky and cumulus days with increasing cloud cover ranges. Over Cabauw, clear-sky days and cumulus days are found to have similar diurnal cycles, but days with cumulus clouds up to 70% cloud cover maintain faster surface winds. Wind mixing depends largely on the atmospheric stability and the strength of the background wind: stronger (200 m) wind implies stronger (surface layer) shear, whereas stronger instability implies better mixing. Correcting for these two parameters shows that less wind shear is present in the upper half of the surface layer under shallow cumulus with a cloud cover up to 70%. In other words: in the presence of moist convection, the winds in the surface layer are relatively strong compared to days with only dry convection. Nearby individual clouds over the trade-wind ocean, where atmospheric stability and winds are much more constant, the sub-cloud wind is also relatively stronger compared to the campaign average. This hints at deeper or more efficient wind mixing across the boundary layer in the presence of clouds.

Using the pseudo-observations of LES over Cabauw, the wind and momentum transport profiles were analysed throughout the boundary layer. In the sub-cloud and cloud layer, the momentum flux profile depends largely on the shear. Local shear-driven turbulent exchange of momentum dominates in the direction of the flow, establishing a so-called down-gradient momentum flux profile (see Chapter 1, section 1.1.1). The magnitude of momentum flux is a strong function of the areal cloud fraction (cloud cover). Larger cloud cover leads to more momentum transport in the cloud layer. Assuming similar cloud updraft speeds, this would follow a mass flux-based estimate of CMT.

In the cross-wind direction (orthogonal to the flow), the wind profile is generally well-mixed with only little wind turning within the sub-cloud or well-mixed layer. However, across cloud base, a jump in the cross-wind profile indicates a strong wind turning. The momentum flux in the cross-wind direction maximizes between the middle and top of the mixed-layer, where also the vertical velocity maximizes, accelerating the cross-wind flow in the lower part and decelerating the cross-wind flow towards the top of the mixed layer. Although the magnitude of the cross-wind flow is much smaller than that of the flow along the main wind direction, the cross-wind momentum flux contributes non-negligibly to the total momentum flux. This also suggests a deceleration of wind is larger towards cloud base than in the lower mixed-layer.

The impact of the amount and depth of convection on the momentum flux profile was especially evident from the flight observations over Germany. During the third measurement day, clouds reaching up to 1800 m (base at 1000 m) had little flux in the sub-cloud layer, but strong momentum fluxes through the cloud layer and moderate fluxes near cloud top. The shallower clouds that reached up to 1500 m (base at 1200 m) had relatively more momentum flux in the sub-cloud layer, a similar flux at cloud base, but little flux remaining at cloud top. Scale analysis shows that the difference in flux between the deeper and shallow clouds is mostly explained by the scales on the order of 1 - 10 km, which contribute significantly to the flux. Their contribution can act to reinforce or oppose the transport done by smaller scales, in the latter case reducing the net transport, sometimes to almost zero, or even changing the sign of the momentum flux.

Variations in the wind structure can provide insight into the dynamics of the momentum transport and their relation to clouds. From the flight campaign, mesoscale variations in wind on scales on the order of a few kilometers are revealed in the DWL wind anomalies from the leg means. Convergence or divergence zones could also be identified. These mesoscale circulations and the role they may play in momentum transport are not yet well understood.

On a smaller scale, wind composites of groups of increasing cloud thickness were studied using data from the R/V Meteor deployed during the EUREC4A campaign. The clouds were generally embedded in faster winds, both in the zonal and the meridional direction (compared to the EUREC4A mean wind). The wind structure directly underneath the shallowest (250 - 500 m thick) and medium (500 - 1000 m thick) clouds were similar. Compared to the average wind in a 10-minute time win-

dow, faster updrafts and meridional winds were revealed, whereas zonal winds were slower. Evidence of weaker winds below and within clouds ('cumulus friction') was found in all groups, where the largest wind anomaly was found under the shallowest cumulus. Underneath those clouds a plume of slower zonal winds originated from the middle of the sub-cloud layer at the downwind side, slanting upwards to cloud base. The shallow and medium cloud groups show similar behaviour, but enhanced convection in the medium clouds appears to form a thermal circulation that affects the wind all the way down to the surface, as predicted by the sailor's theorem. However, whereas the downwind side indeed shows slower winds, the benefits of faster wind at the upwind side are marginal. The thickest cloud group (1 - 1.5 km thick) showed a more complex structure of multiple updrafts and downdrafts that correlated well with the anomalies in the u and v wind, as is expected in mass flux-like momentum transport (visual assessment).

Implications for parametrization schemes

Monin-Obukhov similarity theory (MOST) relates the wind gradient in the surface layer to the momentum flux. Calculating the non-dimensional gradient, a smaller gradient is present in the upper surface layer on days with cumulus clouds than on clear-sky days. When a similar wind gradient is present on both days, this means that more momentum flux would be generated on cumulus days. The use of MOST for parametrization would thus underestimate the generated flux in the surface layer on cumulus days. This may be caused by violating the MOST assumption that the surface layer is not disturbed by processes from outside, which thus does not consider convective up- and downdrafts associated with clouds.

The pseudo observations from LES show that in the mean wind direction, momentum transport profiles look much like a profile as predicted by eddy diffusivity. In the cross wind component, the wind and flux profile remind of a smoothed flux-jump like profile, having the maximum flux a bit lower than expected. However, the flight measurements show us the large differences that can be present in alike situations, making it challenging to find accurate parametrization. But even when we assume that CMT is correctly parametrized for each cloud regime, the problem would come down to simulating the correct cloud types and cloud depth – a whole different challenge.

The mass flux approach is not directly tested, but is assessed based on the wind structures that are found below shallow cumulus clouds: is there visual evidence for a plume that is significantly different than the environment surrounding the cloud and updraft plume? Near cloud base, we observed much slower winds with a clear trace of slower wind down to the surface. This suggests that a dry mass flux of momentum is a necessary addition to an eddy-diffusivity scheme used in the boundary layer. Below the clouds, the correlation between upward motion and wind anomalies was not found to be very strong. This is likely a result of the limitation imposed by the indirect measurement of vertical wind and the size of the measurement volume of the DWL.

The impact of coherent convective circulations and mesoscales on the wind structure and hence the momentum flux show the importance of non-local transport. However, the opposing contributions that can occur between various scales makes it difficult to capture their influence and the mass flux parametrization will not necessarily capture this behaviour.

5.3 Recommendations

To continue the analysis of the wind variability in the presence of clouds, 3D wind observations would be necessary across the depth of the sub-cloud and cloud layer, preferably at a high enough resolution to enable flux calculations. Great opportunities lie with existing meteorological sites that already provide a synergy of atmospheric observations. At the Cabauw observatory, the CMTRACE campaign combines cloud radar and wind lidar data to obtain a full wind profile (Dias Neto et al., 2022), demonstrating a method to advance our understanding of wind flows surrounding clouds and their associated CMT, and may also be valuable for model validation and assimilation. Especially separate measurements of horizontal and vertical wind, in addition to measuring clouds, will help the interpretation of coherent convective circulations from the sub-cloud layer to the cloud layer.

Comparing the measured surface flux at Cabauw with that of LES for each cloud regime (Chapter 2), we found a difference between the two. There are several hypotheses for this discrepancy: 1) We compare a domain averaged LES flux with an instantaneous observed flux, 2) The observed flux is based on eddy covariance estimation taking a 10 minute time window. LES fluxes may include larger time scales that could contribute significantly to the larger flux, 3) Cabauw may experience more surface roughness than the LES, whose roughness is based on the CORINE land cover data set. This dataset considers elements with a minimum width of 100 m, so that e.g. tree rows are not considered. Understanding the origin of the difference between observations and the LES may indicate which processes are missed in LES or which time scales prove essential for the (near) surface flux. This becomes especially important as numerical weather prediction (NWP) models move to higher resolution, and if LES is applied to validate NWP models.

For comparison with observations, a small domain or a domain subset is ideal (Schemann et al., 2020). However, somewhat deeper clouds, such as congestus clouds, are traditionally not well captured in small domain LES. The current development of LES to simulate larger domains and open (opposed to periodic) boundary conditions, may provide a good opportunity to study mesoscale momentum transport.

The understanding of momentum transport requires thinking in three wind components. While models view the horizontal wind in u and v , for the interpretation of wind and momentum transport it is sometimes easier to think in a frame of along- and cross-wind, for instance when little wind turning is present. Feedback between the orthogonal wind components e.g. through evolving pressure gradients, Coriolis force, or convergence and divergence patterns can also complicate the analysis of the

influence of convective processes on the mean wind.

Because of the different reasoning between observationalists, theorists, and modelers, bringing these together will lead to a more integral understanding (of any process), which will result in better representation of these processes in models, improvement or advancement of theory, and better designs for measurements, aiding the entire community.

Bibliography

- Agee, E., and A. Gluhovsky, 1999: Les model sensitivities to domains, grids, and large-eddy timescales. *Journal of the Atmospheric Sciences*, **56** (4), 599 – 604, doi:10.1175/1520-0469(1999)056<0599:LMSTDG>2.0.CO;2, URL https://journals.ametsoc.org/view/journals/atsc/56/4/1520-0469_1999_056_0599_lmstdg_2.0.co_2.xml.
- Arakawa, A., and W. Schubert, 1974: Interaction of a cumulus cloud ensemble with the large-scale environment, part i. *Journal of Atmospheric Sciences*, **31** (3), 674 – 701, doi:10.1175/1520-0469(1974)031<0674:IOACCE>2.0.CO;2, URL https://journals.ametsoc.org/view/journals/atsc/31/3/1520-0469_1974_031_0674_ioacce_2_0_co_2.xml.
- Arrillaga, J., J. Vilá-Guerau de Arellano, F. Bosveld, H. Klein Baltink, C. Yagüe, M. Sastre, and C. Román-Cascón, 2018: Impacts of afternoon and evening sea-breeze fronts on local turbulence, and on co2 and radon-222 transport. *Quarterly Journal of the Royal Meteorological Society*, **144** (713), 990–1011, doi:<https://doi.org/10.1002/qj.3252>, URL <https://rmets.onlinelibrary.wiley.com/doi/abs/10.1002/qj.3252>.
- Baas, P, F. C. Bosveld, H. Klein Baltink, and A. A. M. Holtslag, 2009: A climatology of nocturnal low-level jets at cabauw. *Journal of Applied Meteorology and Climatology*, **48** (8), 1627–1642, URL <https://doi.org/10.1175/2009JAMC1965.1>.
- Badlan, R., T. Lane, M. Moncrieff, and C. Jakob, 2017: Insights into convective momentum transport and its parametrization from idealized simulations of organized convection. *Quarterly Journal of the Royal Meteorological Society*, **143** (708), 2687–2702, doi:<https://doi.org.tudelft.idm.oclc.org/10.1002/qj.3118>, URL <https://rmets-onlinelibrary-wiley-com.tudelft.idm.oclc.org/doi/abs/10.1002/qj.3118>, <https://rmets-onlinelibrary-wiley-com.tudelft.idm.oclc.org/doi/pdf/10.1002/qj.3118>.
- Baidar, S., T. Bonin, A. Choukulkar, A. Brewer, and M. Hardesty, 2020: Observation of the urban wind island effect. *EPJ Web Conferences*, doi:10.1051/epjconf/202023706009, URL <http://dx.doi.org/10.1051/epjconf/202023706009>.
- Bakhshi, R., and P. Sandborn, 2020: Maximizing the returns of lidar systems in wind farms for yaw error correction applications. *Wind Energy*, **23** (6), 1408–1421, doi:<https://doi.org/10.1002/we.2493>, URL <https://onlinelibrary.wiley.com/doi/abs/10.1002/we.2493>, <https://onlinelibrary.wiley.com/doi/pdf/10.1002/we.2493>.
- Banta, R., Y. Pichugina, N. Kelley, R. Hardesty, and W. Brewer, 2013: Wind energy meteorology: Insight into wind properties in the turbine-rotor layer of the atmosphere from high-resolution doppler lidar. *Bulletin of the American Meteorological Society*, **94** (6), 883 – 902, doi:10.1175/BAMS-D-11-00057.1, URL <https://journals.ametsoc.org/view/journals/bams/94/6/bams-d-11-00057.1.xml>.
- Bauweraerts, P., and J. Meyers, 2019: On the feasibility of using large-eddy simulations for real-time turbulent-flow forecasting in the atmospheric boundary layer. *Boundary-Layer Meteorology*, **171**, 213–235, doi:10.1007/s10546-019-00428-5, URL <https://doi.org/10.1007/s10546-019-00428-5>.
- Betts, A. K., 1973: Non-precipitating cumulus convection and its parameterization. *Quarterly Journal of the Royal Meteorological Society*, **99** (419), 178–196, doi:<https://doi.org.tudelft.idm.oclc.org/10.1002/qj.49709941915>, URL <https://rmets-onlinelibrary-wiley-com.tudelft.idm.oclc.org/doi/abs/10.1002/qj.49709941915>, <https://rmets-onlinelibrary-wiley-com.tudelft.idm.oclc.org/doi/pdf/10.1002/qj.49709941915>.
- Bolton, D., 1980: The computation of equivalent potential temperature. *Monthly Weather Review*, **108** (7), 1046–1053, URL https://journals.ametsoc.org/view/journals/mwre/108/7/1520-0493_1980_108_

- 1046_tcocept_2_0_co_2.xml.
- Bony, S., and J. Dufresne, 2005: Marine boundary layer clouds at the heart of tropical cloud feedback uncertainties in climate models. *Geophysical Research Letters*, **32** (20).
- Bony, S., H. Schulz, J. Vial, and B. Stevens, 2020: Sugar, gravel, fish, and flowers: Dependence of mesoscale patterns of trade-wind clouds on environmental conditions. *Geophysical Research Letters*, **47** (7), e2019GL085988, doi:<https://doi-org.tudelft.idm.oclc.org/10.1029/2019GL085988>, URL <https://agupubs-onlinelibrary-wiley-com.tudelft.idm.oclc.org/doi/abs/10.1029/2019GL085988>, e2019GL085988 10.1029/2019GL085988, <https://agupubs-onlinelibrary-wiley-com.tudelft.idm.oclc.org/doi/pdf/10.1029/2019GL085988>.
- Bony, S., B. Stevens, and D. Carlson, 2017a: Understanding clouds to anticipate future climate. *WMO Bulletin*, **66**, 8–11.
- Bony, S., and Coauthors, 2017b: EUREC4A: A Field Campaign to Elucidate the Couplings Between Clouds, Convection and Circulation. *Surveys in Geophysics*, 1–40, doi:[10.1007/s10712-017-9428-0](https://doi.org/10.1007/s10712-017-9428-0).
- Bosveld, F., 1999: The knmi garden experiment: micro-meteorological observations 1988 - 1989 corrections. Tech. rep., KNMI, De Bilt, The Netherlands. URL http://projects.knmi.nl/cabauw/insitu/observations/documentation/Cabauw_TR/Cabauw_TR.pdf.
- Bosveld, F., 2020: The cabauw in-situ observational program 2000 - present: Instruments, calibrations and set-up. Tech. rep., KNMI. URL <https://cdn.knmi.nl/knmi/pdf/bibliotheek/knmi/TR/TR384.pdf>.
- Bosveld, F., P. Baas, A. Beljaars, A. Holtslag, J. Vila-Gerau de Arellano, and B. van de Wiel, 2020: Fifty years of atmospheric boundary-layer research at cabauw serving weather, air quality and climate. *Boundary-Layer Meteorology*, doi:[10.1007/s10546-020-00541-w](https://doi.org/10.1007/s10546-020-00541-w), URL <https://doi.org/10.1007/s10546-020-00541-w>.
- Botnick, A., and E. Fedorovich, 2008: *Large Eddy Simulation of Atmospheric Convective Boundary Layer with Realistic Environmental Forcings*, 193–204. Springer Netherlands, Dordrecht, doi:[10.1007/978-1-4020-8578-9_16](https://doi.org/10.1007/978-1-4020-8578-9_16), URL https://doi.org/10.1007/978-1-4020-8578-9_16.
- Bretherton, C., and P. Bosles, 2017: Understanding mesoscale aggregation of shallow cumulus convection using large-eddy simulation. *Journal of Advances in Modeling Earth Systems*, **9** (8), 2798–2821.
- Brill, K., and B. Albrecht, 1982: Diurnal variation of the trade-wind boundary layer. *Monthly Weather Review*, **110** (6), 601 – 613, doi:[10.1175/1520-0493\(1982\)110<0601:DVOTTW>2.0.CO;2](https://doi.org/10.1175/1520-0493(1982)110<0601:DVOTTW>2.0.CO;2), URL https://journals.ametsoc.org/view/journals/mwre/110/6/1520-0493_1982_110_0601_dvottw_2_0_co_2.xml.
- Brilouet, P.-E., and Coauthors, 2021: The eurec4a turbulence dataset derived from the safire atr 42 aircraft. *Earth System Science Data*, **13** (7), 3379–3398, doi:[10.5194/essd-13-3379-2021](https://doi.org/10.5194/essd-13-3379-2021), URL <https://essd.copernicus.org/articles/13/3379/2021/>.
- Brown, A., 1999: Large-eddy simulation and parametrization of the effects of shear on shallow cumulus convection. *Boundary-layer meteorology*, **91** (1), 65–80.
- Brown, A., and A. Grant, 1997: Non-local mixing of momentum in the convective boundary layer. *Boundary-Layer Meteorology*, **84**, 1–22.
- Browning, K. A., and R. Wexler, 1968: The determination of kinematic properties of a wind field using doppler radar, journal of applied meteorology and climatology. *Journal of Applied Meteorology and Climatology*, **1** (7), 105–113, doi:[10.1175/1520-0450](https://doi.org/10.1175/1520-0450), URL https://journals.ametsoc.org/view/journals/apme/7/1/1520-0450_1968_007_0105_tdokpo_2_0_co_2.xml.
- Brueck, M., L. Nuijens, and B. Stevens, 2014: On the Seasonal and Synoptic Time-Scale Variability of the North Atlantic Trade Wind Region and Its Low-Level Clouds. *Journal of the Atmospheric Sciences*, **72** (4), 1428–1446, doi:[10.1175/JAS-D-14-0054.1](https://doi.org/10.1175/JAS-D-14-0054.1), URL <http://dx.doi.org/10.1175/JAS-D-14-0054.1>.
- Brümmer, B., E. Augstein, and H. Riehl, 1974: On the low-level wind structure in the atlantic trade. *Quarterly Journal of the Royal Meteorological Society*, **100** (423), 109–121.
- Bucci, L., C. O’Handley, G. Emmitt, J. Zhang, K. Ryan, and R. Atlas, 2018: Validation of an airborne doppler wind lidar in tropical cyclones. *Sensors*, **18** (12), doi:[10.3390/s18124288](https://doi.org/10.3390/s18124288), URL <https://www.mdpi.com/1424-8220/18/12/4288>.
- Carr, M., and C. Bretherton, 2001: Convective momentum transport over the tropical pacific: Budget estimates. *Journal of the Atmospheric Sciences*, **58** (13), 1673 – 1693, doi:[10.1175/1520-0469\(2001\)058<1673:CMTOTT>2.0.CO;2](https://doi.org/10.1175/1520-0469(2001)058<1673:CMTOTT>2.0.CO;2), URL <https://journals.ametsoc.org/view/journals/atsc/>

- 58/13/1520-0469_2001_058_1673_cmtott_2.0.co_2.xml.
- Chouza, F., O. Reitebuch, M. Jahn, S. Rahm, and B. Weinzierl, 2016: Vertical wind retrieved by airborne lidar and analysis of island induced gravity waves in combination with numerical models and in situ particle measurements. *Atmospheric Chemistry and Physics*, **16** (7), 4675–4692, doi:10.5194/acp-16-4675-2016, URL <https://acp.copernicus.org/articles/16/4675/2016/>.
- Dias Neto, J., L. Nuijens, C. Unal, and S. Knoop, 2022: Combined wind lidar and cloud radar for wind profiling. *Earth System Science Data Discussions*, 1–30.
- Dixit, V., L. Nuijens, and K. Helfer, 2021: Counter-gradient momentum transport through subtropical shallow convection in icon-lem simulations. *Journal of Advances in Modeling Earth Systems*, e2020MS002352, doi:<https://doi.org/10.1029/2020MS002352>, URL <https://agupubs.onlinelibrary.wiley.com/doi/abs/10.1029/2020MS002352>, e2020MS002352 2020MS002352, <https://agupubs.onlinelibrary.wiley.com/doi/pdf/10.1029/2020MS002352>.
- Dyer, A. J., and B. B. Hicks, 1970: Flux-gradient relationships in the constant flux layer. *Quarterly Journal of the Royal Meteorological Society*, **96** (410), 715–721, doi:<https://doi.org/10.1002/qj.49709641012>, URL <https://rmets.onlinelibrary.wiley.com/doi/abs/10.1002/qj.49709641012>, <https://rmets.onlinelibrary.wiley.com/doi/pdf/10.1002/qj.49709641012>.
- Eberhard, W., R. Cupp, and K. Healy, 1989: Doppler lidar measurement of profiles of turbulence and momentum flux. *Journal of Atmospheric and Oceanic Technology*, **6** (5), 809 – 819, doi:10.1175/1520-0426(1989)006<0809:DLMOP>2.0.CO;2, URL https://journals.ametsoc.org/view/journals/atot/6/5/1520-0426_1989_006_0809_dlmopo_2_0_co_2.xml.
- ECMWF, 2015: *IFS documentation cy41r1*. ECMWF, 4th ed., doi:10.21957/p50qmwprw, operational implementation 12 May 2015.
- Fodor, K., J. Mellado, and M. Wilczek, 2019: On the role of large-scale updrafts and downdrafts in deviations from monin–obukhov similarity theory in free convection. *Boundary-layer meteorology*, **172** (3), 371–396.
- Foken, T., 2006: 50 years of the monin–obukhov similarity theory. *Boundary-Layer Meteorology*, **119** (3), 431–447.
- Fournier, M. B., and J. O. Haerter, 2019: Tracking the gust fronts of convective cold pools. *Journal of Geophysical Research: Atmospheres*, **124** (21), 11 103–11 117, doi:<https://doi.org/10.1029/2019JD030980>, URL <https://agupubs.onlinelibrary.wiley.com/doi/abs/10.1029/2019JD030980>, <https://agupubs.onlinelibrary.wiley.com/doi/pdf/10.1029/2019JD030980>.
- Garratt, J., 1992: *The atmospheric boundary layer*. Cambridge University Press.
- George, G., G. Halloran, S. Kumar, S. Indira Rani, M. Bushair, B. Jangid, J. George, and A. Maycock, 2021: Impact of aeolus horizontal line of sight wind observations in a global nwp system. *Atmospheric Research*, **261**, 105 742, doi:<https://doi.org/10.1016/j.atmosres.2021.105742>, URL <https://www.sciencedirect.com/science/article/pii/S0169809521002982>.
- Gisinger, S., J. Wagner, and B. Witschas, 2020: Airborne measurements and large-eddy simulations of small-scale gravity waves at the tropopause inversion layer over scandinavia. *Atmospheric Chemistry and Physics*, **20** (16), 10 091–10 109, doi:10.5194/acp-20-10091-2020, URL <https://acp.copernicus.org/articles/20/10091/2020/>.
- He, Y., A. Monahan, and N. McFarlane, 2013: Diurnal variations of land surface wind speed probability distributions under clear-sky and low-cloud conditions. *Geophysical Research Letters*, **40** (12), 3308–3314, doi:10.1002/grl.50575.
- Helfer, K. C., and L. Nuijens, 2021: The morphology of simulated trade-wind convection and cold pools under wind shear. *Journal of Geophysical Research: Atmospheres*, **126** (20), e2021JD035 148, doi:<https://doi.org/10.1029/2021JD035148>, URL <https://agupubs.onlinelibrary.wiley.com/doi/abs/10.1029/2021JD035148>, e2021JD035148 2021JD035148, <https://agupubs.onlinelibrary.wiley.com/doi/pdf/10.1029/2021JD035148>.
- Helfer, K. C., L. Nuijens, S. R. de Roode, and A. P. Siebesma, 2020: How wind shear affects trade-wind cumulus convection. *Journal of Advances in Modeling Earth Systems*, **12** (12), e2020MS002 183, doi:<https://doi.org/10.1029/2020MS002183>, URL <https://agupubs.onlinelibrary.wiley.com/doi/abs/10.1029/2020MS002183>, e2020MS002183 10.1029/2020MS002183, <https://agupubs.onlinelibrary.wiley.com/doi/pdf/10.1029/2020MS002183>.

- Helfer, K. C., L. Nuijens, and V. Dixit, 2021: The role of shallow convection in the momentum budget of the trades from large-eddy-simulation hindcasts. *Quarterly Journal of the Royal Meteorological Society*, **147** (737), 2490–2505, doi:<https://doi.org/10.1002/qj.4035>, URL <https://rmets.onlinelibrary.wiley.com/doi/abs/10.1002/qj.4035>, <https://rmets.onlinelibrary.wiley.com/doi/pdf/10.1002/qj.4035>.
- Heus, T., C. F. J. Pols, H. J. J. Jonker, H. E. A. Van den Akker, and D. H. Lenschow, 2009: Observational validation of the compensating mass flux through the shell around cumulus clouds. *Quarterly Journal of the Royal Meteorological Society*, **135** (638), 101–112, doi:<https://doi-org.tudelft.idm.oclc.org/10.1002/qj.358>, URL <https://rmets-onlinelibrary-wiley-com.tudelft.idm.oclc.org/doi/abs/10.1002/qj.358>, <https://rmets-onlinelibrary-wiley-com.tudelft.idm.oclc.org/doi/pdf/10.1002/qj.358>.
- Heus, T., and H. Jonker, 2008: Subsiding shells around shallow cumulus clouds. *Journal of the Atmospheric Sciences*, **65** (3), 1003 – 1018, doi:10.1175/2007JAS2322.1, URL <https://journals.ametsoc.org/view/journals/atsc/65/3/2007jas2322.1.xml>.
- Heus, T., and Coauthors, 2010: Formulation of the dutch atmospheric large-eddy simulation (dales) and overview of its applications. *Geoscientific Model Development*, **3** (2), 415–444.
- Holland, J., and E. Rasmusson, 1973: Measurements of the atmospheric mass, energy, and momentum budgets over a 500-kilometer square of tropical ocean. *Monthly Weather Review*, **101** (1), 44 – 55, doi:10.1175/1520-0493(1973)101<0044:MOTAME>2.3.CO;2, URL https://journals.ametsoc.org/view/journals/mwre/101/1/1520-0493_1973_101_0044_motame_2_3_co_2.xml.
- Holloway, C., A. Wing, S. Bony, C. Muller, H. Masunaga, T. L'Ecuyer, D. Turner, and P. Zuidema, 2017: Observing convective aggregation. *Surveys in Geophysics*, **38** (6), 1199–1236.
- Holtzlag, A., and B. Boville, 1993: Local versus nonlocal boundary-layer diffusion in a global climate model. *Journal of climate*, **6** (10), 1825–1842.
- Horanyi, A., C. Cardinali, M. Rennie, and L. Isaksen, 2015: The assimilation of horizontal line-of-sight wind information into the ecmwf data assimilation and forecasting system. part i: The assessment of wind impact. *Quarterly Journal of the Royal Meteorological Society*, **141** (689), 1223–1232, doi:<https://doi.org/10.1002/qj.2430>, URL <https://rmets.onlinelibrary.wiley.com/doi/abs/10.1002/qj.2430>, <https://rmets.onlinelibrary.wiley.com/doi/pdf/10.1002/qj.2430>.
- Ishwardat, N., O. Krasnov, and A. Yarovoy, 2017: Radar based horizontal wind profile retrieval techniques: Dft applied to scanning doppler radar measurements. M.S. thesis, Electrical Engineering, TU Delft, URL <https://repository.tudelft.nl/islandora/object/uuid:a659654b-e76a-4513-a656-ecad761bdbc8?collection=education>.
- Jungo, G. V., and F. Portè-Agel, 2013: Measurement procedures for characterization of wind turbine wakes with scanning doppler wind lidars. *Adv. Sci. Res.*, 71–75, doi:10.5194/asr-10-71-2013, URL <https://doi.org/10.5194/asr-10-71-2013>.
- Jabouille, P., J. L. Redelsperger, and J. P. Lafore, 1996: Modification of Surface Fluxes by Atmospheric Convection in the TOGA COARE Region. *Monthly Weather Review*, **124** (5), 816–837, doi:10.1175/1520-0493(1996)124<0816:MOSFBA>2.0.CO;2, URL [https://doi.org/10.1175/1520-0493\(1996\)124<0816:MOSFBA>2.0.CO;2](https://doi.org/10.1175/1520-0493(1996)124<0816:MOSFBA>2.0.CO;2), [https://journals.ametsoc.org/mwr/article-pdf/124/5/816/4173699/1520-0493\(1996\)124_0816_mosfba_2_0_co_2.pdf](https://journals.ametsoc.org/mwr/article-pdf/124/5/816/4173699/1520-0493(1996)124_0816_mosfba_2_0_co_2.pdf).
- Kaimal, J. C., J. Wyngaard, Y. Izumi, and O. Cote, 1972: Spectral characteristics of surface-layer turbulence. *Quarterly Journal of the Royal Meteorological Society*, **98** (417), 563–589.
- Kasler, Y., S. Rahm, R. Simmet, and M. Kuhn, 2010: Wake measurements of a multi-mw wind turbine with coherent long-range pulsed doppler wind lidar. *Journal of Atmospheric and Oceanic Technology*, **27** (9), 1529 – 1532, doi:10.1175/2010JTECHA1483.1, URL https://journals.ametsoc.org/view/journals/atot/27/9/2010jtecha1483_1.xml.
- Kirsch, B., F. Ament, and C. Hohenegger, 2021: Convective cold pools in long-term boundary layer mast observations. *Monthly Weather Review*, **149** (3), 811 – 820, doi:10.1175/MWR-D-20-0197.1, URL <https://journals.ametsoc.org/view/journals/mwre/149/3/MWR-D-20-0197.1.xml>.
- Klingebiel, M., and Coauthors, 2019: Remote sensing of sea salt aerosol below trade wind clouds. *Journal of the Atmospheric Sciences*, **76** (5), 1189–1202.
- Koning, A. M., L. Nuijens, F. C. Bosveld, A. P. Siebesma, P. A. van Dorp, and H. J. J. Jonker, 2021: Surface-layer wind shear and momentum transport from clear-sky to cloudy weather

- regimes over land. *Journal of Geophysical Research: Atmospheres*, **126** (21), e2021JD035087, doi:<https://doi.org/10.1029/2021JD035087>, URL <https://agupubs.onlinelibrary.wiley.com/doi/abs/10.1029/2021JD035087>, e2021JD035087 2021JD035087, <https://agupubs.onlinelibrary.wiley.com/doi/pdf/10.1029/2021JD035087>.
- Krishnamurthy, R., A. Choukulkar, R. Calhoun, J. Fine, A. Oliver, and K. Barr, 2013: Coherent doppler lidar for wind farm characterization. *Wind Energy*, **16** (2), 189–206, doi:<https://doi.org/10.1002/we.539>, URL <https://onlinelibrary.wiley.com/doi/abs/10.1002/we.539>, <https://onlinelibrary.wiley.com/doi/pdf/10.1002/we.539>.
- Kropfli, R., 1986: Single doppler radar measurements of turbulence profiles in the convective boundary layer. *Journal of Atmospheric and Oceanic Technology*, **3** (2), 305 – 314, doi:10.1175/1520-0426(1986)003<0305:SDRMOT>2.0.CO;2, URL https://journals.ametsoc.org/view/journals/atot/3/2/1520-0426_1986_003_0305_sdrmot_2_0_co_2.xml.
- Kurowski, M., K. Suselj, W. Grabowski, and J. Teixeira, 2018: Shallow-to-deep transition of continental moist convection: Cold pools, surface fluxes, and mesoscale organization. *Journal of the Atmospheric Sciences*, **75** (12), 4071 – 4090, doi:10.1175/JAS-D-18-0031.1, URL <https://journals.ametsoc.org/view/journals/atoc/75/12/jas-d-18-0031.1.xml>.
- Lamer, K., P. Kollias, and L. Nuijens, 2015: Observations of the variability of shallow trade wind cumulus cloudiness and mass flux. *Journal of Geophysical Research: Atmospheres*, **120** (12), 6161–6178, doi:<https://doi.org/10.1002/2014JD022950>, URL <https://agupubs.onlinelibrary.wiley.com/doi/abs/10.1002/2014JD022950>, <https://agupubs.onlinelibrary.wiley.com/doi/pdf/10.1002/2014JD022950>.
- Lareau, N., Y. Zhang, and S. Klein, 2018: Observed boundary layer controls on shallow cumulus at the arm southern great plains site. *Journal of the Atmospheric Sciences*, **75** (7), 2235–2255.
- LeMone, M., 1983: Momentum transport by a line of cumulonimbus. *Journal of Atmospheric Sciences*, **40** (7), 1815–1834.
- LeMone, M., and D. Jorgensen, 1991: Precipitation and kinematic structure of an oceanic mesoscale convective system. part i: Momentum transport and generation. *Monthly weather review*, **119** (11), 2638–2653.
- LeMone, M., and W. Pennell, 1976: The Relationship of Trade Wind Cumulus Distribution to Subcloud Layer Fluxes and Structure. *Monthly Weather Review*, **104** (5), 524–539, doi:10.1175/1520-0493(1976)104<0524:TROTWC>2.0.CO;2, URL [http://dx.doi.org/10.1175/1520-0493\(1976\)104\(5\)3C0524:TROTWC\(3\)E2.0.CO\(5\)5Cn2](http://dx.doi.org/10.1175/1520-0493(1976)104(5)3C0524:TROTWC(3)E2.0.CO(5)5Cn2).
- Lenschow, D., and P. Stephens, 1980: The role of thermals in the convective boundary layer. *Boundary-Layer Meteorology*, **19**, 509–532, doi:10.1007/BF00122351, URL <https://doi.org/10.1007/BF00122351>.
- Lenschow, D. H., J. Mann, and L. Kristensen, 1994: How long is long enough when measuring fluxes and other turbulence statistics? *Journal of Atmospheric and Oceanic Technology*, **11** (3), 661 – 673, doi:10.1175/1520-0426(1994)011<0661:HLILEW>2.0.CO;2, URL https://journals.ametsoc.org/view/journals/atot/11/3/1520-0426_1994_011_0661_hlilew_2_0_co_2.xml.
- Li, D., and E. Bou-Zeid, 2011: Coherent structures and the dissimilarity of turbulent transport of momentum and scalars in the unstable atmospheric surface layer. *Boundary-layer meteorology*, **140** (2), 243–262.
- Li, Y., D. Thompson, and S. Bony, 2015: The influence of atmospheric cloud radiative effects on the large-scale atmospheric circulation. *Journal of Climate*, **28** (18), 7263–7278.
- Li, Z., P. Zuidema, and P. Zhu, 2014: Simulated convective invigoration processes at trade wind cumulus cold pool boundaries. *Journal of the Atmospheric Sciences*, **71** (8), 2823 – 2841, doi:10.1175/JAS-D-13-0184.1, URL <https://journals.ametsoc.org/view/journals/atoc/71/8/jas-d-13-0184.1.xml>.
- Liu, S., X. Zeng, Y. Dai, and Y. Shao, 2019a: Further improvement of surface flux estimation in the unstable surface layer based on large-eddy simulation data. *Journal of Geophysical Research: Atmospheres*, **124** (17-18), 9839–9854, doi:10.1029/2018JD030222, URL <https://agupubs.onlinelibrary.wiley.com/doi/abs/10.1029/2018JD030222>.
- Liu, Y., and Coauthors, 2011: Simultaneous nested modeling from the synoptic scale to the les scale for wind energy applications. *Journal of Wind Engineering and Industrial Aerodynamics*, **99** (4), 308–319, doi:<https://doi.org/10.1016/j.jweia.2011.01.013>, URL <https://www.sciencedirect.com/science/>

- article/pii/S0167610511000158, the Fifth International Symposium on Computational Wind Engineering.
- Liu, Z., J. Barlow, P. Chan, J. C. H. Fung, Y. Li, C. Ren, H. W. L. Mak, and E. Ng, 2019b: A review of progress and applications of pulsed doppler wind lidars. *Remote Sensing*, **11**, 2522, doi:10.3390/rs11212522, URL <https://www.mdpi.com/2072-4292/11/21/2522/htm#B30-remotesensing-11-02522>.
- Lonitz, K., B. Stevens, L. Nuijens, V. Sant, L. Hirsch, and A. Seifert, 2015: The signature of aerosols and meteorology in long-term cloud radar observations of trade wind cumuli. *Journal of the Atmospheric Sciences*, **72** (12), 4643 – 4659, doi:10.1175/JAS-D-14-0348.1, URL <https://journals.ametsoc.org/view/journals/atsc/72/12/jas-d-14-0348.1.xml>.
- Lux, O., C. Lemmerz, F. Weiler, U. Marksteiner, B. Witschas, S. Rahm, A. Geiß, and O. Reitebuch, 2020: Intercomparison of wind observations from the european space agency's aeolus satellite mission and the aladin airborne demonstrator. *Atmospheric Measurement Techniques*, **13** (4), 2075–2097, doi:10.5194/amt-13-2075-2020, URL <https://amt.copernicus.org/articles/13/2075/2020/>.
- Lux, O., and Coauthors, 2022: Retrieval improvements for the aladin airborne demonstrator in support of the aeolus wind product validation. *Atmospheric Measurement Techniques*, **15** (5), 1303–1331, doi:10.5194/amt-15-1303-2022, URL <https://amt.copernicus.org/articles/15/1303/2022/>.
- Malkus, J., 1949: Effects of wind shear on some aspects of convection. *Eos, Transactions American Geophysical Union*, **30** (1), 19–25.
- Mallaun, C., A. Giez, and R. Baumann, 2015: Calibration of 3-d wind measurements on a single-engine research aircraft. *Atmospheric Measurement Techniques*, **8** (8), 3177–3196, doi:10.5194/amt-8-3177-2015, URL <https://amt.copernicus.org/articles/8/3177/2015/>.
- Mallaun, C., A. Giez, G. J. Mayr, and M. W. Rotach, 2019: Subsiding shells and the distribution of up- and downdraughts in warm cumulus clouds over land. *Atmospheric Chemistry and Physics*, **19** (15), 9769–9786, doi:10.5194/acp-19-9769-2019, URL <https://acp.copernicus.org/articles/19/9769/2019/>.
- Mann, J., A. Peña, F. Bingol, R. Wagner, and M. S. Courtney, 2010: Lidar scanning of momentum flux in and above the atmospheric surface layer. *Journal of Atmospheric and Oceanic Technology*, **27** (6), 959 – 976, doi:10.1175/2010JTECHA1389.1, URL https://journals.ametsoc.org/view/journals/atot/27/6/2010jtecha1389_1.xml.
- Marchaj, C., 1996: *Sail Performance: Theory and Practice*. Adlard Coles Nautical, URL https://books.google.nl/books?id=1_F4HAAACAAJ.
- Maulik, R., V. Rao, S. Renganathan, S. Letizia, and G. Iungo, 2021: Cluster analysis of wind turbine wakes measured through a scanning doppler wind lidar. *AIAA Scitech 2021 Forum*, 1181.
- Mazzaro, L. J., D. Muñoz-Esparza, J. K. Lundquist, and R. R. Linn, 2017: Nested mesoscale-toles modeling of the atmospheric boundary layer in the presence of under-resolved convective structures. *Journal of Advances in Modeling Earth Systems*, **9** (4), 1795–1810, doi:<https://doi.org/tudelft.idm.oclc.org/10.1002/2017MS000912>, URL <https://agupubs-onlinelibrary-wiley-com.tudelft.idm.oclc.org/doi/abs/10.1002/2017MS000912>, <https://agupubs-onlinelibrary-wiley-com.tudelft.idm.oclc.org/doi/pdf/10.1002/2017MS000912>.
- McMichael, L., and Coauthors, 2020: Characterizing subsiding shells in shallow cumulus using doppler lidar and large-eddy simulation. *Geophysical Research Letters*, **47** (18), e2020GL089699, doi:<https://doi.org/10.1029/2020GL089699>, URL <https://agupubs.onlinelibrary.wiley.com/doi/abs/10.1029/2020GL089699>, e2020GL089699 2020GL089699, <https://agupubs.onlinelibrary.wiley.com/doi/pdf/10.1029/2020GL089699>.
- Melville, W. K., 1996: The role of surface-wave breaking in air-sea interaction. *Annual review of fluid mechanics*, **28** (1), 279–321.
- Moene, A., and J. van Dam, 2014: *Transport in the Atmosphere-Vegetation-Soil continuum*. Cambridge University Press.
- Moeng, C.-H., and P. Sullivan, 1994: A comparison of shear-and buoyancy-driven planetary boundary layer flows. *Journal of Atmospheric Sciences*, **51** (7), 999–1022.
- Moncrieff, M., 1997: Momentum transport by organized convection. *The Physics and Parameterization of Moist Atmospheric Convection*, Springer, 231–253.
- Neggers, R., 2015: Attributing the behavior of low-level clouds in large-scale models to subgrid-scale parameterizations. *J. Adv. Model. Earth Syst.*, **7**, 2029–2043.

- Neggens, R., H. Jonker, and A. Siebesma, 2003: Size statistics of cumulus cloud populations in large-eddy simulations. *Journal of the atmospheric sciences*, **60** (8), 1060–1074.
- Nicholls, S., and M. LeMone, 1980: The fair weather boundary layer in gate: The relationship of subcloud fluxes and structure to the distribution and enhancement of cumulus clouds. *Journal of Atmospheric Sciences*, **37** (9), 2051 – 2067, doi:10.1175/1520-0469(1980)037<2051:TFWBLL>2.0.CO;2, URL https://journals.ametsoc.org/view/journals/atsc/37/9/1520-0469_1980_037_2051_tfwbli_2_0_co_2.xml.
- Nicholls, S., and C. Readings, 1981: Spectral characteristics of surface layer turbulence over the tropical ocean. *Quarterly Journal of Meteorological Society*, 591–614, doi:10.1175/1520-0485(1975)005<0157:scosl>2.0.co;2.
- Nuijens, L., A. Savazzi, B. de Boer, G., P.-E., M. Lothon, G. George, and D. Zhang, 2022: The frictional layer in the observed momentum budget of the trades. Tech. rep., Copernicus Meetings. doi:<https://doi.org/10.5194/egusphere-egu22-8080>.
- Nuijens, L., B. Stevens, and A. Siebesma, 2009: The environment of precipitating shallow cumulus convection. *Journal of the Atmospheric Sciences*, **66** (7), 1962–1979, doi:<https://doi.org/10.1175/2008JAS2841.1>, URL <https://journals.ametsoc.org/view/journals/atsc/66/7/2008jas2841.1.xml>.
- Pennell, W. T., and M. A. LeMone, 1974: An experimental study of turbulence structure in the fair-weather trade wind boundary layer. *Journal of Atmospheric Sciences*, **31** (5), 1308 – 1323, doi:10.1175/1520-0469(1974)031<1308:AESOTS>2.0.CO;2, URL https://journals.ametsoc.org/view/journals/atsc/31/5/1520-0469_1974_031_1308_aesots_2_0_co_2.xml.
- Pichugina, Y., and Coauthors, 2017: Properties of the offshore low level jet and rotor layer wind shear as measured by scanning doppler lidar. *Wind Energy*, **20** (6), 987–1002.
- Pu, Z., L. Zhang, S. Zhang, B. Gentry, D. Emmitt, B. Demott, and R. Atlas, 2017: *The Impact of Doppler Wind Lidar Measurements on High-Impact Weather Forecasting: Regional OSSE and Data Assimilation Studies*, 259–283. Springer International Publishing, Cham, doi:10.1007/978-3-319-43415-5_12, URL https://doi.org/10.1007/978-3-319-43415-5_12.
- Romps, D., 2017: Exact expression for the lifting condensation level. *Journal of the Atmospheric Sciences*, **74** (12), 3891–3900.
- Rotunno, R., J. Klemp, and M. Weisman, 1988: A theory for strong, long-lived squall lines. *Journal of Atmospheric Sciences*, **45** (3), 463–485.
- Saggiorato, B., L. Nuijens, A. P. Siebesma, S. de Roode, I. Sandu, and L. Papritz, 2020: The influence of convective momentum transport and vertical wind shear on the evolution of a cold air outbreak. *Journal of Advances in Modeling Earth Systems*, **12** (6), e2019MS001991, doi:<https://doi.org/10.1029/2019MS001991>, URL <https://agupubs.onlinelibrary.wiley.com/doi/abs/10.1029/2019MS001991>, e2019MS001991 10.1029/2019MS001991, <https://agupubs.onlinelibrary.wiley.com/doi/pdf/10.1029/2019MS001991>.
- Sakradzija, M., and D. Klocke, 2018: Physically constrained stochastic shallow convection in realistic kilometer-scale simulations. *Journal of Advances in Modeling Earth Systems*, **10** (11), 2755–2776, doi:<https://doi-org.tudelft.idm.oclc.org/10.1029/2018MS001358>, URL <https://agupubs-onlinelibrary-wiley-com.tudelft.idm.oclc.org/doi/abs/10.1029/2018MS001358>, <https://agupubs-onlinelibrary-wiley-com.tudelft.idm.oclc.org/doi/pdf/10.1029/2018MS001358>.
- Schäfler, A., and Coauthors, 2018: The north atlantic waveguide and downstream impact experiment. *Bulletin of the American Meteorological Society*, **99** (8), 1607 – 1637, doi:10.1175/BAMS-D-17-0003.1, URL <https://journals.ametsoc.org/view/journals/bams/99/8/bams-d-17-0003.1.xml>.
- Schalkwijk, J., F. Bosveld, and A. Siebesma, 2010: *Timescales and structures in vertical transport in the atmospheric boundary layer*. Citeseer.
- Schalkwijk, J., H. Jonker, A. Siebesma, and F. Bosveld, 2015: A year-long large-eddy simulation of the weather over cabauw: An overview. *Monthly Weather Review*, **143** (3), 828–844.
- Schemann, V., K. Ebell, B. Pospichal, R. Neggens, C. Moseley, and B. Stevens, 2020: Linking large-eddy simulations to local cloud observations. *Journal of Advances in Modeling Earth Systems*, **12** (12), e2020MS002209, doi:<https://doi.org/10.1029/2020MS002209>, URL <https://agupubs.onlinelibrary.wiley.com/doi/abs/10.1029/2020MS002209>, e2020MS002209 10.1029/2020MS002209.
- Schlemmer, L., P. Bechtold, I. Sandu, and M. Ahlgrim, 2017: Uncertainties related to the repre-

- sensation of momentum transport in shallow convection. *Journal of Advances in Modeling Earth Systems*, **9** (2), 1269–1291, doi:<https://doi.org/10.1002/2017MS000915>, URL <https://agupubs.onlinelibrary.wiley.com/doi/abs/10.1002/2017MS000915>, <https://agupubs.onlinelibrary.wiley.com/doi/pdf/10.1002/2017MS000915>.
- Schneemann, J., F. Theuer, A. Rott, M. Dorenkamper, and M. Kuehn, 2021: Offshore wind farm global blockage measured with scanning lidar. *Wind Energy Science*, **6** (2), 521–538, doi:10.5194/wes-6-521-2021, URL <https://wes.copernicus.org/articles/6/521/2021/>.
- Scholbrock, A., P. Fleming, D. Schlipf, A. Wright, K. Johnson, and N. Wang, 2016: Lidar-enhanced wind turbine control: Past, present, and future. *2016 American Control Conference (ACC)*, IEEE, 1399–1406.
- Shukla, J., and Y. Sud, 1981: Effect of cloud-radiation feedback on the climate of a general circulation model. *Journal of the Atmospheric Sciences*, **38** (11), 2337–2353.
- Siebesma, A., P. Soares, and J. Teixeira, 2007: A combined eddy-diffusivity mass-flux approach for the convective boundary layer. *Journal of the Atmospheric Sciences*, **64** (4), 1230 – 1248, doi:10.1175/JAS3888.1, URL <https://journals.ametsoc.org/view/journals/atsc/64/4/jas3888.1.xml>.
- Siebesma, A., and Coauthors, 2003: A large eddy simulation intercomparison study of shallow cumulus convection. *Journal of the Atmospheric Sciences*, **60** (10), 1201 – 1219, doi:10.1175/1520-0469(2003)60<1201:ALESIS>2.0.CO;2, URL https://journals.ametsoc.org/view/journals/atsc/60/10/1520-0469_2003_60_1201_alesis_2.0.co_2.xml.
- Siebesma, A. P., and J. W. M. Cuijpers, 1995: Evaluation of parametric assumptions for shallow cumulus convection. *Journal of Atmospheric Sciences*, **52** (6), 650 – 666, doi:10.1175/1520-0469(1995)052<0650:EOPAFS>2.0.CO;2, URL https://journals.ametsoc.org/view/journals/atsc/52/6/1520-0469_1995_052_0650_eopafs_2_0_co_2.xml.
- Skofronick-Jackson, G., and Coauthors, 2021: The joint aeolus tropical atlantic campaign - first results for aeolus calibration/validation and science in the tropics. *ATMOS 2021*, ESA, Virtual Meeting, France, URL <https://hal-insu.archives-ouvertes.fr/insu-03466111>.
- Soden, B., and I. Held, 2006: An assessment of climate feedbacks in coupled ocean–atmosphere models. *Journal of Climate*, **19** (14), 3354 – 3360, doi:10.1175/JCLI3799.1, URL <https://journals.ametsoc.org/view/journals/clim/19/14/jcli3799.1.xml>.
- Stevens, B., 2007: On the growth of layers of non-precipitating cumulus convection. *Journal of the atmospheric sciences*, **64** (8), 2916–2931.
- Stevens, B., and Coauthors, 2001: Simulations of trade wind cumuli under a strong inversion. *Journal of the Atmospheric Sciences*, **58** (14), 1870 – 1891, doi:10.1175/1520-0469(2001)058<1870:SOTWCU>2.0.CO;2, URL https://journals.ametsoc.org/view/journals/atsc/58/14/1520-0469_2001_058_1870_sotwcu_2.0.co_2.xml.
- Stevens, B., and Coauthors, 2016: The barbados cloud observatory: Anchoring investigations of clouds and circulation on the edge of the itcz. *Bulletin of the American Meteorological Society*, **97** (5), 787 – 801, doi:10.1175/BAMS-D-14-00247.1, URL <https://journals.ametsoc.org/view/journals/bams/97/5/bams-d-14-00247.1.xml>.
- Stevens, B., and Coauthors, 2019: A high-altitude long-range aircraft configured as a cloud observatory: The narval expeditions. *Bulletin of the American Meteorological Society*, **100** (6), 1061–1077.
- Stevens, B., and Coauthors, 2021: Eurec4a. *Earth System Science Data*, **13** (8), 4067–4119.
- Stevens, D., A. Ackerman, and C. Bretherton, 2002: Effects of domain size and numerical resolution on the simulation of shallow cumulus convection. *Journal of the Atmospheric Sciences*, **59** (23), 3285 – 3301, doi:10.1175/1520-0469(2002)059<3285:EODSAN>2.0.CO;2, URL https://journals.ametsoc.org/view/journals/atsc/59/23/1520-0469_2002_059_3285_eodsan_2.0.co_2.xml.
- Stull, R., 1988: *An Introduction to Boundary Layer Meteorology*. Kluwer Academic Publishers.
- Sullivan, P., J. McWilliams, and C.-H. Moeng, 1994: A subgrid-scale model for large-eddy simulation of planetary boundary-layer flows. *Boundary-Layer Meteorology*, **71** (3), 247–276.
- Thompson, N., K. L. Webber, and B. P. Norris, 1980: Eddy-fluxes and spectra in the gate sub-cloud layer. *Quarterly Journal of the Royal Meteorological Society*, **106** (448), 277–292, doi:<https://doi.org/10.1002/qj.49710644804>, URL <https://rmets-onlinelibrary-wiley-com.tudelft.idm.oclc.org/doi/abs/10.1002/qj.49710644804>, <https://rmets-onlinelibrary-wiley-com.tudelft.idm.oclc.org/doi/pdf/10.1002/qj.49710644804>.

- Tiedtke, M., 1989: A comprehensive mass flux scheme for cumulus parameterization in large-scale models. *Monthly Weather Review*, **117** (8), 1779 – 1800, doi:10.1175/1520-0493(1989)117<1779:ACMFSF>2.0.CO;2, URL https://journals.ametsoc.org/view/journals/mwre/117/8/1520-0493_1989_117_1779_acmfsf_2_0_co_2.xml.
- Troen, I., and L. Mahrt, 1986: A simple model of the atmospheric boundary layer; sensitivity to surface evaporation. *Boundary-Layer Meteorology*, **37** (1-2), 129–148.
- Tung, W.-W., and M. Yanai, 2002: Convective momentum transport observed during the toga coare iop. part ii: Case studies. *Journal of Atmospheric Sciences*, **59** (17), 2535–2549.
- van Stratum, B., J. Vila-Guerau de Arellano, C. van Heerwaarden, and H. Ouwersloot, 2014: Subcloud-layer feedbacks driven by the mass flux of shallow cumulus convection over land. *Journal of the Atmospheric Sciences*, **71** (3), 881–895.
- Vial, J., and Coauthors, 2019: A new look at the daily cycle of trade wind cumuli. *Journal of Advances in Modeling Earth Systems*, **11** (10), 3148–3166, doi:<https://doi.org/tudelft.idm.oclc.org/10.1029/2019MS001746>, URL <https://agupubs-onlinelibrary-wiley-com.tudelft.idm.oclc.org/doi/abs/10.1029/2019MS001746>, <https://agupubs-onlinelibrary-wiley-com.tudelft.idm.oclc.org/doi/pdf/10.1029/2019MS001746>.
- Voigt, A., N. Albern, P. Ceppi, K. Grise, Y. Li, and B. Medeiros, 2021: Clouds, radiation, and atmospheric circulation in the present-day climate and under climate change. *Wiley Interdisciplinary Reviews: Climate Change*, **12** (2), e694.
- Wagner, J., and Coauthors, 2017: Observed versus simulated mountain waves over scandinavia – improvement of vertical winds, energy and momentum fluxes by enhanced model resolution? *Atmospheric Chemistry and Physics*, **17** (6), 4031–4052, doi:10.5194/acp-17-4031-2017, URL <https://acp.copernicus.org/articles/17/4031/2017/>.
- Webb, M., and Coauthors, 2006: On the contribution of local feedback mechanisms to the range of climate sensitivity in two gcm ensembles. *Climate Dynamics*, **27**, 17–38, URL <https://doi.org/10.1007/s00382-006-0111-2>.
- Weissmann, M., R. Busen, A. Dörnbrack, S. Rahm, and O. Reitebuch, 2005: Targeted observations with an airborne wind lidar. *Journal of Atmospheric and Oceanic Technology*, **22** (11), 1706 – 1719, doi:10.1175/JTECH1801.1, URL https://journals.ametsoc.org/view/journals/atot/22/11/jtech1801_1.xml.
- Witschas, B., C. Lemmerz, A. Geiß, O. Lux, U. Marksteiner, S. Rahm, O. Reitebuch, and F. Weiler, 2020: First validation of aeolus wind observations by airborne doppler wind lidar measurements. *Atmospheric Measurement Techniques*, **13** (5), 2381–2396, doi:10.5194/amt-13-2381-2020, URL <https://amt.copernicus.org/articles/13/2381/2020/>.
- Witschas, B., S. Rahm, A. Dörnbrack, J. Wagner, and M. Rapp, 2017: Airborne wind lidar measurements of vertical and horizontal winds for the investigation of orographically induced gravity waves. *Journal of Atmospheric and Oceanic Technology*, **34** (6), 1371–1386, doi:<https://doi.org/10.1175/JTECH-D-17-0021.1>, URL <https://journals.ametsoc.org/view/journals/atot/34/6/jtech-d-17-0021.1.xml>.
- Wu, X., and M. Yanai, 1994: Effects of Vertical Wind Shear on the Cumulus Transport of Momentum: Observations and Parameterization. *Journal of the Atmospheric Sciences*, **51** (12), 1640–1660, doi:10.1175/1520-0469(1994)051<1640:EOVWSO>2.0.CO;2, URL [https://doi.org/10.1175/1520-0469\(1994\)051<1640:EOVWSO>2.0.CO;2](https://doi.org/10.1175/1520-0469(1994)051<1640:EOVWSO>2.0.CO;2), [https://journals.ametsoc.org/jas/article-pdf/51/12/1640/3426877/1520-0469\(1994\)051_1640_eovwso_2_0_co_2.pdf](https://journals.ametsoc.org/jas/article-pdf/51/12/1640/3426877/1520-0469(1994)051_1640_eovwso_2_0_co_2.pdf).
- Wutzler, T., A. Lucas-Moffat, M. Migliavacca, J. Knauer, K. Sickel, L. Šigut, O. Menzer, and M. Reichstein, 2018: Basic and extensible post-processing of eddy covariance flux data with reddyproc. *Biogeosciences*, **15** (16), 5015–5030.
- Yamaguchi, T., G. Feingold, and J. Kazil, 2019: Aerosol-cloud interactions in trade wind cumulus clouds and the role of vertical wind shear. *Journal of Geophysical Research: Atmospheres*, **124** (22), 12 244–12 261.
- Yuan, J., H. Xia, T. Wei, L. Wang, B. Yue, and Y. Wu, 2020: Identifying cloud, precipitation, windshear, and turbulence by deep analysis of the power spectrum of coherent doppler wind lidar. *Optics Express*, **28** (25), 37 406–37 418.
- Zhan, L., S. Letizia, and G. Valerio Iungo, 2020: Lidar measurements for an onshore wind farm: Wake vari-

- ability for different incoming wind speeds and atmospheric stability regimes. *Wind Energy*, **23** (3), 501–527, doi:<https://doi.org/10.1002/we.2430>, URL <https://onlinelibrary.wiley.com/doi/abs/10.1002/we.2430>, <https://onlinelibrary.wiley.com/doi/pdf/10.1002/we.2430>.
- Zhang, Y., and S. A. Klein, 2013: Factors controlling the vertical extent of fair-weather shallow cumulus clouds over land: Investigation of diurnal-cycle observations collected at the arm southern great plains site. *Journal of the Atmospheric Sciences*, **70** (4), 1297 – 1315, doi:10.1175/JAS-D-12-0131.1, URL <https://journals.ametsoc.org/view/journals/atsc/70/4/jas-d-12-0131.1.xml>.
- Zhu, P., 2015: On the mass-flux representation of vertical transport in moist convection. *Journal of the Atmospheric Sciences*, **72** (12), 4445 – 4468, doi:10.1175/JAS-D-14-0332.1, URL <https://journals.ametsoc.org/view/journals/atsc/72/12/jas-d-14-0332.1.xml>.
- Zuidema, P., G. Torri, C. Muller, and A. Chandra, 2017: A survey of precipitation-induced atmospheric cold pools over oceans and their interactions with the larger-scale environment. *Surveys in Geophysics*, **38** (6), 1283–1305.
- Zuidema, P., and Coauthors, 2012: On trade wind cumulus cold pools. *Journal of the Atmospheric Sciences*, **69** (1), 258 – 280, doi:10.1175/JAS-D-11-0143.1, URL <https://journals.ametsoc.org/view/journals/atsc/69/1/jas-d-11-0143.1.xml>.

Acknowledgements

"The pessimist complains about the wind;
The optimist expects it to change;
The realist adjusts the sails."

William Arthur Ward

We all are a pessimist, optimist, or realist at some point. During my PhD, I switched mindset multiple times, but with the broad support and help of colleagues, friends, and family, I have been able to adjust the sails to reach the final port. Here I'll take the opportunity to express my thanks.

First Louise: Thank you for your support, and keeping me on track when I wonder off in something else that is also interesting, for taking me out on the research flight which was both very cool and afterwards insightful in understanding the conditions in which the data was taken. I am grateful for the opportunity to develop myself in many aspects, both in setting up research, but also in presenting, writing and discussing, and being member of the PhD Council. Many thanks to Pier and Fred, your enthusiasm and expertise in the modeling and observational world of meteorology helped very much in completing the first paper and throughout the rest of my PhD. Also thanks to the Whiffle crew, especially Harm and Pim, for the discussions and for running the best model set-up as possible, ever including new features and improvements. I also want to thank the DLR crew for your hospitality and especially to Christian Mallaun, Christian Lemmerz, Benjamin Witschas, and Oliver Reitebuch for your help with the second article.

Then the *cloud dummies*: first and foremost to Bea and Kevin, with whom I shared an office, went on conferences with (lost some posters on the way – how many PhDs does it take to get a poster to a conference?!) and even spent some holidays together. Also thanks to Vishal and Alessandro for the nice discussions and the fun dinners we had together with Louise, as well as to Jose for teaching me some basics of cloud radar and wind lidar, the great discussions we had lately, and for sharing so many nice (trumpet) music and playing together. Furthermore, thanks to Steven. Although you were officially a "stable boundary layer guy", you almost seemed part of our group, and were always there to help out and connected both groups. Many other colleagues made life at GRS enjoyable and fun, I hereby thank you all! A PhD cannot be finished without the help of Niels for any computer matters nor without the support of Debbie, Suzanne, Lidwien, and Natascha who are always there to help out or for a chat!

I am very grateful to Bas and Marie-Claire that I had the opportunity to spend

my last half year at the TU in the Fruit-frost group. In this short period, I was not only encouraged to finish my PhD, but I learned very many things, not only about plants and the greenhouse business, but also the ins and outs of organizing fieldwork, from our discussions, and from cooperating in a large group with a broad range of specialists. Dai and Judith, many thanks for your help in familiarizing me with the available instruments, fieldwork practicalities, and especially your expertise in DTS. I am sure that made the fieldwork as big a success.

I also extend my gratitude to KNMI and, in particular Philippe, for providing me with the opportunity to successfully finish the last parts of my PhD while working at the institute. Feeling supported, also from my direct colleagues, helped me a lot.

Of course, I cannot forget my friends outside the department: Thierry, Karlijn, Ivy, Chak, and Else, for the relaxing moments and all the board games that we played. Let's keep that up. Ruben and Selma, for sharing the love for science and for a tasty craft beer. Eva, Kathelijne, Leonoor, and Auke: at some point you didn't dare asking about the state of my first paper, but now the whole thesis is finished, thanks for your support! Dominique and Matthijs, thank you for inspiring me in many ways and for the great hiking and biking trips that we did together. I really enjoy those! Manon, we don't see each other often, but I know you're only a phone call away. Frans and Marloes, thank you for being there. No matter what, I know I can count on your help and advice.

Last, but not least my family, especially those that are closest to me: mum and dad, Maria, Erik, Wilma, Robert and Manouk, Sabine, Sjoerd, Opa and Oma, Marjolein and Harmen. We have shared so many great, but also sad moments together. Having such a loving family around me is a great comfort that cannot be described in words. A special thanks to Rogier. You are always the one reading manuals, and it seems like you know mine better than I do. Thank you for always being there, for inspiring and encouraging me to start playing trumpet and give me back my beloved music after I had to give up playing piano, and for kicking me out to go for a run when I cannot stop fretting about anything. I love you.

That's all folks!

About the author

Mariska Koning (Capelle aan den IJssel, 6 June 1993) graduated from the Marnix Gymnasium in 2011, after which she started her academic journey at TU Delft with a Bachelor of Science in Applied Physics. She obtained this degree in 2015, upon finishing her thesis "Cu₂N on Cu₃Au as substrate for the study of magnetic atoms". Applied physics is still quite fundamental, and although she enjoyed that, she decided to pursue a master's degree with something more tangible and enrolled into Geoscience and Remote Sensing.

This multidisciplinary domain opened up a wide array of research fields, ranging from wavefield imaging to planetary science and to land monitoring through various technologies such as satellites, GPS, and traditional measurement techniques. However, it was atmospheric physics, and specifically clouds, that had initially driven her to begin this masters track.

Diving into the interaction of clouds and winds, which also formed the central theme of her master's thesis, Mariska successfully earned the degree of Master of Science (2017). As she progressed into her doctoral studies, she became well-versed in processing measurement data from diverse sources and analyzing the subtle effects that clouds exert on the wind amidst complex atmospheric processes.

She is grateful to have taken part as a postdoctoral researcher in the innovative *Plantenna* project. This experience allowed Mariska to cultivate a whole new set of skills, ranging from selecting new instruments, installing them in the field to organising the measurement campaigns in close consultation with the multidisciplinary team of scientists within *Plantenna*. The project also broadened her knowledge in fields of plants, greenhouse dynamics, hydrology, and various measurement techniques essential for monitoring these intricate systems.

She is pleased to have found her ideal job in the Research & Development, Observations and Data technology department at KNMI (Royal Dutch Meteorological Institute). Together with her colleagues she ensures the quality of research conducted at Cabauw, and plays an integral role in leveraging the Cabauw data for scientific investigations.

List of Publications

- **Koning, A. M.**, Nuijens, L., Bosveld, F. C., Siebesma, A. P., van Dorp, P. A., & Jonker, H. J. J. (2021). Surface-Layer Wind Shear and Momentum Transport From Clear-Sky to Cloudy Weather Regimes Over Land. *Journal of Geophysical Research: Atmospheres*, 126(21), doi:10.1029/2021JD035087
- **Koning, A. M.**, Nuijens, L., Mallaun, C. (2022). Momentum fluxes from airborne wind measurements in three cumulus cases over land. *Atmospheric Chemistry and Physics*, 22(11), doi:10.5194/acp-22-7373-2022

